THESIS FOR THE DEGREE OF DOCTOR OF PHILOSOPHY IN THERMO AND FLUID DYNAMICS

Energy saving strategies for electric vehicles operating in cold climates

ANANDH RAMESH BABU

Department of Mechanics and Maritime Sciences

CHALMERS UNIVERSITY OF TECHNOLOGY

Göteborg, Sweden 2024

Energy saving strategies for electric vehicles operating in cold climates
ANANDH RAMESH BABU
ISBN 978-91-8103-037-2

Doktorsavhandlingar vid Chalmers tekniska högskola
Ny serie nr. 5495
ISSN 0346-718X
Department of Mechanics and Maritime Sciences
Chalmers University of Technology
SE-412 96 Göteborg
Sweden
Telephone: +46 (0)31-772 1000

Chalmers Digitaltryck
Göteborg, Sweden 2024

Energy saving strategies for electric vehicles operating in cold climates
ANANDH RAMESH BABU
Department of Mechanics and Maritime Sciences
Chalmers University of Technology

Abstract

Electromobility has gained significance over recent years in an attempt to reduce greenhouse gas emissions contributing to climate change. The requirements for the performance and efficiency of electric vehicles are high to make them an attractive alternative to conventional fossil-fuel-driven vehicles. Lithium-ion batteries are excellent energy storage systems when operated under conducive conditions, i.e. a temperature range of 15°C to 35°C. Their performance and cycling life are drastically affected when operated outside this range. In cold climates, the battery packs need to be heated for optimal performance. Additionally, the passenger cabins must be climatized. The energy for battery and cabin heating is derived from the packs, which consequently results in reduced driving range.

This work is concerned with strategies for reducing these heating loads. Three methods, namely cabin insulation, cabin air recirculation, and battery pack thermal encapsulation, have been investigated to estimate heating load reductions and their influence on vehicle range.

Cabin insulation was investigated on a passenger car cabin and a truck cabin using computational fluid dynamics (CFD). Insulating the cabin reduced the heat losses, heating the cabin faster and to higher mean temperatures than the non-insulated configuration under a constant heating load. An adaptive cabin air recirculation strategy was used to control the return-air ratio such that window fogging was avoided, and good air quality could be maintained. Numerical simulations using a coupled CFD-thermoregulation model were performed on the truck cabin with cabin heating and recirculation controllers. Combining the two strategies (cabin insulation and air recirculation) further decreased the cabin heating energy consumption.

Thermal encapsulation of battery packs as a means of passive battery thermal management was tested to improve the battery performance and decrease the heating demand for climatization after long parking periods in cold climates. Several levels of insulation on a calibrated battery pack model were studied under cool-down scenarios. With sufficient thermal resistance, the heat loss from the pack was minimized and the packs were kept at near-optimal temperatures.

Finally, vehicle simulations were performed for a truck under parking-driving scenarios to investigate the effectiveness of all the strategies combined at various ambient temperatures. The cabin heating load decreased significantly, and the battery heating load was eliminated for all low ambient temperatures. Their combined effects led to the increase in vehicle range at low ambient temperatures, up to 7% at -20°C.

Keywords: electric vehicle, low-temperature BEV performance, cabin climatization, battery pack climatization, CFD, cabin insulation, cabin air recirculation, battery encapsulation

"And I knew exactly what to do. But in a much more real sense, I had no idea what to do."

- Michael Scott

Acknowledgements

First of all, I would like to thank my supervisor and examiner Prof. Simone Sebben for all the constant guidance and support through the years, especially her patience and continuous feedback for improving the quality of my work. Secondly, I would like to thank Adj. Prof. Sassan Etemad, VGTT for his support and cooperation in the later stages of the project. I would also like to thank all my supervisors from Chalmers, VCC, and VGTT namely, Dr. Jelena Andric, Dr. Blago Minovski, Tore Bark, and Dr. Zenitha Chronéer for all their invaluable knowledge and discussions during the project. I want to acknowledge Dr. Masih Khoshab, and Dr. Majid Astaneh for their invaluable input. I want to express my utmost gratitude to all those who made this work possible.

I want to acknowledge the Swedish Energy Agency, VGTT, and VCC for their funding, and Prof. Lennart Löfdahl and Alexander Broniewicz for initiating the research project. The simulations were performed on the computational clusters at Volvo Cars and National Academic Infrastructure for Supercomputing in Sweden (NAISS).

I want to show my deepest appreciation to all my former and present colleagues, and friends at VEAS for creating an excellent work environment. The fun discussions and activities throughout the years have made this journey delightful. I am thankful to everyone in the RVAD group for the open and spontaneous discussions. I will cherish the memories of the after-works, climbing sessions, chats, and exhilarating games of ping pong. I want to thank Sonja, who always has our best interests in mind.

Most importantly, thank you to all my friends and especially my family for supporting, inspiring, and putting up with me all these years.

Anandh Ramesh Babu
Göteborg, May 2024

Nomenclature

Abbreviations

0D	Zero Dimensional
1D	One Dimensional
3D	Three Dimensional
BEV	Battery Electric Vehicle
BMS	Battery Management System
BTMS	Battery Thermal Management System
CFD	Computational Fluid Dynamics
CHT	Conjugate Heat Transfer
ECM	Electrical Circuit Model
HPPC	Hybrid Pulse Power Characterization
HVAC	Heating Ventilation and Air Conditioning
HWFET	HighWay Fuel Economy Test
ICEV	Internal Combustion Engine-powered Vehicle
JOS	JOint System thermoregulation
LIB	Lithium-ion Battery
NMC	Nickel Mangenese Cobalt
PCM	Phase Change Material
PI	Proportional Integral
PTC	Positive Thermal Coefficient
RANS	Reynolds Averaged Navier-Stokes
RAR	Return Air Ratio
RH	Relative Humidity
SoC	State of Charge
URANS	Unsteady Reynolds Averaged Navier-Stokes
VCC	Volvo Car Corporation
VGTT	Volvo Group Truck Technology
VTMS	Vehicle Thermal Management System

Subscripts

0	Initial value of the quantity
∞	Ambient condition
bo	Upstream condition to the heater
cab	Mean quantity in the cabin

in	Inlet condition of a quantity	
k	Step index	
REC	Mass-averaged quantity from the recirculation outlet	
ref	Reference value of the quantity	
set	Setpoint for the corresponding quantity	

Symbols

β	Road gradient	[rad]
μ_r	Tyre rolling resistance	[−]
a_v	Vehicle acceleration	$\left[\frac{\mathrm{m}}{\mathrm{s}^2}\right]$
A_{f_v}	Vehicle frontal area	$\left[\mathrm{m}^2\right]$
C_d	Drag coefficient	[−]
C_i	Polarization capacitance in the ECM	[F]
g	Acceleration due to gravity	$\left[\frac{\mathrm{m}}{\mathrm{s}^2}\right]$
I	Current	[A]
M_v	Vehicle mass	[kg]
P_v	Vehicle traction power	[W]
R_0	Cell internal resistance	[Ω]
U_{oc}	Open-circuit voltage	[V]
V_T	Terminal voltage	[V]
v_v	Vehicle velocity	$\left[\frac{\mathrm{m}}{\mathrm{s}}\right]$
v_{legal}	Legal speed limit	$\left[\frac{\mathrm{m}}{\mathrm{s}}\right]$
v_{target}	Driver target speed	$\left[\frac{\mathrm{m}}{\mathrm{s}}\right]$
Y	Road curvature	$\left[\mathrm{m}^{-1}\right]$
α	CO_2 concentration	[ppm]
Δt	Timestep when all transport equations are solved	[s]
Δt^*	Timestep while solving only the energy equation	[s]
Δx_ω	Difference between the setpoint vapor mass fraction and the ambient vapor mass fraction	[−]
$\dot{m}$	Mass flow rate	$\left[\frac{\mathrm{kg}}{\mathrm{s}}\right]$
$\dot{Q}$	Battery heat generation	[W]
γ	Recirculation or return-air ratio	[−]
λ	Thermal conductivity	$\left[\frac{\mathrm{W}}{\mathrm{m}\cdot\mathrm{K}}\right]$
ω	Specific humidity	[−]
ϕ	Relative humidity	[%]
τ	Thermal time constant	[h]
θ	Non-dimensionalized temperature	[−]

c_p	Specific heat capacity	$\left[\frac{\text{kJ}}{\text{kg}\cdot\text{K}}\right]$
D	Diameter of coolant channel	[m]
dt_{co}	Co-simulation time interval	[s]
e	PI controller error	[−]
h	Heat transfer coefficient	$\left[\frac{\text{W}}{\text{m}^2\text{K}}\right]$
k_i	Integral gain	[−]
k_p	Proportional gain	[−]
L	Length scale	[m]
N_{mod}	Number of cells in a battery module	[−]
P	Pressure	[Pa]
P_{sat}	Saturation pressure	[Pa]
Q_{heater}	Cabin heater rate	[W]
R_i	Polarization resistance in the ECM	[Ω]
R_{th}	Thermal resistance	$\left[\frac{\text{m}^2\text{K}}{\text{W}}\right]$
T	Temperature	[K]
t^*	Duration of freezing flow solver	[s]
x_ω	Vapor mass fraction	[−]
C-rate	Charge/discharge current relative to the nominal battery capacity	$\left[\text{h}^{-1}\right]$
Gr	Grashof number	[−]
Le	Lewis number	[−]
Nu	Nusselt number	[−]
Pr	Prandtl number	[−]
Re	Reynolds number	[−]
Sc	Schmidt number	[−]

Thesis

This thesis consists of an extended summary of the following appended papers:

Paper A Ramesh Babu, A., Andric, J., Minovski, B., and Sebben, S. "System-Level Modeling and Thermal Simulations of Large Battery Packs for Electric Trucks". *Energies* **14**.16 (2021-01). Number: 16 Publisher: Multidisciplinary Digital Publishing Institute, 4796. ISSN: 1996-1073. DOI: 10.3390/en14164796. URL: https://www.mdpi.com/1996-1073/14/16/4796 (visited on 2023-01-04)

Paper B Ramesh Babu, A., Minovski, B., and Sebben, S. "Thermal encapsulation of large battery packs for electric vehicles operating in cold climate". *Applied Thermal Engineering* **212** (2022-07), 118548. ISSN: 1359-4311. DOI: 10.1016/j.applthermaleng.2022.118548. URL: https://www.sciencedirect.com/science/article/pii/S1359431122004999 (visited on 2023-01-04)

Paper C Ramesh Babu, A., Sebben, S., and Bark, T. "Effect of Cabin Insulation on the Heating Performance in EVs at Low Temperatures". *SAE WCX Conference*. Detroit, Michigan, United States: SAE Technical Papers, 2023-04. DOI: 10.4271/2023-01-0763. URL: https://www.sae.org/content/2023-01-0763 (visited on 2023-06-13)

Paper D Ramesh Babu, A., Sebben, S., Chronéer, Z., and Etemad, S. "An adaptive cabin air recirculation strategy for an electric truck using a coupled CFD-thermoregulation approach". *International Journal of Heat and Mass Transfer* **221** (2024-04), 125056. ISSN: 0017-9310. DOI: 10.1016/j.ijheatmasstransfer.2023.125056. URL: https://www.sciencedirect.com/science/article/pii/S0017931023012012 (visited on 2023-12-14)

Paper E Ramesh Babu, A., Sebben, S., Chronéer, Z., and Etemad, S. "Heating load reduction strategies for cabin and battery pack climatization in electric trucks operating in cold climates." *Submitted to Thermal Science and Engineering Progress* (2024)

Division of work

A The battery pack was modeled by Ramesh Babu in collaboration with Volvo Group Truck Technology (VGTT). The simulations and analysis were done by Ramesh Babu. The battery modeling parameters and the experimental data used to validate the model were obtained from VGTT. The first manuscript was written by Ramesh Babu and then discussed, reviewed, and revised by all authors.

B The modeling, simulation, and analysis were performed by Ramesh Babu. The electrical circuit battery model was provided by VGTT. The first manuscript was written by Ramesh Babu and then discussed, reviewed, and revised by all authors.

C The modeling, simulations, and analysis were performed by Ramesh Babu. The wind tunnel tests were performed by the climate team at VCC. The first manuscript was written by Ramesh Babu, and then discussed, reviewed, and revised by all authors.

D The cabin modeling, simulations, and analysis were performed by Ramesh Babu. The aerodynamic simulations were performed by Chronéer, VGTT. The first manuscript was written by Ramesh Babu, and then discussed, reviewed, and revised by all authors.

E The vehicle modeling, simulations, and analysis were performed by Ramesh Babu. The electrical circuit battery model and the experimental test data used for its validation were provided by VGTT. The manuscript was first written by Ramesh Babu, and then discussed, reviewed, and revised by all authors.

Other relevant publication

1. Ramesh Babu, A., and Sebben, S. "A 1D Model for Zonal Comfort Estimation and Control in a Passenger Car Cabin". *FKFS Conference on Vehicle Aerodynamics and Thermal Management*, Stuttgart, Germany, 2023-10.

Contents

Part I

Extended summary

1

Introduction[1]

This thesis is focused on saving energy by reducing the auxiliary loads of battery electric vehicles (BEVs), specifically for climatizing the battery packs and passenger cabins, when operating in cold weather.

The global annual greenhouse gas emissions are at an all-time high, with road vehicles constituting about 76% of the emissions from the transport sector in the European Union in 2021 [2, 3]. The emission cap for road vehicles has decreased with each new regulation. It is expected to reduce further in the coming years to combat the harmful effects of greenhouse gas emissions and climate change [4].

BEVs have gained significance over the past decade and are viewed as a promising transportation means instead of conventional vehicles driven by fossil fuels. BEVs also have low operating costs, high performance, and efficiency which appeal to the customers. More importantly, opportunities in the form of government subsidies, infrastructure, and funding have contributed to the shift in focus to develop and utilize electrified vehicles. As a result, electric vehicle sales increased five-fold in 2022, relative to 2018 [5].

Lithium-ion batteries (LIBs) have become the dominant energy storage device for the automotive industry as they have a high energy density, high power, excellent storage capabilities, and good cycling life as compared to other commercial battery technologies [6]. While these are compelling features, LIBs are limited by safety concerns associated with overheating leading to thermal runaway and explosion, poor performance at non-ideal operating temperatures, high cost, and aging. Batteries are electrochemical systems and their operating temperatures highly influence their performance. The ideal range for LIB operation is between 15°C to 35°C and operating them at lower temperatures results in poor performance [7]. Additionally, the passenger cabins must be climatized, which often requires a large amount of energy. The combined effects have been attributed to a significant loss in driving range in cold weather. This exacerbates the range anxiety already prevalent among customers and is a major deterrent to market penetration. Hence, improving the thermal efficiency and heat management in BEVs, along with strategies to reduce these auxiliary loads is essential to realize the full potential of the available energy.

1.1 Research objectives

This research project aims to increase the knowledge of the vehicle's energy expenditure for climatizing the battery packs and the cabin when operating in cold weather, and strategies for

[1] Parts of this thesis have been carried over from the Licentiate thesis [1]

reducing it. Three strategies were investigated during the project, namely,

- Cabin insulation
- Cabin air recirculation
- Battery pack encapsulation

Two main research questions were formulated:

1. How much do the cabin and battery heating requirements influence the energy consumption of BEVs at low ambient temperatures?
2. How do the investigated strategies (cabin insulation, cabin air recirculation, and battery pack encapsulation) reduce the heating load at the component level and consequently improve the vehicle range?

1.2 Limitations and constraints

- Although the reference models developed during the work were based on experimental data, the efforts were entirely numerical. Except for the fully insulated cabin of the passenger car, the modified configurations were not experimentally verified.
- A 1D modeling strategy was used for describing the battery pack to facilitate the simulation of different subsystems such as the vehicle power-train and cooling systems. Hence, the 3D effects of fluid flow and heat transfer were not captured in the 1D model.
- Complete vehicle simulations were only performed on the electric truck. The vehicle and system controllers were simplified and of low fidelity.

1.3 Thesis outline

This thesis consists of two parts: an extended summary and five appended papers.

Chapter 1 states the motivation, the objectives, and the limitations of the research project. Chapter 2 describes the literature survey containing background, and the various strategies employed to mitigate auxiliary energy consumption of the cabin and to improve battery performance. Chapter 3 presents the usage of cabin insulation and recirculating cabin air to reduce cabin heating load. Chapter 4 explores the effects of battery pack encapsulation under parked conditions. Chapter 5 presents a combined analysis of all the investigated strategies at the vehicle level, followed by some concluding remarks and future work in Chapter 6. Finally, Chapter 7 provides a summary of the appended papers.

Figure 1.1 gives an overview of the appended papers. The investigations on the battery pack were performed using a 1D modeling approach, while for the cabin, 0D and 3D methods were

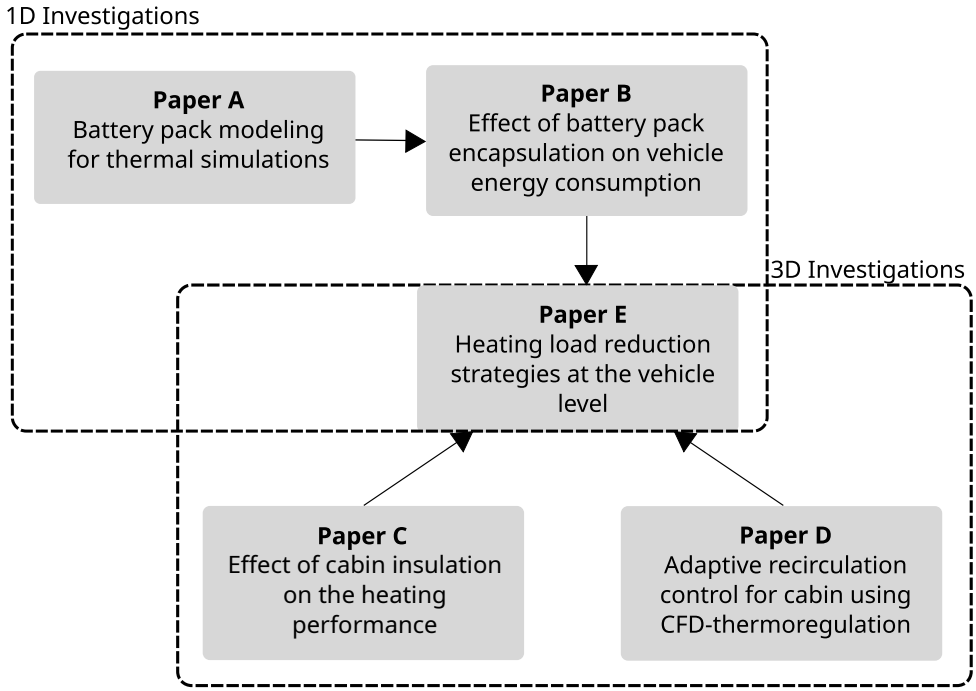

Figure 1.1: *Overview of the papers appended to the thesis. The arrows denote the flow of information between the papers.*

employed. Paper A describes a module-discretized battery modeling procedure to study the thermal behavior of large battery packs. Based on this approach, the battery pack encapsulation was investigated in Paper B. Heating load reduction strategies of the cabin were investigated in Paper C (insulating the passenger cabin) and Paper D (adaptive recirculation control). Finally, Paper E combines the findings of Papers B, C and D at the vehicle level.

2

Background

The transition to BEVs marks a shift in the automotive industry, promising cleaner and more sustainable transportation. However, this transition brings forth unique challenges, particularly in managing the thermal dynamics and its influence on the varying real-world performance. The vehicle thermal management system (VTMS) ensures that the components are climatized to the appropriate temperatures for improved energy utilization, extends their lifetime, and provides a hospitable cabin for the occupants. There is a strong interplay between the employed VTMS and the real-world performance of a BEV.

Several parameters influence the range of a BEV and can be broadly grouped into four factors [8]:

- Travel and roadway-related factors [9–13] such as distance, speed, travel time, travel route, traffic
- Environmental factors [14–17] such as ambient temperature, precipitation, wind effects
- Vehicle-related factors [18–20] such as vehicle mass, battery capacity, and auxiliary loads
- Driver behavior [21].

The environmental factors, specifically the ambient temperature, have a substantial impact on vehicle energy consumption. Several real-world tests have been conducted to illustrate this effect [14, 19, 20, 22, 23]. The results from these studies have been consistent in presenting an asymmetric curve for the vehicle energy consumption with varying ambient temperatures as seen in Figure 2.1 [14]. The energy consumption of a BEV is the lowest at around 20°C to 25°C, and increases in warmer and colder weather. For the poor low-temperature performance, several reasons have been put forth by studies such as high aerodynamic resistances owing to higher air density, high rolling resistance due to cold tyres, high auxiliary loads from the heating, ventilation, and air conditioning (HVAC) system, and poor battery performance [14, 23, 24]. The two latter effects are described briefly in the next section.

2.1 Low-temperature effects on BEV performance

2.1.1 HVAC energy consumption

The HVAC system is one of the largest auxiliary loads in the vehicle and ensures that the passenger compartment achieves good air quality, comfortable temperature, and relative humidity (RH) levels. In conventional internal combustion engine-powered vehicles (ICEVs), heat losses are

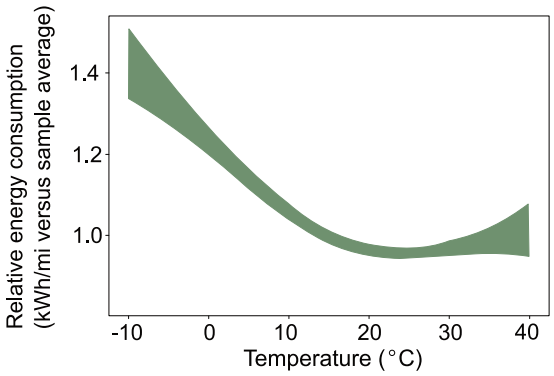

Figure 2.1: *Effect of ambient temperature on the BEV energy consumption. Data was extracted from the study by Taggart [14].*

high and energy is readily available for heating purposes. However, the power train in BEVs is more efficient than in ICEVs, which results in less waste heat being available in the cooling systems. For this reason, BEVs are equipped with an electric heater to heat the passenger compartment [25]. Since the energy utilized is from the vehicle's battery, this adds to the energy consumption of the vehicle.

Several studies have investigated the high energy demand of the cabin in cold weather. Zhang et al. [26] modeled the heating load of the climate system as ambient (energy loss to the environment), ventilation (HVAC heating), solar (heat gain from the sun), and metabolic (heat gain from the occupants) loads, and analyzed the effects of each load type on the energy demand. The metabolic and solar heat gains were negligible for their test cases. At the same time, the ventilation load accounted for about 70% of the total load at -20°C, and the rest was ambient load. The transient heating phase increased the influence of ambient load due to the cabin's thermal inertia [27]. The converse effect was noted in buses, where the ambient load was more dominant due to the large windows, and the constant opening and closing of the doors [28]. Yuksel and Michalek [22] aggregated data from over 7000 trips of Nissan Leafs across North America and reported an increase in the energy consumption of about 65% at -30°C as compared to 20°C. Taggart [14] performed a similar analysis on over 10,000 individual vehicles and demonstrated similar effects. Additionally, he showed that short trips particularly had larger penalties due to high cabin heating loads over small distances. Longer trips, however, amortize the energy expenditure over longer distances. Delos Reyes et al. [29] showed a drop in range of up to 70% at temperatures at -26°C as compared to 28°C. The authors saw an almost linear decrease in vehicle range when the ambient temperature decreased from 19°C to -15°C while the HVAC heating load increased linearly. Testing performed by Meyer et al. [30] using a dynamometer setup at -18°C/-20°C, showed a 50% drop in range with cabin heating as compared to 20°C. At -7°C, the use of cabin heating reduced the range by 25% as compared to no cabin heating. Steinstraeter et al. [19] found a maximum decrease of about 50% due to heating demand and limited battery recuperation. Their results showed that about 32% of the net energy for a trip was spent on cabin heating, which was in line with other literature [31, 32], and about 22% of energy was lost due to poor battery performance.

As seen, the above studies show that the HVAC load causes a significant decrease in range for BEVs while operating in cold weather, largely due to the high ventilation load. The thermal

inertia of a cold cabin increases the ambient load during the initial phase of heating.

2.1.2 Battery performance

During operation, the lithium ions in a battery cell are transported between two electrodes (cathode made of a lithium compound and anode made of a carbonaceous compound [33]), through an electrolyte and a separator, while transferring electrons through an external circuit and current collectors. The direction of the transported quantities characterizes charging and discharging.

As mentioned, batteries are electrochemical systems whose operating temperatures significantly influence their performance. Numerous studies have attempted to investigate the performance of LIBs at low temperatures and have noted decreased energy and power capabilities. Nagasubramanian [34] studied the performance of commercially available 18650 Li-ion cells at different temperatures ranging from 25°C to -40°C. He reported a drop in the energy density down to 5% and power density to 1.25% at -40°C as compared to 25°C. At -10°C, Ji et al. [35] noted a 23% and 59% drop in available capacity at 1C and 4.6C discharge rates at the cell level, respectively. This illustrates that the low-temperature cell performance depends both on the operating temperatures and discharge rates. The reason for this behavior was attributed to the low ion diffusivity through the electrolyte in cold environments, causing high internal resistance.

Another reason for the observed effects was described by Zhang et al. [36], where they linked the behavior to the high charge transfer resistance at the electrode/electrolyte interfaces due to slow kinetics. Additionally, they demonstrated high charge-transfer resistance and anode polarization at low states of charge (SoC), thus affecting its charging performance. This meant that charging a discharged cell was more difficult than discharging a charged cell [37] at low operating temperatures.

The negative polarization of the anode at low temperatures is one of the primary reasons for lithium plating as demonstrated by Waldmann et al. [38]. Lithium plating is characterized by the deposition of metallic lithium on the anode surface and leads to capacity loss by interfering with the intercalation of lithium between the anode and electrolyte. The deposited lithium effectively reduces the amount of active material that is cyclable, causing an irreversible drop in the capacity and lifetime of the cell. Fan and Tan [39] studied the charging characteristics at low temperatures and found that lithium plating occurred at low temperatures and SoC when charged at high C-rates. They recommended charging with low C-rates, under 0.2C, when operating at -20°C. Furthermore, plating in the form of dendrite could grow and penetrate through the separators, resulting in an internal short-circuit [33, 40], which is also a safety hazard.

Thus, the main mechanisms for the poor low-temperature battery performance can be summarized as follows [41–43]:

- Increased resistance due to low electrolyte and interfacial conductivity.
- Sluggish kinetics caused by high charge transfer resistance, and slow solid-state Li-ion diffusion.
- Polarization of the anode results in lithium plating, reducing capacity and lifetime.

2.2 Strategies for improved energy efficiency

2.2.1 Integrated thermal management strategies

The thermal management strategies at the component level aim at ensuring comfortable cabins and aiding the batteries to operate at the maximum available capacity. To fully utilize the available energy in the vehicle, integrated solutions are necessary to allow for energy transfer from one component to another. Lei et al. [44] divided the integrated thermal management strategies into air-side, refrigerant-side integration, and waste heat recovery schemes.

The air-side integrated schemes use the heat from the battery pack to heat the air going into the cabin [45], when the heat production is close to the HVAC heat requirement. This approach has been carried over from ICEVs where this energy was abundantly available. The refrigerant-side integrated schemes employ either switching valves in the refrigerant loop or secondary loop integration schemes. In secondary loop schemes, the battery coolant circuit is connected to the refrigerant circuits. In BEVs with large battery packs, a chiller is equipped to cool the battery pack using the refrigerant system. The chiller can either be placed in series or parallel to the evaporator in the refrigerant loop [25, 46, 47]. Zhang et al. [48] employed such a system in heat pump mode, which resulted in better performance under the heating mode, as compared to a positive thermal coefficient (PTC) heater. In the waste heat recovery schemes, waste heat from batteries, motors, and electronics is collected for cabin heating on the refrigerant side or air side. Han et al. [49] used the waste heat from the batteries to heat the cabin and increased the heating capacity and coefficient of performance of the heat pump. Meanwhile, Suh et al. [50] employed the waste heat from the motors and demonstrated a 25% drop in energy consumption. Ahn et al. [51] used a dual-source heat pump that derived heat from air and waste heat. They pointed out that the use of waste heat greatly improved the capability of the systems when deriving heat from the air was not possible.

Thus, by enabling such systems, the cooling needs are met for components producing heat, and heating demands are met for the cabin, which typically requires enormous energy in winter.

2.2.2 Cabin climatization strategies

In the context of reducing the energy consumption for cabin climatization, all strategies typically fall into two approaches [52]. The first approach includes strategies to reduce energy requirements (ventilation and ambient loads), such as localized zonal climatization [53], reflective glazing [54], thermal insulation [55–57], and recirculating cabin air [58–60]. The second approach includes strategies to provide the required energy efficiently with the use of heat pumps, and waste heat recovery systems, as discussed earlier [51, 60–62].

The ventilation load occurs when the HVAC system takes the outside air and treats it to the desired state to maintain good air quality, thermal comfort, and defog/defrost the windscreen. Recirculating cabin air is an efficient way to reduce this load by taking air from the climatized cabin to the HVAC. This has shown to reduce the HVAC load between 7% and 48% in summer [63]. In cold climates, however, other considerations are necessary. The occupants present inside the cabin generate CO_2 and moisture (through respiration and sweating). At low ambient temperatures, when the windshield temperature is lower than the dew point temperature of the

air next to it, the moisture in the air condenses as fog on the surface. This reduces visibility for the driver and is detrimental to their safety. Thus, to prevent such conditions many automobile manufacturers refrain from using recirculation, thereby increasing the energy spent. Wei et al. [64] studied different recirculation levels at 0°C and recommended not to use recirculation when the vehicle had more than three passengers.

Several anti-fog measures have been investigated. Urbank et al. [65] developed an integrated dew point and glass temperature sensor that detects the presence of fogging. Based on the presence of fog detected through the sensor, the control systems operated to defog by reducing recirculation, increasing defroster flow, and so on. Shikata et al. [58] proposed the concept of a two-layer HVAC where the fresh air and recirculated air were not mixed. They were heated separately and supplied, with the fresh air delivered to the defrosters and the recirculated air discharged at the floor outlets. The recirculated air heating requirements were reduced, decreasing the total HVAC heating demand. Hirai et al. [59] were among the pioneers to perform recirculation control with anti-fog measures and demonstrated about 30% energy savings with experimental testing. A similar approach was taken by Zhang et al. [60] where they employed a continuous anti-fog curtain, such that the air from the defroster has a lower dew point temperature than the windshield temperature. They investigated the use of recirculation under various steady-state operating conditions and demonstrated up to 68% reduction in heating demand. Lorenz et al. [66, 67] analyzed several discrete recirculation ratios and showed that fogging at -10°C and 70% RH with two passengers in the vehicle. They also investigated several configurations with heated seats, windows, and panels with reduced HVAC heating, that saved about 57% of the baseline energy demand. Pan et al. [68] considered both fogging and CO_2 using a simplified thermal model and employed the strategy that required higher fresh-air intake. Their study showed that utilizing recirculated air reduced the heating demand between 14% to 46% compared to the baseline. Norin [69] proposed double pane glazing to significantly raise the inner surface temperature of the windshield to avoid window fogging and improve passenger comfort. Additionally, antifog coatings, that are hydrophilic have been studied [70]. These materials strongly interact with water drops to form a continuous or nearly continuous thin film of water on the solid surface. As a result, incident light transmits without being scattered. Hence, even if condensation persists, the surface remains optically clear. However, Lorenz [67] noted that the buffering capacity of these coatings is limited, and their cost-effectiveness and susceptibility to damage make them not ideal for standard automotive applications.

Studies on reducing ambient loads aim at decreasing the parasitic heat loss to the interior thermal masses and the ambient to reduce the heating demand. Oiwake et al. [56] investigated the effect of glass and body heat transfer characteristics on the energy demand and found that reducing the heat conduction coefficient by 90% resulted in about 30% fuel savings. Gasworth and Tankala [54] proposed polycarbonate glazing to reduce the heating load as its thermal conductivity is 80% lower than glass. Jeffers et al. [53] studied the effect of polycarbonate glass glazing and foam insulation on different surfaces. They found up to 18.3% reduction in steady-state heating load at -5°C. The major benefit was from reducing the thermal conductivity of the cabin shell. However, in their prior work [71] under warm conditions, they saw a marginally higher roof temperature during a heat soak. Upon cooling, little benefit was seen in the energy consumption as compared to the case without insulation.

2.2.3 Battery thermal management strategies

To mitigate the low-temperature effects of LIBs, many avenues have been explored at the cell, and pack levels. Studies have investigated the use of electrolytes, electrolyte additives, and electrodes which have improved ion diffusivity and low activation energy [72–74]. While these improve the low-temperature performance, lithium plating could still occur, and the available capacity is lower than that at ideal operating temperatures.

To preserve the battery pack's lifetime, many BEV manufacturers disable/limit charging at subzero temperatures in the battery management system (BMS) [19, 20]. The BMS does not allow the cold battery pack to recuperate energy under braking. Preconditioning them to optimum temperature before they are cycled is commonly practiced in BEVs. The main criteria for the selection of the appropriate heating system are (a) heating time; (b) the power consumption; (c) the overall cost of the system; and (d) the complexity of design [33]. Typically the heating methods can be categorized into two types based on the origin of heat energy: external and internal heating [7, 35].

External heating systems use a heat source outside the battery cells to generate the majority of the heat used for the battery warm-up [41]. Some examples are liquid heating, resistance heating, phase change material (PCM) heating, and so on. In modern BEVs, the indirect liquid battery thermal management system (BTMS) approach is employed, where the batteries are climatized by letting coolant flow through jackets/plates with channels [7, 75, 76]. Liquid heating employs coolant heaters, such as PTC heaters powered by batteries to heat them. Studies have focused on improving the design of the coolant channels for good uniformity [75, 77, 78] and fast heat transfer from the coolant to the batteries [79]. PTC heaters are fastened to the surface of the cells, or between two cells to heat them through conduction in resistance heating. This method has high heating efficiency, short heating time, and low energy consumption on prismatic cells [80, 81], but requires space for installation in the battery packs and increases the weight significantly. PCMs are energy storage materials that absorb and release heat through melting and solidifying at a certain temperature. PCMs aid the batteries in maintaining temperature with the available thermal energy stored as latent heat when the ambient temperature is low [82, 83].

Internal heating systems warm up the cells within the packs, requiring no external heat transfer medium. Some examples are internal self-heating, mutual pulse heating, and alternation current heating. The internal self-heating method employs internal resistance and a discharging current profile, typically based on constant voltage discharge, to heat the cells [84, 85]. However, due to the nature of the heating, energy loss is seen which makes this suitable only when the initial SoC levels are relatively high. Mutual pulse heating uses alternative charge/discharge processes between the battery and another energy storage device [86–89]. The energy loss is relatively low, but the system complexity is high, and the long pulses at high SoC levels can lead to lithium plating [41]. Heating with external power sources eliminated the need for energy consumption from the battery pack, thus extending the driving range. Hand and Stuart [90, 91] proposed a method to heat the batteries with alternating load current. Different amplitudes and frequencies of the alternating current were tested and they found that a frequency of 10-20 kHz and high amplitudes decreased the heat-up time significantly. Additionally, Zhu et al. [92] found that the waveforms of the alternating current also had a significant impact on the heating efficiency of

LIBs.

While heating with external power sources is best suited for BEVs from a range standpoint, it is impractical to rely solely on them to climatize the batteries. So, vehicles are equipped with coolant heaters upstream of the batteries to heat them when required. Hu et al. [41] pointed out that effective insulation can reduce heat loss to the environment, thus reducing energy expenses during the warm-up phase. Ling et al. [93] investigated the effect of PCM with high thermal capacitance to store heat. It was noted that the usage of PCM decreased the rate at which the cells cool down, but negatively affected the heat-up performance of already cold battery cells, which is in line with the conclusions from Ghadbeigi et al. [83]. Ouyang et al. [94] carried out a series of experiments to probe the influence of thermal insulation around battery cells for the temperature range 0-20°C and concluded that thermally insulated cells showed improved discharge performance and a slower decay rate. Wu et al. [95] examined the effect of thermal insulation using nano-porous aerogel with different thicknesses in battery cells. The low thermal diffusivity of the aerogel aided in retaining heat in the cells at low temperatures resulting in better energy utilization.

As described in the research objectives in section 1.1, the thesis includes three strategies, namely cabin insulation, cabin air recirculation, and battery pack encapsulation.

- Cabin insulation - for reduction of ambient load
- Cabin air recirculation - for reduction of ventilation load
- Battery pack encapsulation - for slowing down battery pack cool down

These strategies have been investigated at the component and vehicle levels and will be discussed in the upcoming chapters.

3

Load reduction methods for cabin climatization

This chapter focuses on the strategies for reducing the ambient and ventilation loads of the HVAC. First, the effects of cabin insulation on reducing the ambient load on a passenger car are discussed (Paper C). Then, the effects of using recirculation to reduce the ventilation load on a truck are presented (Paper D). Finally, the combined effects are evaluated on the truck.

Each section addresses the geometry, the simulation methodology, and the results. All 3D CFD simulations were performed in STAR-CCM+.

3.1 Reduction of ambient load using cabin insulation

3.1.1 Vehicle geometry and numerical setup

The vehicle considered in the first study was a full-scale SUV-BEV. The CAD included both the interior and the exterior geometry so that heat transfer from the air in the cabin to the solids and ambient air could be accounted for while the vehicle is in motion. All the interior cabin solids that were in direct contact with the cabin air were considered as seen in Figure 3.1, where the solids are grouped and colored based on their properties, which are given in Table A.1 in Appendix A. There were several inlets into the cabin from the HVAC system. These are illustrated in Figure 3.2. Each inlet was prescribed an inlet mass flow rate and temperature. The evacuation outlet was taken downstream of the cabin around the luggage cover (S10) in Figure 3.1a.

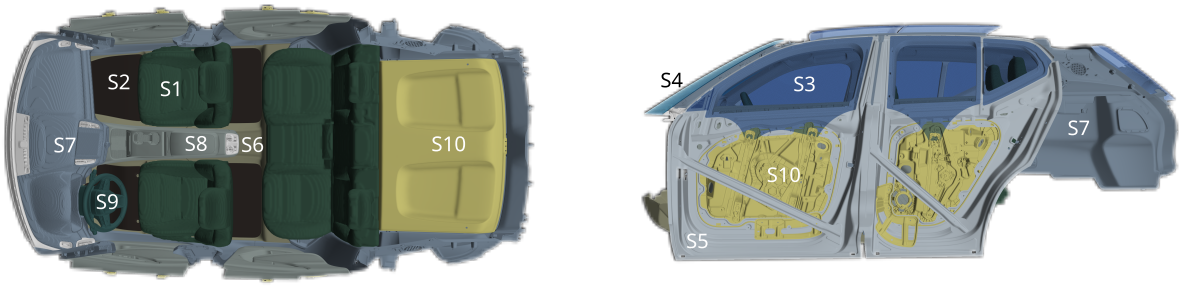

(a) *(b)*

Figure 3.1: *Cabin solids colored based on the corresponding material property from Table A.1 in Appendix A (a) Top view; (b) Side view.*

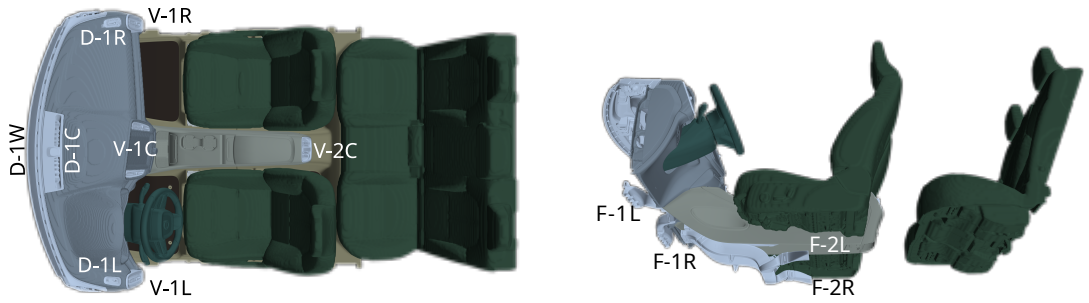

(a) *(b)*

Figure 3.2: *Inlets in the cabin from the HVAC coded according to: inlet type (defroster-D, vent-V or floor-F), row number (1 or 2), and location (center-C, left-L, right-R or windshield-W). (a) Top view; (b) Side view.*

The internal volume of air in the cabin and door gaps was modeled as a gas with constant density during domain initialization and as an ideal gas during heating. The variations in the dynamic viscosity and thermal conductivity due to temperature were accounted for using Sutherland's law. The realizable $k-\epsilon$ (URANS) turbulence model was used since it was shown to be the most robust in the literature according to [96, 97]. Gravity was taken into account to capture buoyancy effects during heating. However, solar radiation was neglected in these simulations since this effect is generally low in cold weather [52, 98].

The vehicle was placed in an open-road setup (a rectangular domain) of dimensions $15.7L\times$ $8.9L\times$ $6.7L$, where L is the length scale, i.e. the vehicle length, to simulate external flow under driving conditions. The exterior air had a constant density, corresponding to the ambient pressure and temperature. The inlet was located $4.5L$ upstream of the vehicle, where a uniform velocity equal to the vehicle velocity and ambient temperature were prescribed. The same velocity was used on the ground, with a moving wall boundary condition to achieve the desired relative motion between the vehicle and the ground. The outlet was modeled as a pressure outlet boundary condition with a gauge pressure of 0 Pa and the same temperature as the ambient. The top and the side walls of the domain were prescribed a zero-gradient condition. Conjugate heat transfer (CHT) interfaces were used on the vehicle boundaries where the solids were modeled namely, the front and rear windshields, the windows, the sunroof, and the door. All the other surfaces of the vehicle were modeled as adiabatic walls. The exterior flow was modeled using the SST $k-\omega$ (RANS) turbulence model.

Both RANS models for interior and exterior air used 'All y^+ wall treatment' to compute the wall shear stress, heat flux, and near-wall turbulent quantities. This approach has been recommended for complex geometries and uses a continuous function to model the transported quantities close to the wall [99].

Simulating cabin heat-up is challenging as it takes a long physical time, and an transient approach is required. The flow in the cabin, once developed, was locally steady when the boundary conditions were kept constant. This was confirmed by monitoring the velocity fields on probes at the head, midsection, and feet levels of the driver, the front passenger, and the

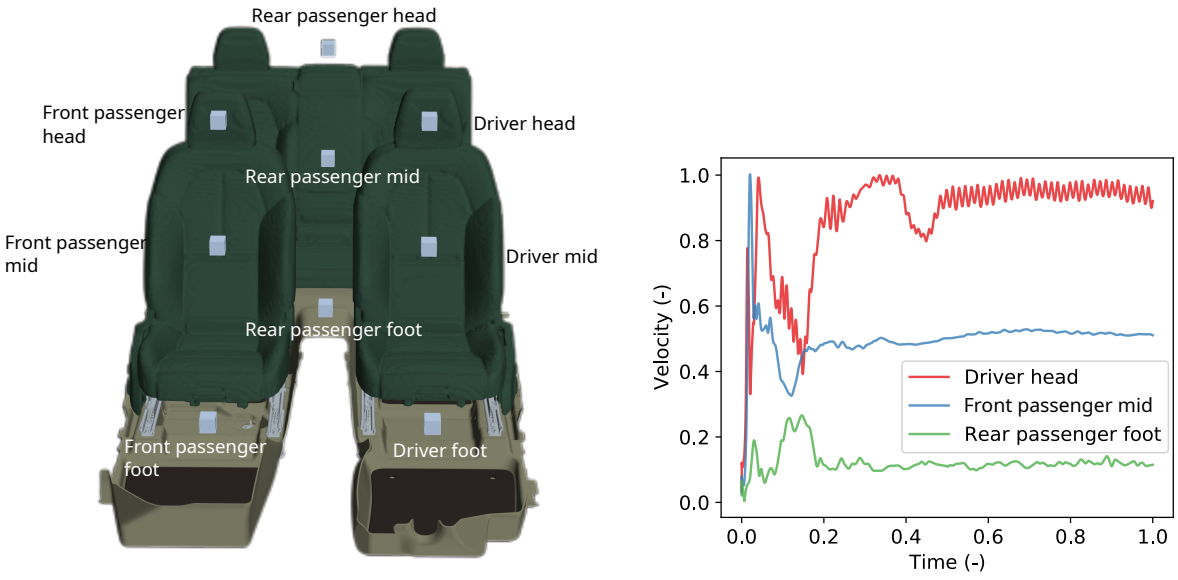

(a) *(b)*

Figure 3.3: *(a) The location of nine monitor volumes used in the simulation; (b) Normalized velocity vs time in three monitor volumes. The values were normalized to the maximum instantaneous driver head velocity and the heat-up time.*

rear passenger, Figure 3.3a. The velocities at a few monitors are plotted in Figure 3.3b, but the same effect was observed on all other monitors. Thus, by freezing the continuity and momentum equations for a certain duration, t^*, and solving only the energy equation with a coarser time step, Δt^*, simulating cabin heat-up becomes more affordable. The flow needed to be intermittently unfrozen to facilitate convergence and to account for the varying buoyancy effects due to changing temperatures in the cabin.

Four numerical sensitivity studies were systematically performed:

1. a mesh study,
2. a time-step study (Δt) when all transport equations are solved,
3. a time study for the duration (t^*) of freezing the flow solver,
4. a time-step study (Δt^*) during frozen flow.

The results of the numerical sensitivity analyses are presented in detail in Paper C. The medium mesh with about 120 million polyhedral cells in the cabin air and solid domains was deemed to be sufficient. The meshing strategy for the exterior flow followed the recommendations of studies used for vehicle aerodynamics [100, 101], with about 200 million hexahedral cells. Both the interior and exterior meshes were refined with several prism layers that resulted in a wall $y^+ \approx 1$, to capture the velocity and thermal boundary layers accurately. Figure 3.4 illustrates a

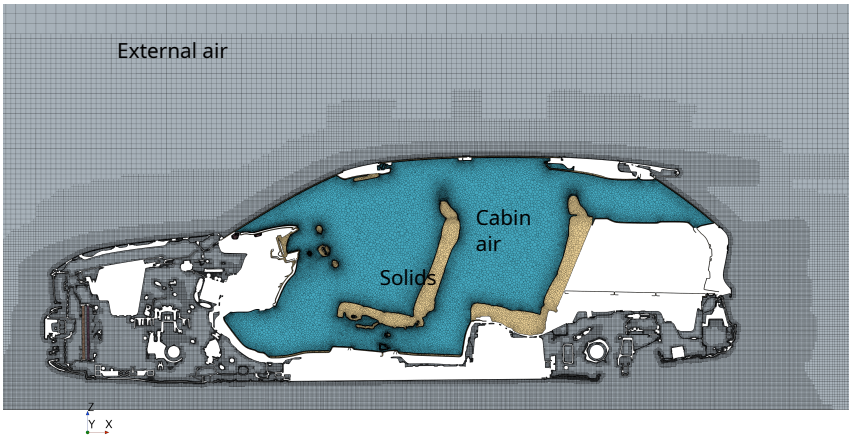

Figure 3.4: *An XZ-mesh section at Y = -0.25 m with the three computational domains colored based on the domain type: external air in grey, cabin air in turquoise, and cabin solids in yellow.*

section of the mesh at Y= − 0.25 m, along the centre of the driver's seat. From the time-step studies, $\Delta t = 0.02$ s while solving all transport equations, $t^* = 9$ s for the duration of freezing the flow solver, and $\Delta t^* = 0.25$ s as the time-step for the energy solver when the flow solver was frozen, were found to be the best compromise between accuracy and computational resources.

The simulation procedure is sketched in Figure 3.5, describing the various steps to simulate the transient cabin heat-up. The first step was to set initial and boundary conditions such as the ambient, inlet, and initial temperatures in the domains, mass flow rates at the cabin inlets, vehicle velocity, and cabin insulation. A steady-state simulation of the external flow was performed. The heat transfer coefficient distribution computed on the external boundaries of the car was mapped as the convective boundary condition for the solids. Then, the internal cabin air was initialized with a steady-state simulation with constant-density air. The steady-state simulation was used to reduce computational effort. The solver was then set to run an unsteady simulation, with the ideal gas model and gravity. The fully unsteady conjugate heat transfer simulation was performed for the internal cabin air and the solid domains with the time step (Δt) 0.02 s, till steady velocity values were obtained in the monitor volumes, which typically took about 10-20 s. Once a local steady-state was achieved, a loop was set up with two conditional statements. The first condition was a time-based stopping criterion to terminate the computation if the total time (40 minutes) was achieved. The second condition was to re-compute the external flow and the heat transfer coefficients on the outer CHT interfaces every five minutes. While testing the method, it was noted that the heat transfer coefficient on the outer walls was largely affected only by the vehicle velocity for speeds above 5 km/h. However, at low vehicle velocities or stand-still conditions, a mixed/natural convection regime occurred which made it necessary to update the wall heat transfer coefficient more often with changing wall temperatures. Then, the final step of the loop involved freezing flow intermittently and solving only the energy equation for $t^* = 9$ s with the time step $\Delta t^* = 0.25$ s, and then all the transport equations were solved for 1 s with the time step $\Delta t = 0.02$ s.

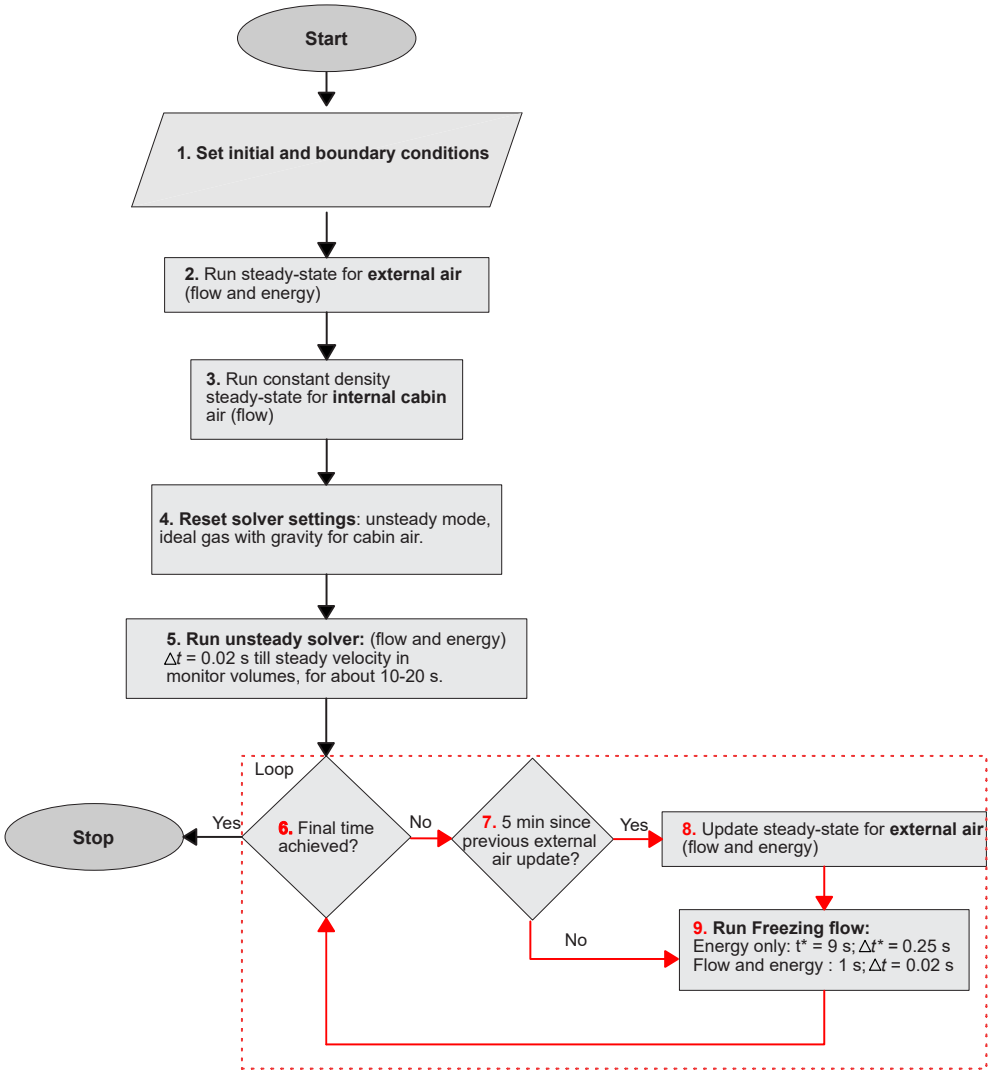

Figure 3.5: *Numerical framework to simulate passenger car cabin heat-up while driving.*

Simulation scenario

The scenario studied was a passenger car being heated up for 40 minutes while being driven at 50 km/h and -7°C ambient temperature after a fully soaked condition. The mass flow of air prescribed at the cabin inlets is presented in Table 3.1, with the same naming convention as used in Figure 3.2. A constant heater power was employed during an experimental campaign performed in a climatic wind tunnel at VCC, and the corresponding inlet temperatures were collected using thermocouples at each inlet location, as shown in Figure 3.6. The temperature at the window defrosters (D-1W) was not measured, so the temperatures from the left and right defrosters were used accordingly on the boundary.

The insulation material used in the study was 3M Thinsulate, which has a thermal conductivity of 0.05 W/mK and a density of 8 kg/m^3. Due to the low density, the mass of the added insulation was negligible in comparison to the other solids in the cabin. Hence, in the CFD simulations, the insulation material was modeled through thermal resistance, R_{th}, imposed on the interfaces

Inlet	Mass flow (kg/s)
D-1C	0.0079
D-1L	0.0007
D-1R	0.0007
D-1W	0.0019
V-1L	0.0038
V-1R	0.0039
V-1C	0.0016
V-2C	0.0013
F-1L	0.0074
F-1R	0.0076
F-2L	0.0044
F-2R	0.0049

Table 3.1: *Mass flow at the cabin inlets: See Fig.3.2 for their locations.*

between the cabin air and the solids.

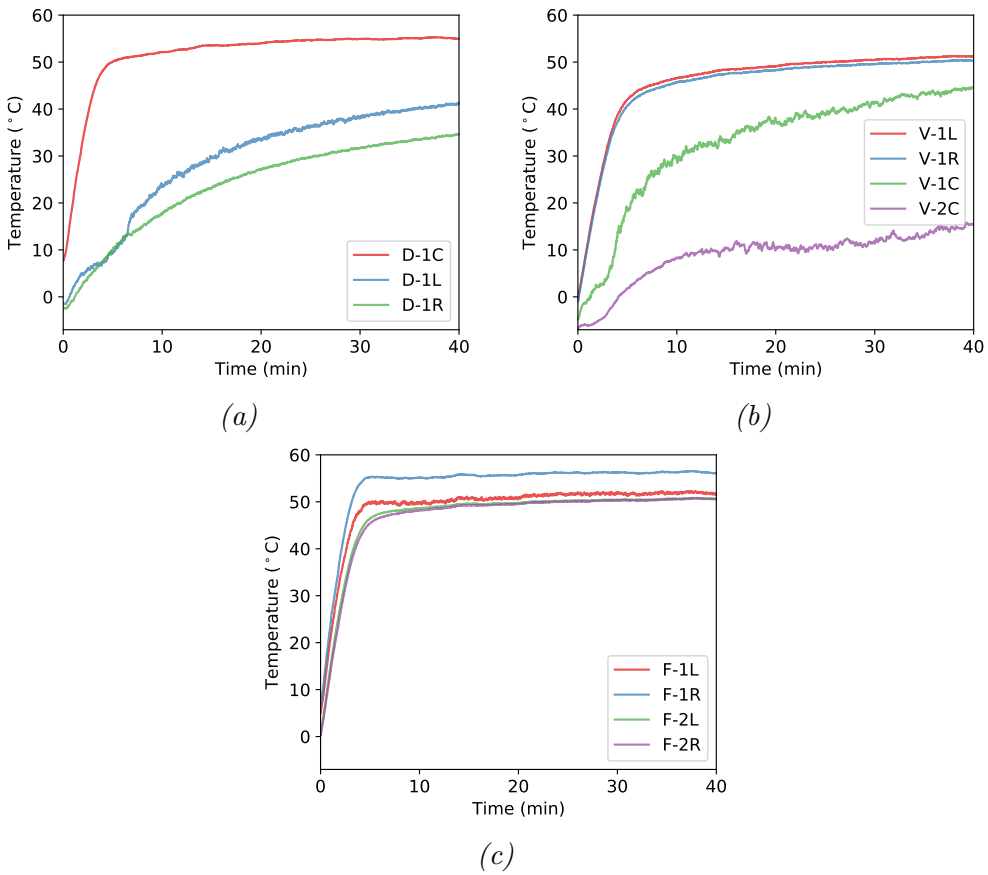

Figure 3.6: *Temperature at the cabin inlets obtained from measurements: (a) defroster; (b) vent and (c) floor.*

3.1.2 Heating performance of the insulated cabin

Two studies were performed: 1) the choice of insulating surface; and 2) the magnitude of insulation resistance. The first study involved configurations where different interior surfaces were insulated separately, namely the roof, seats, door panels, pillars, and dashboard console. Then, a fully insulated configuration where all the above-mentioned surfaces were insulated together. For the first study, a thickness of 41 mm was considered for the insulating material, which resulted in a thermal resistance of 0.82 m^2K/W. For the second study, with the fully insulated design, four insulation resistances, 0.41, 0.82, 1.64, and 3.28 m^2K/W were investigated.

Effect of insulation surface

The six configurations with insulation were compared to a baseline, without any insulation. Figure 3.7 shows the average cabin temperature during the 40-minute heating phase. It can be seen that the average temperature is higher for all configurations with insulation as compared to the baseline. The insulated configurations also exhibit faster heat-up rates for the same heating load, to reach 20°C. The fully insulated configuration takes only about 7.5 min, while the baseline configuration takes about 23 min. This benefit is twofold: lower time to reach a comfortable temperature and lower energy expenditure to attain the desired state. Among the configurations with insulation, fully insulating the cabin provides the maximum mean cabin temperature rise of about 5.6°C higher than the baseline, followed by seat insulation of about 2.3°C higher than the baseline. This is in line with the results observed in [102] where the temperature of the seats strongly affected the air temperature due to their large thermal mass. Insulation on all other surfaces results in a smaller mean temperature increase.

Figure 3.8 presents the variation in the net heat transferred as a consequence of insulating the different surfaces as compared to the baseline. Insulation reduces the heat transfer on the corresponding surfaces as expected, thus increasing the cabin temperature. Since the heat transfer rate is directly proportional to the difference in temperatures between the surfaces and the cabin air, it increases the net heat transferred to the non-insulated surfaces. This effect is observed in the carpets, the seat rails, the windows, and the windshields. This is also the reason that surfaces in the fully insulated configuration experience a slightly lower reduction in the net

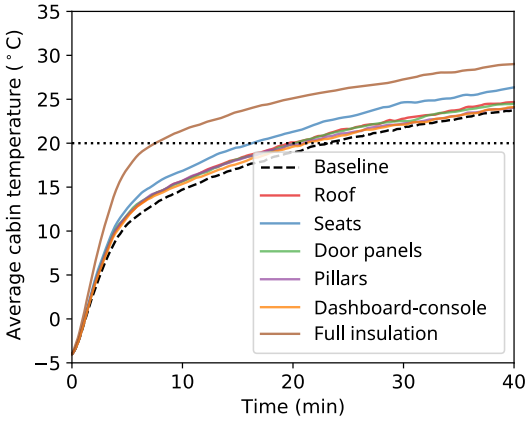

Figure 3.7: *Effect of insulating cabin surfaces on the average cabin temperature.*

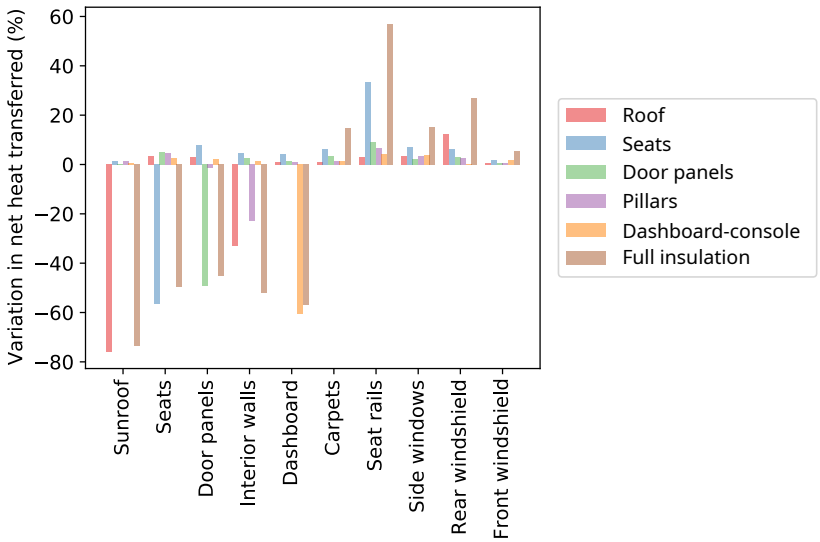

Figure 3.8: *Effect of insulating cabin surfaces on the variation in the net heat transferred to the cabin solids.*

heat transferred as compared to their insulated counterpart. The 'Interior walls' surface in the plot includes both the roof and the pillars. It can be seen that the roof insulation contributes to a larger reduction in heat transfer to the walls than insulating just the pillars since warmer air rises to the top of the cabin. So, insulating it reduces a greater proportion of heat transfer than insulating just the pillars.

Effect of magnitude of insulation resistance

Figure 3.9 shows the average cabin temperature during heat-up for the baseline and the fully insulated configurations with four different resistances. As expected, the cabin temperatures increase with increasing thermal resistance. As before, the rate at which the cabin heats up is higher for the insulated configurations as compared to the baseline. However, the heating rate for

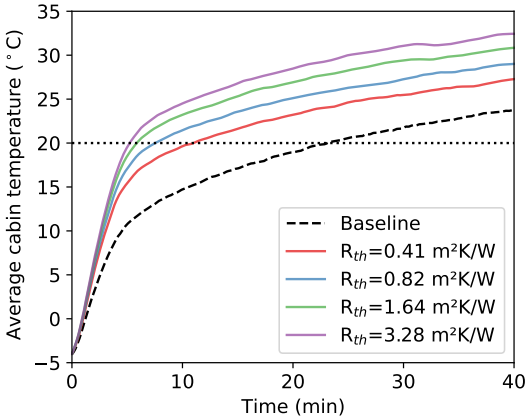

Figure 3.9: *Effect of varying magnitudes of insulation resistance on the average cabin temperature vs time.*

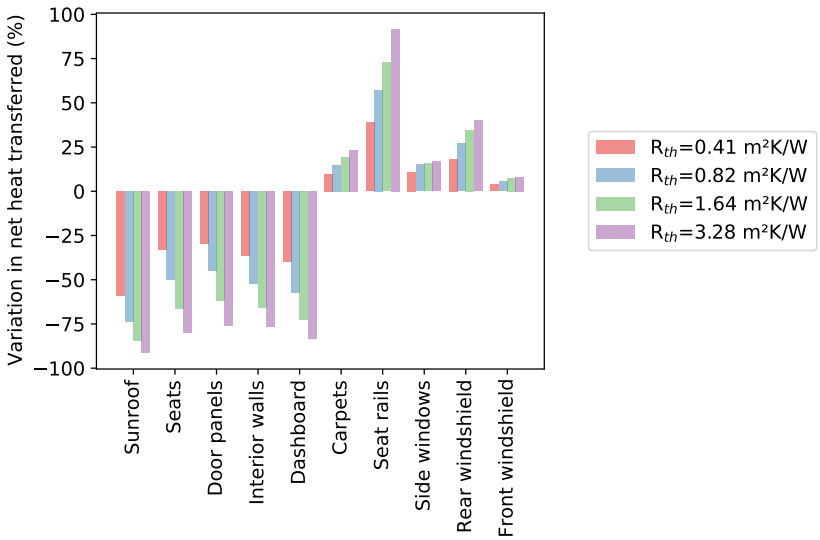

Figure 3.10: *Effect of varying magnitudes of insulation resistance on the variation in the net heat transferred to the cabin solids.*

the configurations with insulation is very similar over the first few minutes. The cabin heat-up rate rises by 20% while increasing the insulation resistance from 0.41 m^2K/W to 3.28 m^2K/W over the first five minutes. Nevertheless, this results in the configuration with 3.28 m^2K/W insulation reaching 20°C within 5.2 min, the 0.41 m^2K/W configuration within 11 min, and the baseline requiring double the latter time. Thus, increasing the insulation thermal resistance reduces heat loss, and accelerates the process to reach the desired temperature, thereby reducing energy expenditure.

In Figure 3.10, the variation in the heat transferred through the different surfaces is presented. As expected, increasing the insulation resistance decreased the net heat transferred through the insulated surfaces, thereby increasing the cabin temperature. The heat transferred through the non-insulated surfaces increased as a consequence of the higher cabin temperatures as seen in the previous subsection.

For transient heat-up, adding resistance causes a temperature rise resulting in a larger temperature difference, thus increasing the heat transfer on non-insulated surfaces as seen earlier. The rate of increase in the mean temperature rise drops with the insulation resistance, for the given scenario, and hence there should exist a critical value of thermal resistance beyond which the increase in temperature is marginal. So, using the available data, a curve-fit $f(R_{th})$, was generated as shown in Figure 3.11, where the mean temperature rise as compared to baseline was defined as a function of the insulation resistance. The configuration $R_{th} = 0$ m^2K/W represents the baseline configuration. The four insulation values discussed above were used to create the curve-fit function, referred to as 'Numerical: Fit'. An additional computation for $R_{th} = 20$ m^2K/W was performed to evaluate the curve-fit function. The error between the actual value and the one obtained from the curve-fit function is 0.24°C. The maximum mean cabin temperature increase that can be obtained is about 11°C higher than the baseline configuration for the scenario considered. The increase is marginal beyond a thermal resistance of 4 m^2K/W, which already produces about a 9°C increase in mean temperature.

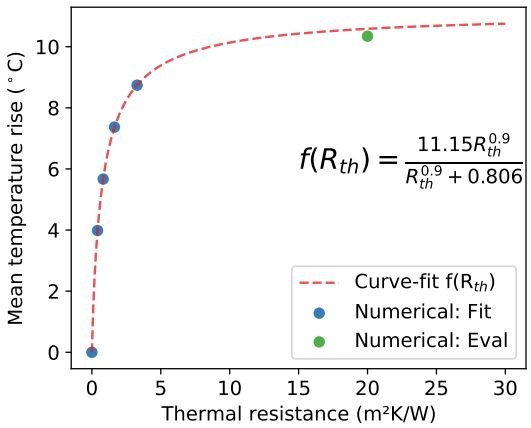

Figure 3.11: *Mean temperature rise of the fully insulated configuration relative to the baseline presented as a function of the insulation thermal resistance (R_{th}).*

Insulation configuration	**Reduction in heater energy spent** (%)
Dashboard console	8.85
Wall	9.60
Door	13.1
Roof	15.9
Seat	30.7
Full insulation - 0.41 m^2K/W	54.4
Full insulation - 0.82 m^2K/W	70.0
Full insulation - 1.64 m^2K/W	77.6
Full insulation - 3.28 m^2K/W	80.4

Table 3.2: *Percentage reduction in energy spent to heat the cabin from -7°C to 20°C with a constant heating power.*

Table 3.2 summarizes the reduction in heating energy spent to reach a mean cabin temperature of 20°C, for each insulation configuration relative to the baseline cabin. This trend can be viewed as potential energy saved during heating to achieve 20°C. However, it must be noted that the presented values are specific to a constant heating rate and for this specific scenario. In Section 3.2, which covers the work in Paper D, a heater was modeled using a controller. This made it possible to evaluate energy savings over a given time of operation.

3.1.3 CFD validation with experimental data

The baseline and fully insulated (with $R_{th} = 0.82$ m^2K/W) configurations were experimentally tested by the climate team at VCC in a climatic tunnel for the same conditions used in the numerical simulations, i.e, the car driven at 50 km/h and -7°C ambient temperature. The experimental setup of the fully insulated configuration had the insulating material fastened to the different surfaces as shown in Figure 3.12. To compare the two configurations effectively, the air heater power, the HVAC flap angles, and blower settings were kept constant and the re-circulation mode in the cabin was deactivated. The inlet temperatures were measured using thermocouples at the end of the inlet ducts for both configurations, as seen in Figure 3.6.

Figure 3.12: *Experimental setup of the fully insulated cabin.*

Eight K-type thermocouples were set up in the vehicle cabin to capture the air temperatures during the heat-up, see Figure 3.13. Four were placed about 10 cm in front of the headrests of the front and rear passenger seats (T1-T4), and the other four (T5-T8) behind the rear seat's headrest. Figure 3.14 compares the results of the numerical model and the measurements during the heat-up scenario, for four of the thermocouples. As seen, both configurations agree very well with the measurements, except T7 (and T8, shown in Paper C) for the baseline configuration, where the temperatures are over-predicted by about 4°C. Further analysis can be found in Paper C.

Figure 3.13: *Positions of thermocouples (T1-T8) placed in the car during experiments.*

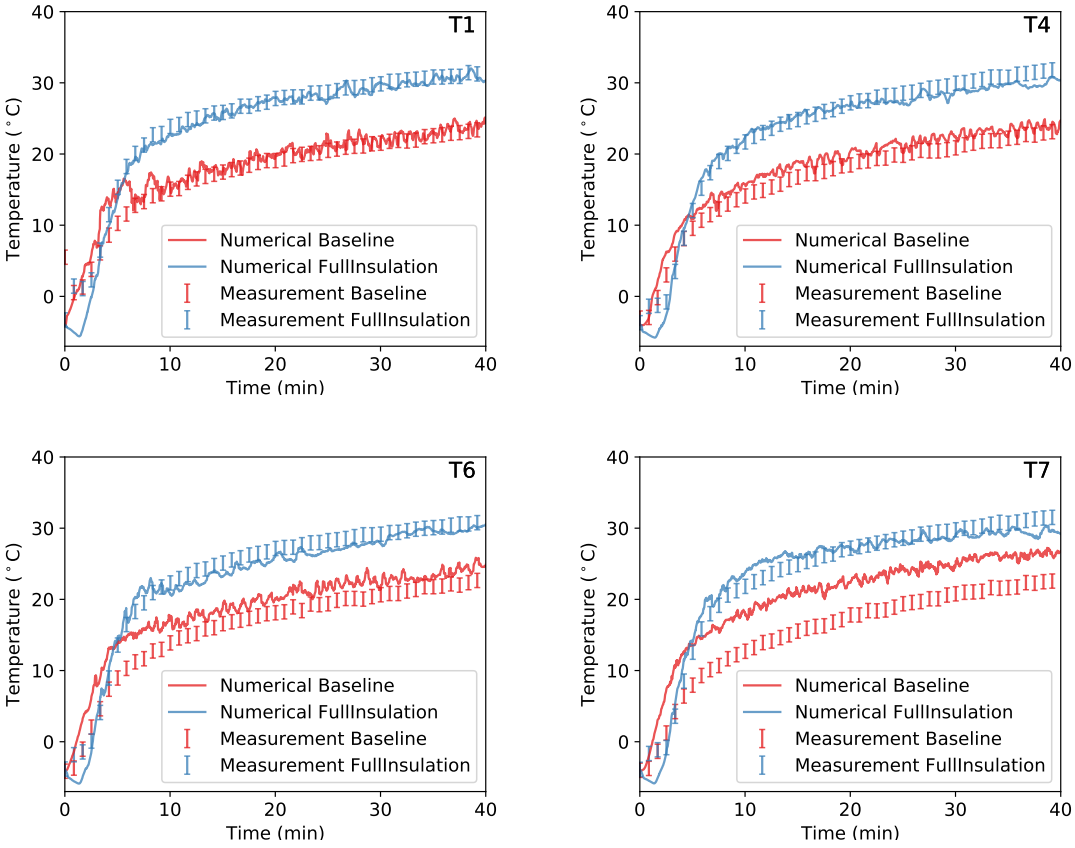

Figure 3.14: *Air temperature recorded at selected thermocouples from measurements and the numerical model.*

3.2 Reduction of ventilation load using cabin-air recirculation

3.2.1 Vehicle geometry and numerical setup

Here, an electric truck cabin was considered with a manikin at the driver's position. Similar to the previous study, all the solids inside the cabin, in direct contact with the cabin air, were accounted for, as shown in Figure 3.15a. The properties of the solids are grouped and colored based on the material properties and given in Table A.2 in Appendix A. The computational domain for the cabin air was taken from downstream of the HVAC system, from the air distribution ducts. The model had six inlets leading to a central defroster, vents, two floor inlets, and two demisters as illustrated in Figure 3.15b. Two outlets were considered, an evacuation (EVAC) and a recirculation (REC).

Since cabin-air recirculation is of interest, the CO_2 and moisture produced by the occupant in the cabin must be considered for effective operation. To track these, the air was modeled as a multi-component ideal gas with dry air and water vapor, and CO_2 was modeled as a passive scalar. This strategy was used since the concentration of CO_2 could be monitored while assuming air to be a binary mixture of dry air and vapor, and the properties of the air-vapor mixture are available in the literature. The variations in the dynamic viscosity and specific heat of dry air were considered using Sutherland's law. In contrast, for vapor, the dynamic viscosity and specific heat were set to 8.89×10^{-6} Pa-s, and 1868 kJ/kg-K, respectively [103]. The mixture properties were defined based on the mass-weighted average of the two species. The Schmidt number (Sc) and Lewis number (Le) determined the air-vapor mixture diffusivity and thermal conductivity and were computed to be 0.61 and 0.85, respectively [103, 104]. The Schmidt number for CO_2 was set to 1.14 [105]. Similar to the previous study, the realizable $k-\epsilon$ (URANS) turbulence model was used, with gravity to capture buoyancy effects during heating, and no solar radiation.

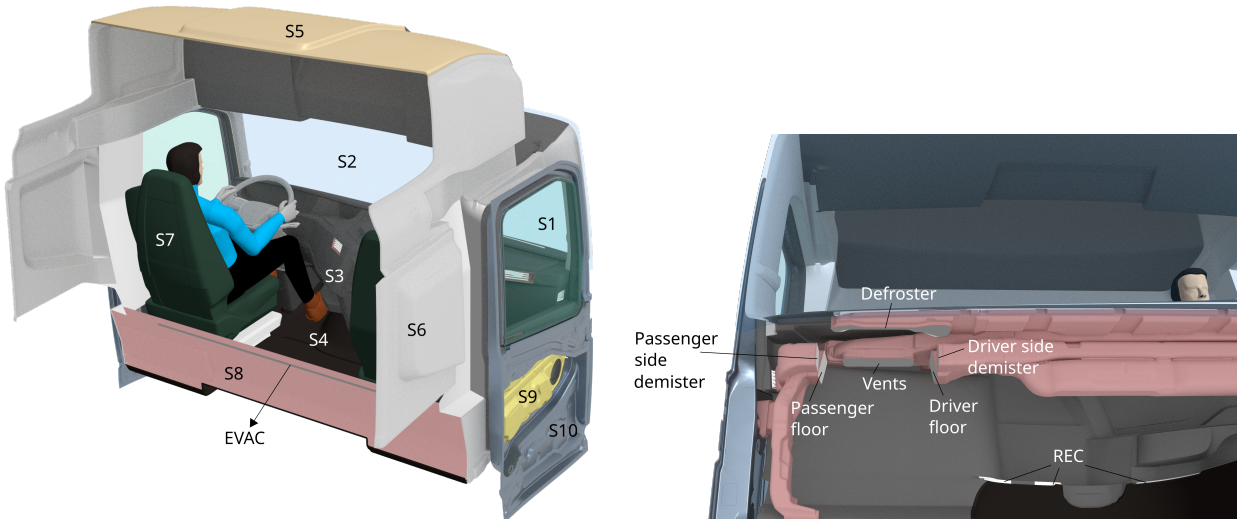

(a) *(b)*

Figure 3.15: *(a) Truck cabin with all the interior solids (S1-S10) colored based on the corresponding material property from Table A.2, along with the evacuation outlet (EVAC); (b) Inlets in the cabin and the recirculation outlet (REC).*

To model the heat transfer from the cabin air to the ambient, the inner solid surfaces were set up with CHT interfaces, while the outer solid surfaces employed a convective boundary condition, which included a heat transfer coefficient (h_{ext}), ambient temperature (T_∞) and thermal resistance (R_{th}) between the cabin solid and external wall of the truck, as shown in Figure 3.16a. The heat transfer coefficient (h_{ext}) is a function of Reynold's number (Re) and Prandtl number (Pr) when the process is forced convection-dominant. This was also seen in the previous study with the passenger car, where the heat transfer coefficient on a surface was approximately constant for a given vehicle velocity. To reduce computational demands of the CFD simulation, the h_{ext} from external flow simulations was imposed on the outer boundaries of the cabin solids, for selected velocities as shown in Figure 3.16b. More details of the simulations are provided in Appendix A.2 of Paper D.

At standstill conditions, where the heat transfer is in the natural convection regime, the heat transfer coefficient is a function of the difference between the wall and ambient temperatures [103, 106]. Hence, an empirical Nusselt number (Nu) correlation for natural convection of a vertical plate was employed as a function on the outer walls of the front and side windows.

$$\mathrm{Nu} = 0.59(\mathrm{Gr}_L \cdot \mathrm{Pr})^{1/4} = \frac{h_{ext} L}{\lambda} \tag{3.1}$$

A value of 4.65 W/m^{2}K was used on the other outer walls based on previous works [102, 107, 108] at standstill conditions. The same value was used on the outer surfaces of the dashboard and the ducts under all vehicle speeds. The R_{th} was estimated through steady-state Fourier's law of heat conduction, and given in Table A.3.

A simplified fogging model was considered using the fluid-film multiphase model [99], where the film is composed of water. The film was set up as a shell at the interfaces between the windows (S1 and S2 in Figure 3.15) and the cabin air. Table 3.3 displays the material properties of water condensed at the interface [103]. The phase change process involving evaporation and

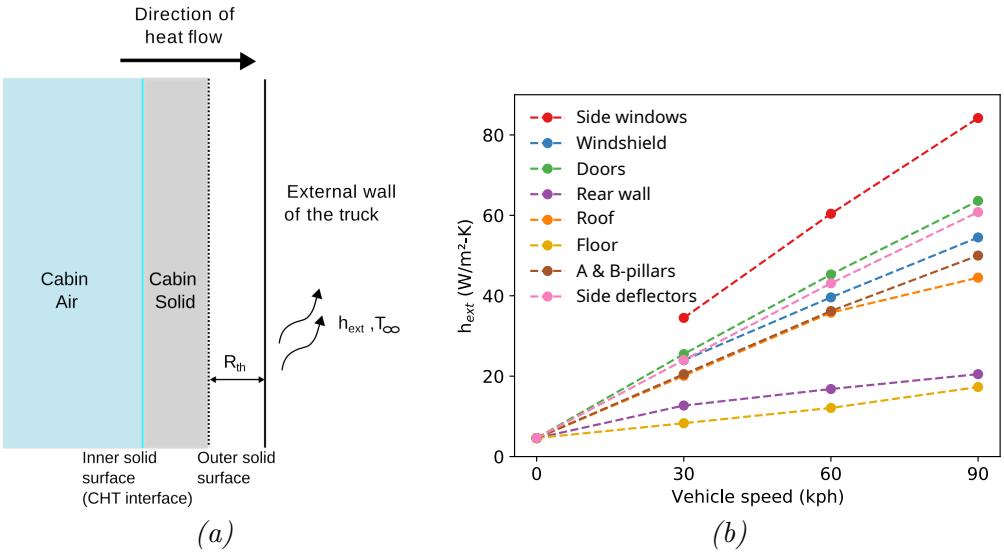

Figure 3.16: *(a) Schematic of the boundary conditions on the cabin solids; (b) Variation in the heat transfer coefficient on the external vehicle surface with vehicle speed.*

Property	Value
Density (kg/m^3)	998
Specific heat (J/kgK)	4180
Thermal conductivity (W/mK)	0.57
Latent heat (MJ/kg)	2.5

Table 3.3: *Material property of water in the fluid-film model [103]*

condensation of water is governed by the concentration and the saturation pressure (P_{sat}) of vapor in air at a given location. The saturation pressure of vapor represents the maximum partial pressure of vapor in a dry air-vapor mixture for a given temperature. In this work, the Antoine formulation was adopted [99],

$$\frac{P_{sat}(T)}{P_{ref}} = \exp\left(11.949 - \frac{3978.205}{T - 39.801}\right) \tag{3.2}$$

where P_{ref} is the reference pressure (1 bar), and T, its temperature in Kelvin.

Since the film model was used to detect the occurrence of fogging, the influence of surface tension was neglected to simplify the physics. The effect of the water adhesion to the surface was modeled by assuming a very high dynamic viscosity for water. This allowed the condensed water to stick to the surface, mimicking the effect that surface tension would otherwise have induced. This approach is valid for the current investigation since the proposed recirculation strategy should not fog the windows.

Co-simulation methodology with a human thermoregulation model

The manikin used in this work was simulated based on the joint system thermoregulation model, JOS-3 [109]. JOS-3 consists of 83 nodes where the manikin is divided into 17 segments. Each segment includes an artery, a vein, a core node, and a skin node. The limbs contain superficial vein nodes. The head and the pelvis include additional layers in muscle and fat nodes. JOS-3 models the heat loss to the ambient as sensible heat losses consisting of convective and radiative heat transfer, and latent heat loss at the skin and through respiration.

The central idea was to employ the computed total heat loss of each segment from CFD to model sensible heat loss from the manikin. The heat transfer coefficient computed based on the flow field, and the relative humidity of air were used to compute the amount of sweating through each segment. The detailed implementation is presented in section 2.2 of Paper D.

Control strategy

Two controllers were modeled, one to heat the cabin and the other to recirculate air, and were evaluated after every execution of the JOS-3 model.

Cabin heating

The cabin heater was modeled with a proportional-integral (PI) controller targeting the HVAC inlet and the mean temperature of the cabin. The inlet mode of the PI controller operated with a setpoint for inlet temperature. This was defined as a function of the ambient temperature

(T_∞), as $40 - T_\infty$ [°C]. The controller operated in this mode until the mean cabin temperature reached 20°C. Beyond this state, the controller switched to the cabin-temperature mode, with the setpoint for the mean temperature at 22°C. Thus, the heater rate at each step k is computed as,

$$Q_{heater}|_k = k_p e_q|_k + \sum_{k=0}^{N} k_i e_q|_k dt_{co} \tag{3.3}$$

where e_q is the instantaneous error, Q_{heater} is the heating load, k_p and k_i are the gains of the controller. The value for k_p was taken as -1 and k_i took the values -5 in the inlet temperature mode, and -0.5 in the cabin temperature mode. When the modes switch, the integral state of the controller was recomputed to provide a smooth transition. Based on the output of the PI controller, the inlet temperature to the cabin was set as,

$$T_{in}|_k = T_{bo}|_k + \frac{Q_{heater}|_k}{\dot{m} c_p} \tag{3.4}$$

where T_{bo} is the temperature of the air upstream of the heater, $\dot{m}$ is the mass flow rate of air into the cabin and c_p is the specific heat of air. The temperature of air upstream of the heater was defined as,

$$T_{bo,k} = \gamma|_k T_{REC}|_k + (1 - \gamma|_k) T_\infty \tag{3.5}$$

where γ represents the return-air ratio and T_{REC} is the mass flow averaged temperature obtained at the outlet of the boundary, REC. To prevent overshoot, the maximum temperature at the inlet was limited to the setpoint temperature when operating in the cabin-temperature mode.

Recirculation strategy

The recirculation or return-air ratio (RAR) strategy employed two controllers, one for CO_2 (α) and the other for vapor mass fraction (x_ω), and chose the most critical strategy.

The concentration of CO_2 at the inlet of the ducts with RAR was defined similarly to eqn. 3.5 as,

$$\alpha_{bo}|_k = \gamma|_k \alpha_{REC}|_k + (1 - \gamma|_k) \alpha_\infty \tag{3.6}$$

where α_{REC} is the mass flow averaged value entering the REC boundary, and α_∞ is the ambient condition. The equation for x_ω was defined similarly.

The setpoint for CO_2 in this work was considered to be a mean concentration of 1000 ppm to maintain a safe operating environment in the vehicle based on previous works [64, 110]. The output of the controller yielded the RAR γ_α, and was formulated analogous to eqn. 3.3. The gains for the controller were taken from the work of Wei et al. [64] as -0.03 for k_p and -0.0003 for k_i.

The criterion for humidity must be formulated such that the air entering the cabin does not fog the windshield and the side windows. So, if the dew-point temperature of the air from the HVAC is lower than the minimum window temperature ($T_{g,min}$), fogging due to HVAC flow can be prevented. Thus, the setpoint for vapor mass fraction was defined with a safety margin of 1°C from $T_{g,min}$. The vapor mass fraction was defined as,

$$x_\omega(T, \phi) = \frac{\omega(T, \phi)}{1 + \omega(T, \phi)} \tag{3.7}$$

where ω is the specific humidity of vapor and was defined as,

$$\omega(T, \phi) = 0.622 \frac{\phi P_{sat}(T)}{P - \phi P_{sat}(T)} \tag{3.8}$$

P_{sat} is the saturation pressure obtained from the Antoine equation (eqn. 3.2), ϕ is the relative humidity and P is the reference pressure. The setpoint was redefined at each step as $x_\omega(T_{g,min}|_k - 1, 100\%)$.

The gains were set based on the ambient temperature, and are defined in the Appendix C. The rest of the controller was defined similarly to eqn. 3.3 and the output of this controller yielded γ_{x_ω}.

The minimum of (γ_α, γ_{x_ω}) was considered as the final recirculation ratio (γ) for the subsequent step. This approach is equivalent to the strategy proposed in [68], however, the usage of the PI controller provides feedback control and aids in maintaining the setpoint despite local flow variations. The output of the re-circulation controller was saturated between [0, 0.95].

Boundary conditions

Several boundary conditions needed to be defined for the co-simulation. For clarity, these conditions are grouped into CFD-based, thermoregulation-based, and case-based conditions. Each category includes some constants and a few scenario-dependent variables.

CFD-based conditions

- Mass flow rate into the cabin from the blower: 0.083 kg/s
    1. Defroster: 0.0166 kg/s
    2. Vents: 0.0099 kg/s
    3. Driver-side demister: 0.0074 kg/s
    4. Passenger-side demister: 0.0074 kg/s
    5. Driver floor: 0.01826 kg/s
    6. Passenger floor: 0.0232 kg/s
- Mass flow rate from the human nostrils: 9 l/min [110]
- Ambient CO_2 concentration: 420 ppm
- Human breath CO_2 concentration: 40000 ppm
- Relative humidity of human breath: 90% [111]. The vapor mass concentration was computed based on eqn. 3.7 and eqn. 3.8 at the core temperature of the driver's head during runtime.

The air temperature, mass fractions of vapor and dry air, and the CO_2 concentrations were defined as functions at the inlet boundaries based on eqn. 3.4, and eqn. 3.6 and corresponding variations for vapor and air mass fraction. The cabin was initialized to the same temperature,

Ambient Temperature (°C)	Clothing resistance (clo)				
	Head	Torso	Hand	Leg	Feet
0	0	0.9	0.1	0.9	0.1
-10	0	1.3	0.15	1.3	0.15
-20	0	1.5	0.2	1.5	0.2

Table 3.4: *Clothing resistance on JOS-3 depending on the ambient temperature.*

vapor-air, and CO_2 concentration as the ambient. The boundary conditions for driving speed, ambient temperature, and relative humidity are explained later in the subsection, case-based conditions.

Thermoregulation-based conditions

- Initial soak time: 5 min. This was imposed to get a representative initial skin temperature for the driver under a certain ambient condition.
- Clothing resistance: The total clothing resistance on the driver was considered based on the ambient temperatures according to the recommendations from Rintamaki et al. [112] for a low-moderate activity level. This was divided into five and applied to individual segments in JOS-3 as shown in Table 3.4.
- Physical activity ratio: 1.6. The ratio of total energy production to the metabolic rate of the driver.

Case-based conditions and sensitivity analyses

Each co-simulation was defined using three parameters: the vehicle speed, the temperature, and the relative humidity of ambient air. These parameters were chosen as they had the largest influence on the choice of recirculation strategy, energy consumption, and thermal comfort. To understand their sensitivity, a reference case at 90 km/h, -10°C, and 70% RH was considered. The effect of vehicle speed is discussed in Paper D. Two ambient temperatures -20°C, and 0°C, at 70% RH, and two relative humidities, 50%, and 90%, at -10°C and -20°C are analyzed. To quantify the reduction in energy expenditure using recirculation, the cases were also investigated without recirculation, i.e. $\gamma = 0$.

A numerical sensitivity study for the current model was systematically performed and included mesh and time step studies. The results are presented in detail in Paper D. The resulting configuration with about 33 million polyhedral cells and a timestep of 0.2 s was found to be sufficient. The approach of freezing the flow solver was not used in the truck model since the outlet boundary condition was altered with recirculation.

3.2.2 CFD validation with experimental data

The results from a climatic chamber test performed on the truck at stand-still conditions without a manikin were used to validate the accuracy of the CFD model. The truck cabin was equipped

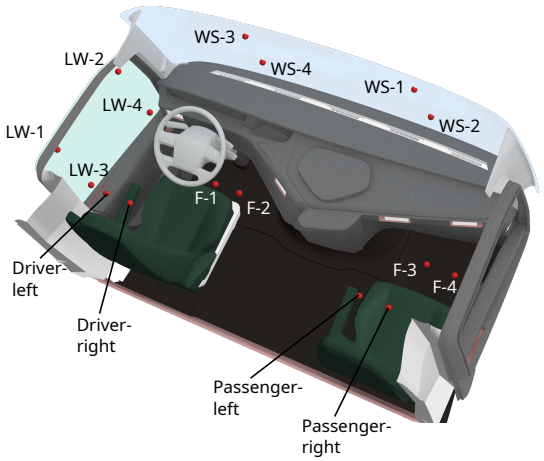

Figure 3.17: *Positioning of the thermocouples during the test in the climatic chamber.*

with several K-type thermocouples as shown in Figure 3.17. The thermocouples, Driver-left, Driver-right, Passenger-left, and Passenger-Right measure the air temperatures at the head level while the others measure the surface temperatures. During the test, the cabin was soaked to an ambient temperature of 0°C (T_∞) and was heated for two hours with the Auto-HVAC setting and a target of 22°C. The temperatures at the end of the test were monitored for about 10 minutes to ensure they had reached steady values. For effective comparison with the experimental data, a steady-state numerical simulation was performed with the resulting mesh from the mesh study (without the manikin), and the results are shown in Figure 3.18. It can be seen that they agree well, with several estimations from the numerical simulation within the probe's accuracy of ± 0.5°C. Although small deviations are seen for certain probes, the model was considered validated since the mean error was 2.5% and the maximum error was about 6.5% for the considered case.

3.2.3 Heating performance with cabin air recirculation

The results discussed in this subsection correspond to the reference case, at -10°C, 70% RH, and 90 km/h driving speed. The main energy source to heat the cabin is the heater modeled at the inlet and therefore, a strong convection effect is seen in these regions. This is visualized in Figure 3.19, where the temperature along the driver's median plane and front window, along with the boundary heat flux on the driver are displayed at selected times during the heat-up. At 10 s, a plume of warm air rises from the driver, denoting natural convection owing to the high surface temperature. This disappears when the inlet flow enters the cabin as seen in the subsequent images. The local variations in the temperature distribution along the plane can be attributed to the convective jets from the inlet flow, in addition to the respiration from the manikin. Due to the large temperature difference between the driver and the cabin air, a large heat flux is seen at the beginning, and it gradually reduces as the cabin warms up. The flow from the central defroster warms the front window. However, due to the high driving speed of 90 km/h, the windshield remains cold, away from the region where the defroster flow is incident.

Figure 3.20 presets the vapor mass fraction at the inlet, and RAR for the case with adaptive control on the reference case. It can be seen that the controller operates as expected by varying the RAR to achieve the required setpoint. The dotted and dashed lines in the figure represent

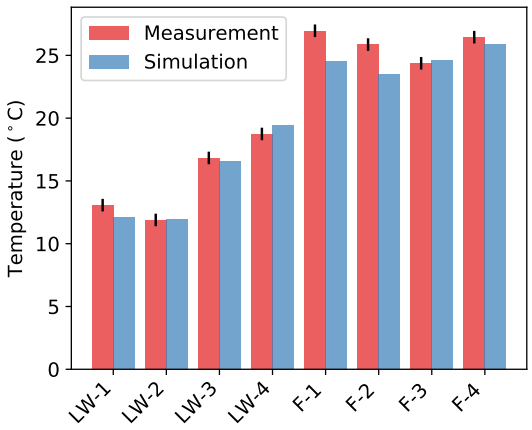

(a)

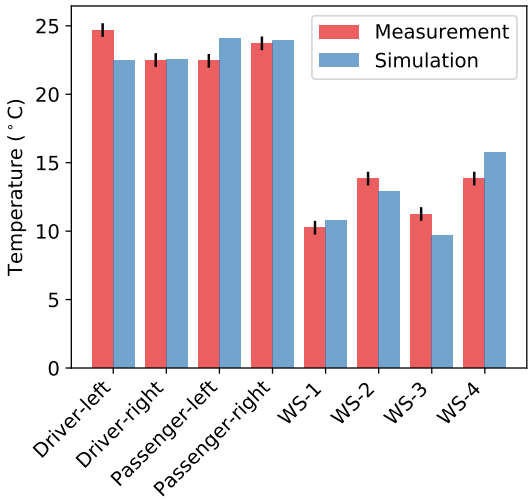

(b)

Figure 3.18: *Comparison of the thermocouples' temperatures from the numerical simulation and experiment. The uncertainty of the experiments was considered to be the probe's accuracy. (a) Left window and floor thermocouples; (b) Head-level air temperatures and front windshield thermocouples.*

the variation in the vapor mass fractions that cause fogging and the corresponding setpoint from the controller, which takes the minimum temperature of the interface into account, respectively. The control has little over-shoot, demonstrating that the operating conditions at the inlet never exceed the saturated state on the front window. The resulting RAR is about 78% at the end of 30 min and this is expected to increase with rising minimum window temperatures. The mean cabin CO_2 concentration with this RAR was 775 ppm, which indicates that the humidity is more critical than CO_2 for RAR control of the reference case. With the RAR strategy, the total energy consumption was approximately 6.3 MJ over the 30 min of the simulation, which is about 29.3% lower than the same scenario with no recirculation. The average temperature of the cabin with the RAR is about 0.5 to 1°C lower than the case without recirculation, as displayed in Figure 3.21a. This is because the heater rate drops due to the hot air entering the recirculation

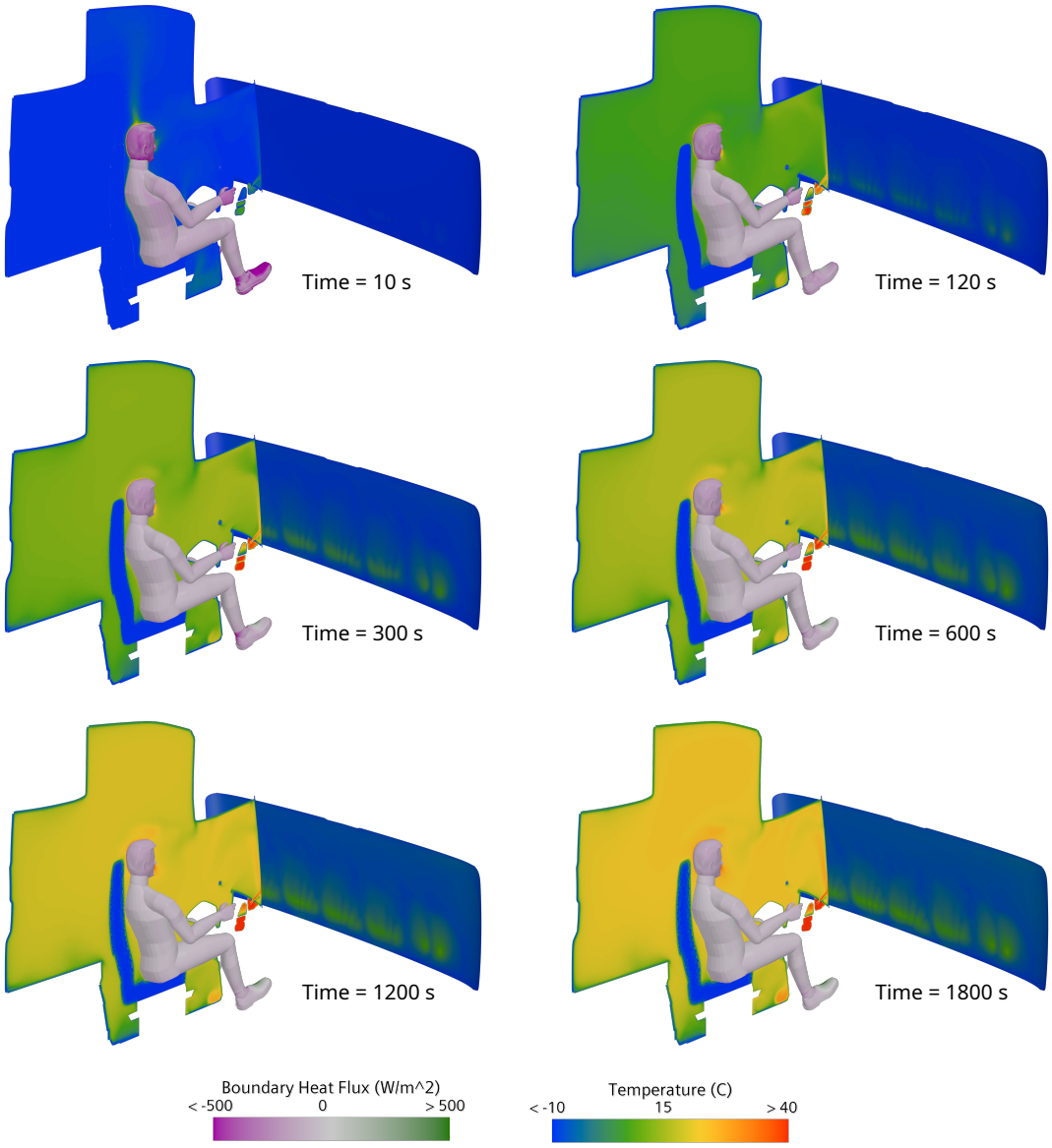

Figure 3.19: *Temperature distribution along the driver's median plane and front window along with the boundary heat flux on the driver at several time instances during the heat-up at -10°C, 70% RH, and 90 km/h.*

outlets under the dash panels. A large portion of the air from the floor inlets moves towards the REC ducts upon striking the foot of the driver, and/or the floor of the truck. This means that the hot air from the inlets does not mix with the cabin and less energy is imparted for cabin heating. However, this did not severely affect the overall thermal sensation and comfort indices of the driver, obtained based on the UCB-Zhang thermal comfort scale [113], as shown in Figure 3.21b.

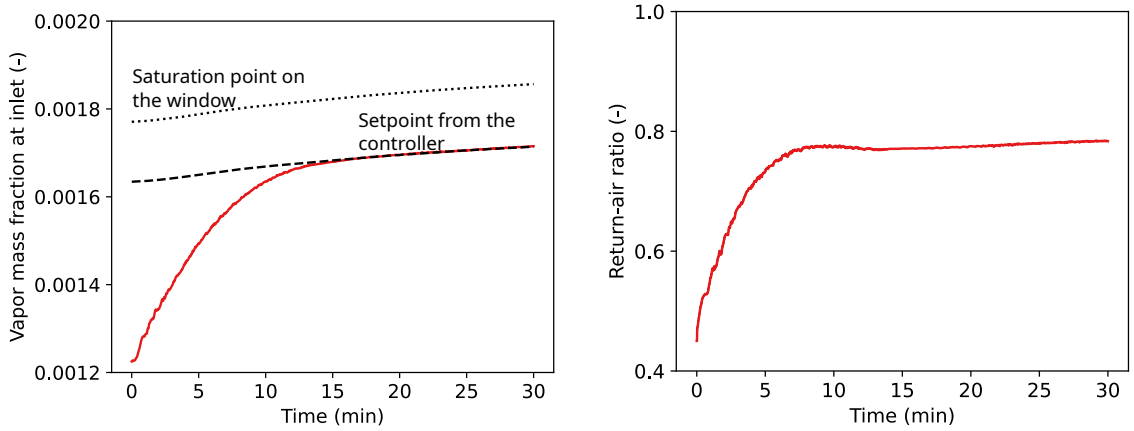

(a) *(b)*

Figure 3.20: *Results of the RAR controller on the reference simulation, -10°C, 70% RH and 90 km/h: (a) Vapor mass fraction at the inlet; (b) Return-air ratio.*

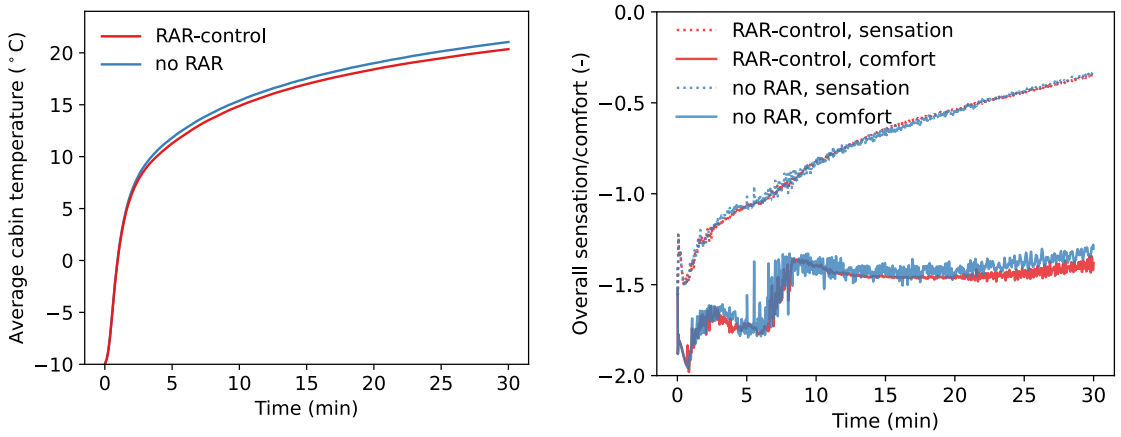

(a) *(b)*

Figure 3.21: *Results from the reference simulation with and without recirculation: (a) Average cabin temperature; (b) Overall sensation and comfort.*

Parametric analysis

The effects of variation in driving speed, ambient temperature, and relative humidity from the reference case are individually analyzed in Paper D, and only the combined analysis is discussed here. The results from the parametric analyses considering the variation in ambient temperature and relative humidity at 90 km/h are plotted together in Figure 3.22. It can be seen in Figure 3.22a that the fresh-air flow rate ($(1-\gamma)\dot{m}_{in}$) into the cabin decreases with Δx_ω, which represents the difference between the setpoint vapor mass fraction computed at $T_{g,min}-1$ (which varies during heat up) and the ambient vapor mass fraction, i.e. $\Delta x_\omega = x_\omega(T_{g,min}-1) - x_{\omega,\infty}$. In the plot, each cluster of symbols represents the results from one scenario after either of the setpoints is achieved. A clear trend is observed, meaning that irrespective of the ambient temperature and relative humidity, the Δx_ω determines the amount of fresh air required. This trend should be valid at any driving speed since the determining factor for fogging is the temperature of the surface and the humidity of the air adjacent to it. For each scenario, the

amount of fresh air required decreases since the windows heat up, thus increasing the Δx_ω. The maximum RAR of approximately 86.3% corresponding to a fresh air flow rate of 10 g/s maintains the mean cabin CO_2 concentration at 1000 ppm as shown in previous literature [64, 110]. The steady-state solution from the 0D cabin (derived in Appendix B, eqn. B.6) is plotted with an uncertainty band. As seen, it is in excellent correlation with the results from CFD. The uncertainty stems from the amount of sweating from the manikin, varying from 18 to 25 g/h, depending on the clothing resistance (Table 3.4) employed for a given scenario. This agrees well with the observations in previous studies [67, 114]. While the correlation is good, the small deviations between the solutions from the two models can be attributed to the local vapor mass fraction and the CO_2 concentrations at the REC boundaries in CFD, which can not be captured in the 0D model. Additionally, the presence of an open REC outlet changes the flow behavior around the dashboard and floor as described earlier.

In Figure 3.22b, the net energy savings are plotted as a function of mean RAR over the last 5 min of the scenario. They increase linearly with RAR until the threshold for CO_2 is met at 86.3% RAR. At this point, the trend deviates between different ambient temperatures. This can be explained by rearranging eqn. 3.4 and eqn. 3.5 as,

$$\begin{aligned} Q_{heater,k} = \dot{m}_{in} c_p \big[&\left(T_{in,k}|_{(T_{cab},T_\infty)} - T_\infty\right) \\ &-\gamma|_{\Delta x_\omega,k} \left(T_{REC,k} - T_\infty\right)\big] \end{aligned} \tag{3.9}$$

The setpoint for the inlet temperature is a function of the mean cabin and ambient temperatures. As explained from Figure 3.22a, the RAR is dependent on the Δx_ω. The net energy savings relative to no recirculation can be defined from eqn. 3.9 as,

$$\Delta Q_{heater}\% = \frac{\sum_k \gamma|_{\Delta x_\omega,k}(T_{REC,k} - T_\infty)}{\sum_k T_{in,k}|_{(T_{cab},T_\infty)} - T_\infty} \times 100 \tag{3.10}$$

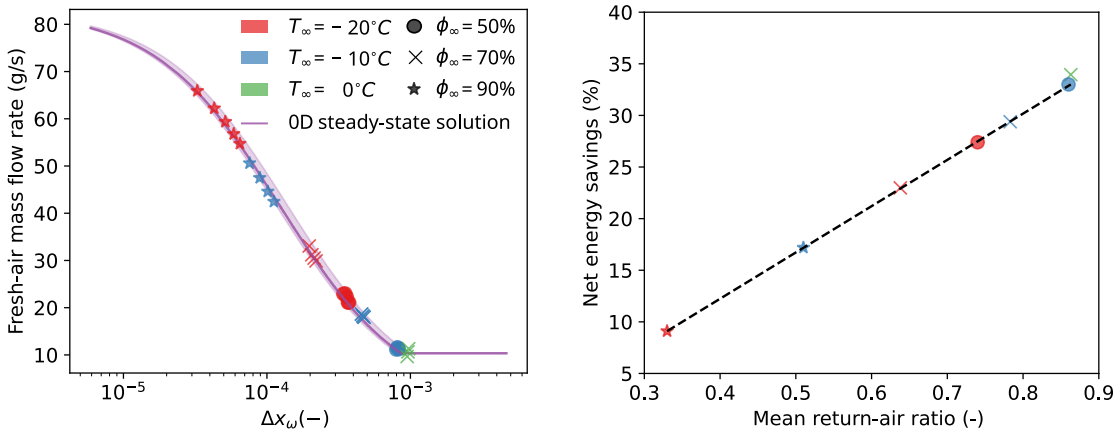

(a) *(b)*

Figure 3.22: *Combined analysis based on the sensitivity studies of ambient temperature and relative humidity at 90 km/h: (a) Variation of fresh-air flow rate into the cabin versus the difference between setpoint and ambient vapor mass fractions at the inlet (Δx_ω); (b) Variation of net energy savings vs return-air ratio*

The expression describes the linear dependency between energy savings and RAR. This also explains the lower energy savings at lower ambient temperatures. The energy saving at 0°C ambient temperature and 70% RH is marginally higher than -10°C and 50% RH, even though they operate at 86% RAR, due to the inherently lower energy requirement (smaller denominator in eqn. 3.10) to heat the cabin when operating at 0°C. It must be mentioned that the net energy savings for the investigated scenario are typically lower since T_{REC} and γ increase during the heat-up phase. The instantaneous energy saving was more than 41% for the reference case at the end of 30 min.

3.3 Combined effects on the truck cabin

Both strategies were studied together on the truck model and the results are discussed in this section. First, the fully insulated cabin is compared with the baseline cabin, and then the recirculation control is included in the fully insulated model. The co-simulation procedure with the JOS3 and the cabin heater was employed to target a mean cabin temperature of 22°C and studied on the reference case at 90 km/h, -10°C, and 70% RH.

Analogous to the passenger car cabin, the truck model was modified to include thermal resistances on various solids to resemble the fully insulated setup. The configuration with resistance 0.82 m^2K/W was simulated. Figure 3.23a compares the mean cabin temperature of the baseline and fully insulated cabins. As seen in Section 3.1, the rate of cabin heating is higher for the fully insulated cabin. The cabin reaches the target setpoint temperature in about 10 minutes with the fully insulated configuration while the baseline does not reach the setpoint even in 30 minutes. The higher air and surface temperatures of the fully insulated cabin improve the overall sensation to more neutral conditions (≈ 0 [113]) as compared to the baseline where the conditions are perceived as cold, as shown in Figure 3.23b.

One of the consequences of cabin insulation as shown in Figure 3.24 is that the inlet temperature required to maintain the cabin at the setpoint is reduced since the heat losses to the cabin solids

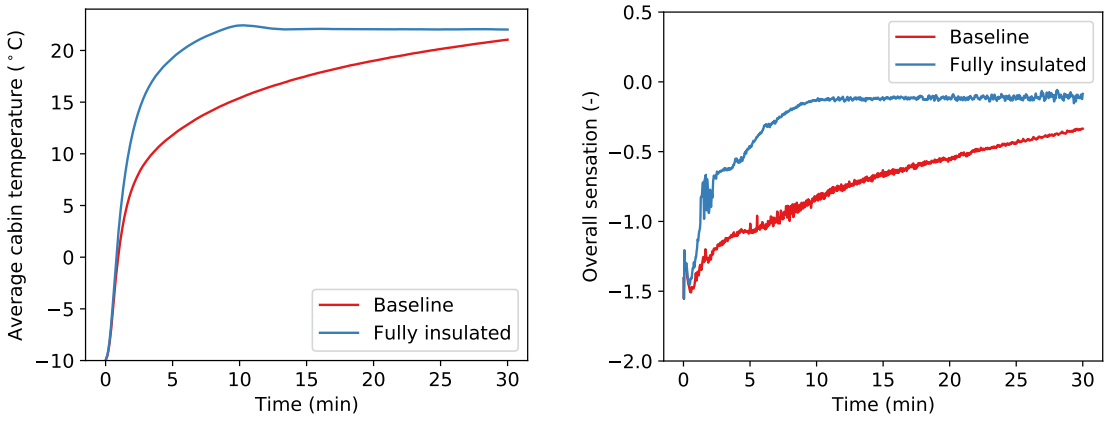

(a) (b)

Figure 3.23: *Comparison between baseline and fully insulated configurations: (a) Average cabin temperature; (b) Overall sensation.*

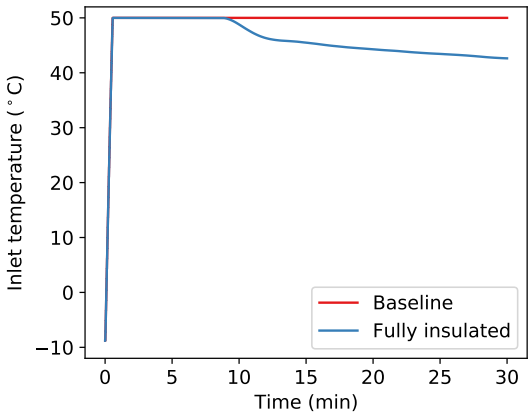

Figure 3.24: *Cabin inlet temperature comparison between baseline and fully insulated cabins.*

are lower. As the cabin reaches the setpoint temperature, the inlet temperature is reduced. This means the energy required by the cabin heater is also reduced, and for the considered scenario over 30 minutes, it accounts for about 6% reduction in energy expenditure.

Next, the fully insulated cabin with cabin air recirculation is discussed. The vapor mass fraction at the inlet and the employed recirculation ratios are compared between the baseline and fully insulated configurations in Figure 3.25. Under humidity-critical conditions, the recirculation controller determined the setpoint based on the minimum window temperature. With the fully insulated cabin, the minimum temperature on the window increases at a faster rate than the baseline cabin, resulting in a more aggressive recirculation strategy. However, since the heater rate drops with the fully insulated configuration at 10 min, the mean and minimum temperatures on the window plateau around -4.7°C and -9.3°C, respectively while the same for the baseline configuration continue to rise.

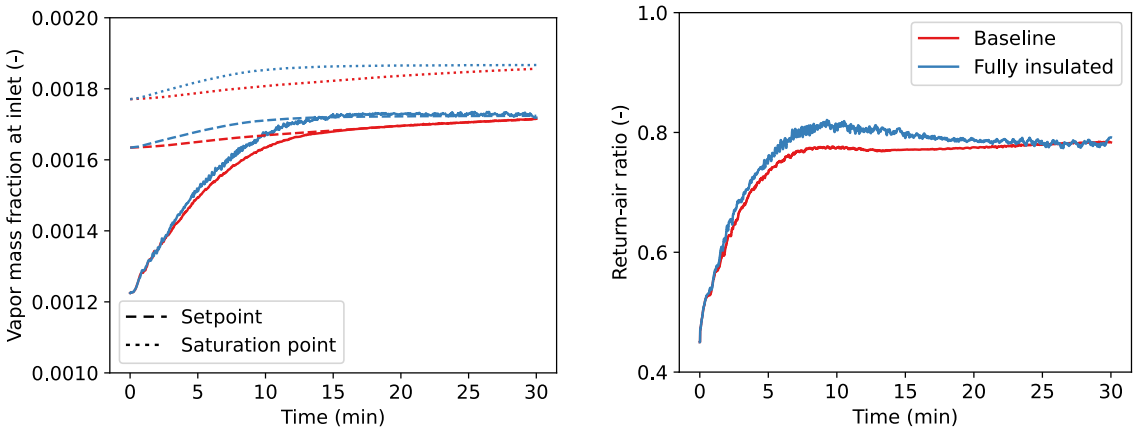

(a) *(b)*

Figure 3.25: *Results from the RAR control of the reference scenario for the baseline and fully insulated cabins: (a) Vapor mass fraction at the inlet; (b) Return-air ratio.*

Configuration	Energy expenditure (MJ)	Energy Savings (%)	Mean overall sensation (−)
Baseline	8.927	–	-0.73
Baseline w/ RAR	6.311	29.3	-0.731
Fully insulated	8.377	6.1	-0.251
Fully insulated w/ RAR	5.199	41.7	-0.253

Table 3.5: *A summary comparing the energy expenditure, energy savings and mean overall sensation for the baseline and fully insulated cabins with/without RAR control.*

The energy expenditure of the configurations, the energy savings relative to the baseline setup, and the mean overall thermal sensation are presented in Table 3.5. It can be seen that the baseline cabin with recirculation control provides better energy savings while the fully insulated configuration provides better overall sensation for the occupant. The fully insulated configuration with the recirculation has the best heating performance and thermal sensation metrics. The fully insulated configuration with RAR control has greater savings (41.7%) than the isolated configurations combined. The fully insulated cabin reaches the temperature setpoint faster than the baseline cabin and this enables the heater to employ warmer recirculated air. Thus, based on eqn. 3.10, the main reasons for the greater energy savings are due to higher RAR and recirculated air temperature, coupled with lower inlet temperature requirements with the fully insulated configuration as compared to the baseline cabin.

4

Thermal encapsulation for battery pack climatization

This chapter focuses on the climatization of large battery packs using thermal encapsulation as a means of passive battery thermal management to reduce heat loss during periods of cool-down. First, the modeling framework and the battery pack model validation are presented. Then, the effects of battery pack thermal encapsulation are discussed.

Two battery pack configurations were studied. The first type was used in Papers A and B, where only the battery pack modeling and encapsulation were of primary interest, and the second type was used in Paper E, where the complete vehicle was considered. Only the latter setup is discussed in the chapter. The battery pack was modeled in the commercial simulation platform, GT-SUITE.

4.1 Modeling framework

4.1.1 Battery pack modeling

The battery pack in consideration had Li-ion cells arranged in several stacks or trays. Each tray included an aluminium cooling plate, battery modules, and a thermal interface material between the modules and the cooling plate as shown in Figure 4.1. Each module had several prismatic NMC-type Li-ion cells.

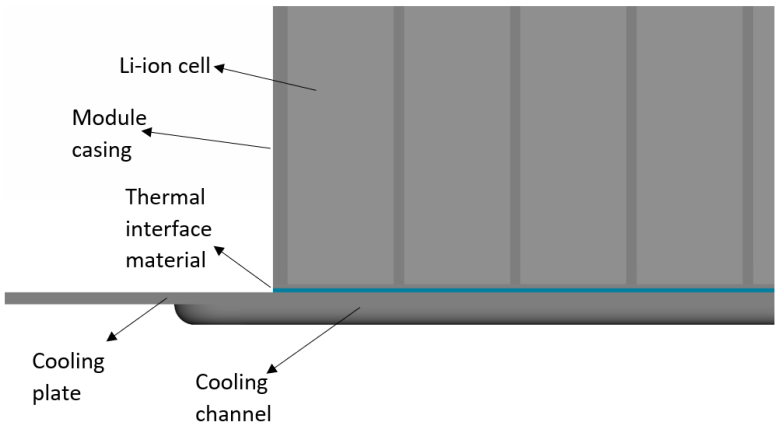

Figure 4.1: *Cross-sectional view of the battery module assembly.*

Property/Material	Aluminium	Stainless steel	Coolant	Li-ion cells
Density (kg/m^3)	2702	7860	1057	2846
Thermal conductivity (W/m-K)	160	15	0.44	12.3
Specific heat (J/kg-K)	883	460	3484	888
Dynamic viscosity (Pa-s)	-	-	0.0027	-

Table 4.1: *Thermal properties of the materials in the battery pack.*

The cooling plates consisted of several channels for the coolant to flow through, to condition the cells. The coolant used was a 40-60 mixture of glycol water. The conservation equations in 1D formulation for coolant flow through the channels were solved numerically using an implicit solver to compute the fluid and heat flow in the model [115]. These quantities were solved only in the direction of fluid flow. To compute the conjugate heat transfer between the fluid and solids, the heat transfer coefficient (h) must be estimated. This closure problem was solved by using empirical heat transfer correlations for the Nusselt number, $Nu_D = hD/\lambda$, where D is the channel diameter and λ is the thermal conductivity.

The coolant flow through the channels of the battery pack was predominantly laminar. So, a constant Nusselt number of 3.66 was taken under constant wall temperature consideration [103], which was used to compute the heat transfer coefficient. For the other pipes, the heat transfer coefficient was obtained through the Colburn analogy [116]. Thus, the heat transfer between the coolant and the cooling channels was computed.

The battery pack was discretized at the module level. Each battery module included battery cells enclosed by a module casing. The cells in each battery module were modeled using a single thermal mass. This approximation facilitated simulations at the vehicle level with a good trade-off between accuracy and computational resources. The consequence is that all cells in the module have the same temperature. This assumption holds good when the battery operates at low C-rates (discharge or charge current normalized with capacity) and when the cell temperatures in the module are quite uniform.

The battery cells were in contact with the module casing (in stainless steel), and the heat transfer between the two was modeled through conduction. The heat resistance of the thermal interface material between the module casing and the cooling plate was calibrated based on data from a heat-up test, shown below. Finally, a stainless steel battery pack casing enclosed all the modules, and was modeled as a thermal mass. The heat transfer between the battery modules and the casing was calibrated using thermal resistance with data from a cool-down test. Table 4.1 shows the properties of the materials used in the battery pack.

A second-order (2RC) Thevenin electrical circuit model (ECM) [117] was used to describe the electrical behavior of battery cells along with Bernardi's thermal model [118] to account for heat generation. The ECM uses resistors ($R_{i,0}$) and capacitors (C_i) to estimate the output terminal voltage (V_T). The schematic of the 2RC ECM is illustrated in Figure 4.2. The terminal voltage at a given step k is computed as,

$$V_T^k = U_{oc} - I^k R_0 - \sum_i U_i^k \tag{4.1}$$

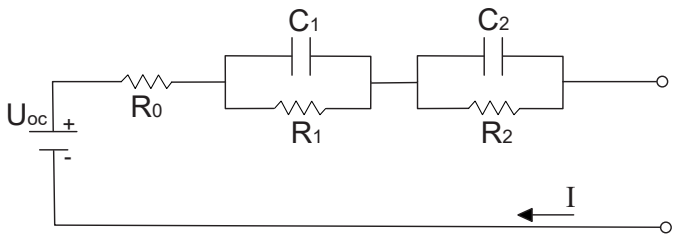

Figure 4.2: *Schematic of the second-order Thevenin electrical circuit model.*

where U_{oc} is the open-circuit voltage of the cell, i represents the RC-branch and takes values [1,2], I is the current through the cell, and

$$U_i^k = U_i^{k-1} e^{-\frac{\Delta t}{R_i C_i}} + R_i (1 - e^{-\frac{\Delta t}{R_i C_i}}) I^{k-1} \tag{4.2}$$

Look-up tables as functions of current, battery temperature, and SoC were created for the model parameters $R_{i,0}$ and C_i by using a standard hybrid pulse power characterization (HPPC) test of the battery cell. The developed model applied for cell temperatures between -20°C to 40°C across SoC in the range of 0.1 to 0.9 and at different current rates. The battery pack model was discretized at the module level and so all battery cells within the same module were assumed to have identical states.

The heat generation ($\dot{Q}$) in each module was estimated using,

$$\dot{Q} = N_{mod} \cdot I \left((U_{oc} - V_T) + T \frac{\partial U_{oc}}{\partial T} \right) \tag{4.3}$$

where N_{mod} is the number of cells in each module, and T is the module temperature.

Battery pack heat transfer

The thermal interface material present between the module casing and the cooling plate was represented using thermal resistance, and it was used to calibrate the heat transfer between the battery modules and the coolant. Similarly, the heat transfer between the battery modules and the battery casing was calibrated using thermal resistance.

The temperatures are non-dimensionalized as,

$$\theta = \frac{T - T_{ref}}{T_0 - T_{ref}} \tag{4.4}$$

where T_0 is the initial measured temperature, T_{ref} is the reference temperature for the scenario. The reference temperature was taken at the ambient temperature for the cool-down cases or such that the measured values lie between 0 and 1 for the other scenarios.

Figure 4.3a presents a comparison between the non-dimensionalized measured and simulated battery pack temperatures during a cool-down test under idle conditions. The experiment was performed in a test chamber where the ambient temperature was maintained at subzero temperatures for about 34 h and the average battery pack temperature was monitored. The results from the simulation agree with the measurements indicating that the heat loss from the battery pack to the ambient is captured very well.

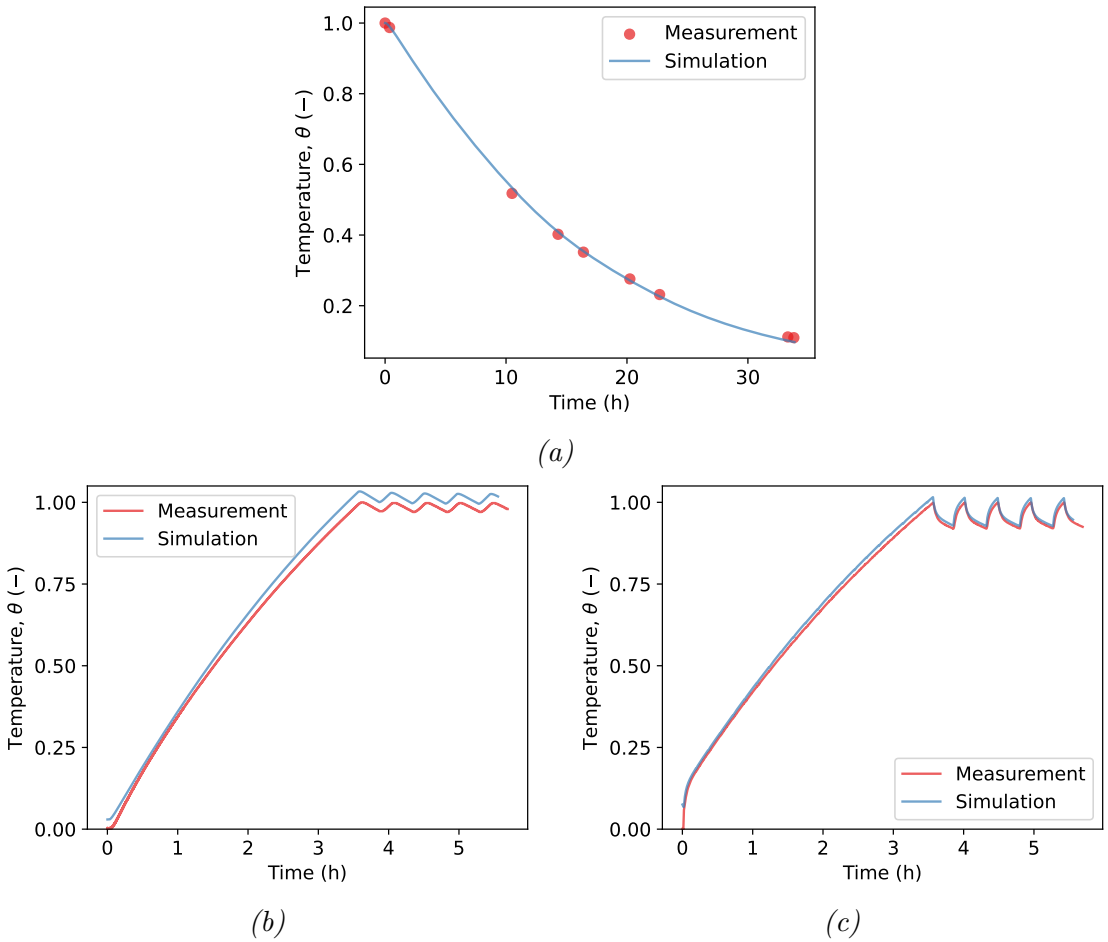

Figure 4.3: *Non dimensionalized temperature (θ) vs time comparing measurements and simulations; (a) Battery pack temperature during cool-down; (b) Battery pack temperature during heat-up; (c) Outlet coolant temperature from the battery pack during heat-up.*

Figure 4.3b and Figure 4.3c present a comparison between the measured and simulated battery pack temperatures, and coolant outlet temperatures during a heat-up test, where warm coolant flowed through the battery pack. The coolant inlet conditions, consisting of the volume flow rate and coolant temperature, were taken from the measurements. The results demonstrate the excellent agreement in the heat transfer between the modules and the coolant.

4.1.2 Battery pack model validation

Data measured from a truck during a winter expedition in Kiruna, Sweden, was used to validate the battery pack performance. Figure 4.4a and Figure 4.4b present the truck's measured speed and requested current from the pack. The battery pack was initially cold, so the battery was heated simultaneously using a heater. The initial SoC of the battery pack was 83%, and the coolant flow rate and temperature into the battery pack are presented in Figure 4.4c.

Based on these inputs, four quantities namely, average battery pack temperature, coolant outlet temperature, terminal pack voltage, and SoC were evaluated as shown in Figure 4.5. The trends

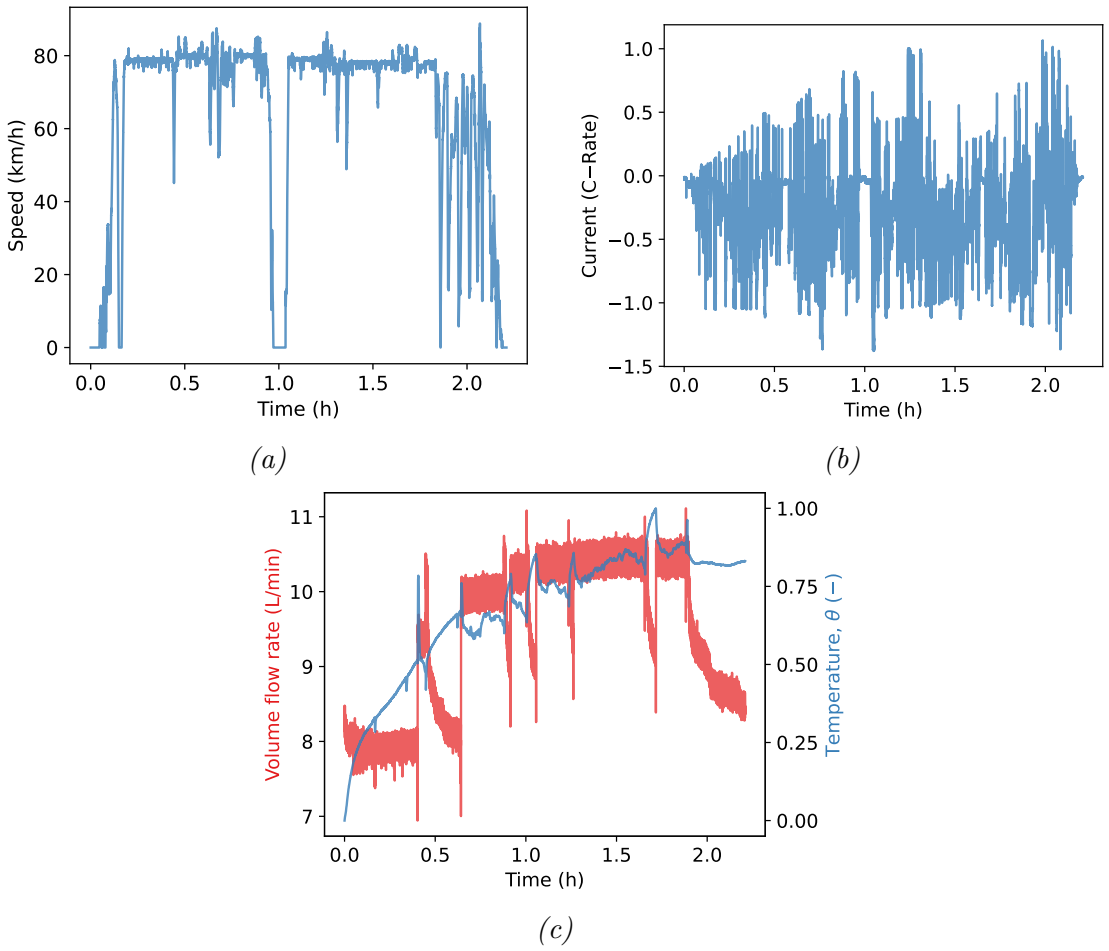

Figure 4.4: *Battery pack validation scenario: (a) Vehicle speed, (b) Current, and (c) Inlet volumetric flow rate and temperature of the coolant.*

Quantity	RMSE	Maximum error
Average battery pack temperature (°C)	0.633	1.308
Outlet coolant temperature (°C)	0.244	1.087
Normalized pack voltage (%)	1.34	6.5
SoC (%)	1.03	2.13

Table 4.2: *RMSE and maximum errors between the measured and simulated quantities for the validation scenario.*

are captured well in the simulation for all the quantities. The root mean square errors (RMSE) and the maximum error between the simulated and measured values are presented in Table 4.2. The results are in good agreement with the measurements.

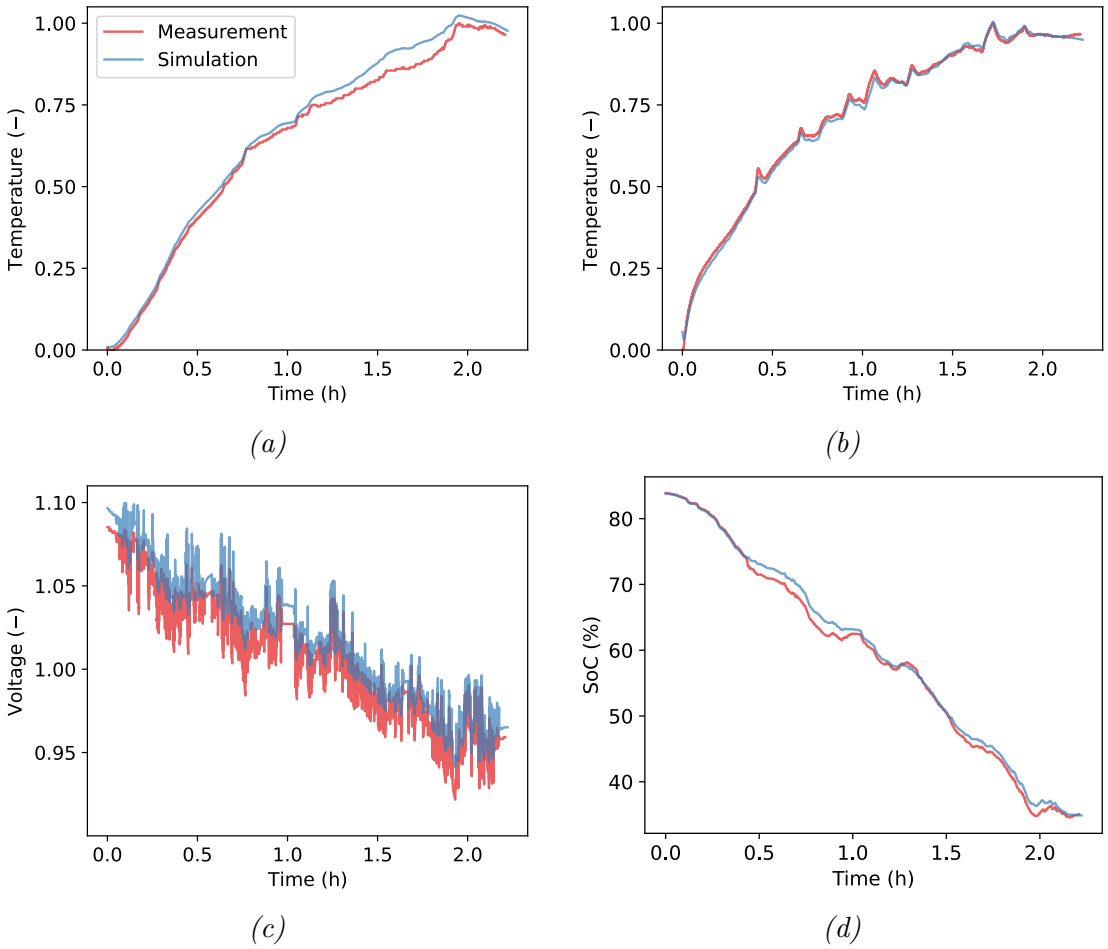

Figure 4.5: *Results for the validation scenario: (a) Average battery pack temperature, (b) Outlet coolant temperature, (c) Pack terminal voltage, and (d) Battery pack SoC.*

4.2 Effects of battery pack encapsulation

The central idea of battery pack encapsulation is that the packs are typically warm at the end of driving and by encapsulating them, the energy required to reheat them for subsequent operations after long parking periods can be reduced. This increases the driving range and also the battery life. In the study, this was achieved using thermally insulating materials as seen in Figure 4.6. Plates of insulation with a certain thickness and material properties were placed on each side of the battery pack. The thermal conduction between the battery pack casing and the thermal insulation was considered to account for heat loss.

In Paper B, the energy consumption was evaluated at selected ambient temperatures from 25°C to -25°C under parking-driving scenarios, where the pack was initialized to 25°C, and allowed to cool down for 12 h. The vehicle was then driven with a Highway Fuel Economy Test (HWFET) drive cycle, and the energy consumption was evaluated. A reference case with pack encapsulation was considered and found that the battery pack was warmer, compared to cases without encapsulation, at the end of the parking phase resulting in reduced heater energy expenditure. Since the batteries operate at temperatures closer to the ideal operating range,

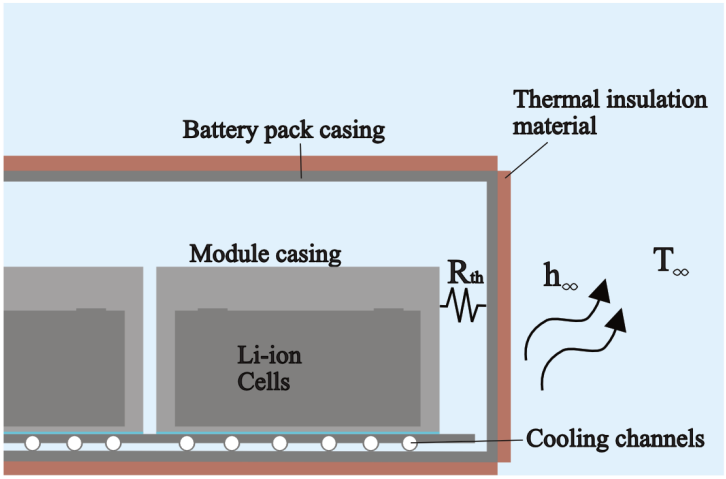

Figure 4.6: *Thermal encapsulation of the battery pack.*

the performance is also improved. The thermal resistance of the insulating material played a significant role in reducing heat loss in cold environments leading to the observed energy savings. The results presented in this section are for the battery pack used in Paper E based on the methodology and results from Paper B.

Cool-down trends are presented for the baseline and encapsulated battery packs with increasing thermal resistance in Figure 4.7a. The battery pack was initialized to 23°C at an ambient temperature of -20°C. The rate of cooling decreases with increasing thermal resistance and thus, the battery pack with encapsulation experiences reduced heat loss, resulting in higher temperatures. Both the thermal conductivity and the thickness were varied for the insulating material to achieve the respective resistance values. The results indicate that the temperature variation is an exponentially decaying process. This behavior can be captured using an equation with the form [103],

$$\theta(t) = exp(-t/\tau) \tag{4.5}$$

where τ is the thermal time constant, which represents the time it takes for the temperature to drop by 63.2% of the temperature difference. The time constant for each simulated configuration was estimated, and is plotted in Figure 4.7b as a function of the thermal resistance of encapsulation. The temperature decay that is obtained from equation 4.5 was within 1.5% of the simulated values for all cases. The thermal resistance of 0 m^2K/W in the figure represents the baseline battery pack. With increasing thermal resistance, the time constant increases, i.e., the cooling process is delayed. Based on these results, a curve-fit was generated between thermal resistance and time constant,

$$\tau^*(R_{th}) = \frac{501 \cdot R_{th}^{0.867}}{R_{th}^{0.867} + 16.108} + 13.04 \tag{4.6}$$

As shown in Figure 4.7b, this equation describes the relationship well for the simulated cases between the 0 and 4 m^2K/W, and this function was deemed accurate for further analyses. The intercept of the function is the time constant for the baseline battery pack. The function behaves asymptotically at very high thermal resistances of encapsulation.

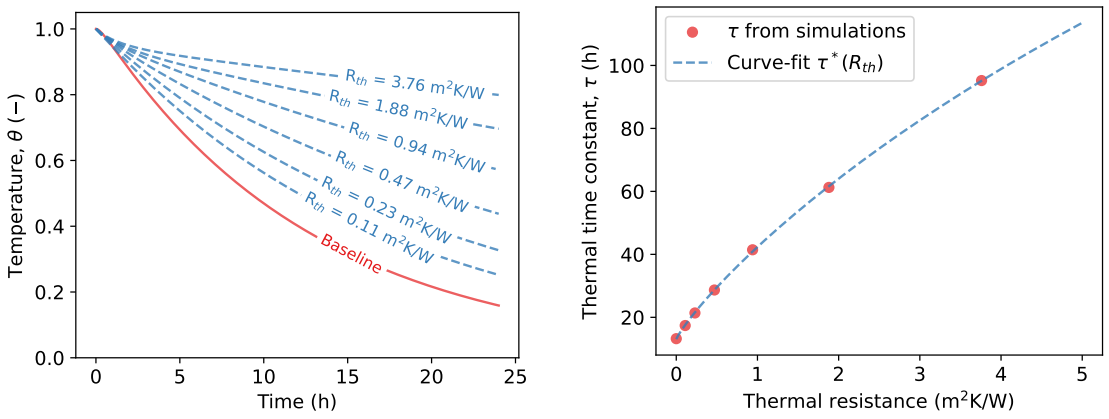

(a) *(b)*

Figure 4.7: *(a) Variation in the battery pack temperature during the parking phase comparing the baseline and encapsulated configurations. (b) Effect of thermal resistance of encapsulation on the thermal time constant.*

Using equations 4.5, and 4.6 in 4.4, the battery pack temperature, T_b, at the end of the parking phase can be computed.

$$T_b = T_\infty + (T_0 - T_\infty) \cdot exp(-t/\tau^*) \tag{4.7}$$

The expression contains three independent variables in t, T_∞, and τ. In the vehicle model (which is discussed in the next chapter), the threshold for battery heating was set to 15°C. So if the battery pack temperature is lower than this threshold at the end of the parking phase, coolant heaters are employed to heat the pack. A preliminary analysis is performed here to understand the effect of these parameters on the energy required for battery heating. The specific energy required, q, is described as,

$$q = \begin{cases} c_p \cdot (T_b - 15) & \text{if } T_b < 15°\text{C} \\ 0 & \text{otherwise} \end{cases} \tag{4.8}$$

where c_p is the specific capacity of the cells of the battery pack. It must be noted that q is the minimum specific energy required to raise the pack temperature to 15°C. In the vehicle, the battery pack continuously loses heat even during heating, and so the energy expenditure is typically higher. The heating energy is derived from both coolant heaters and self-heating during operation.

The effect of the thermal resistance of the pack encapsulation and ambient temperature on the battery pack temperature at the end of a 12 h parking phase, is presented in Figure 4.8a. The black contour line represents the threshold for battery heating. So, for scenarios where the battery pack temperature is under the threshold, coolant heaters would be employed for battery climatization. The minimum energy required per ton of battery pack to heat it to 15°C, is shown in Figure 4.8b. The contour profile is complementary to that in Figure 4.8a, for temperatures under the threshold line. When heating is needed, the required energy increases linearly with decreasing ambient temperature, for a given encapsulation thermal resistance following equation 4.7. Meanwhile, an exponential increase in energy requirement is seen when decreasing the thermal resistance for a given ambient temperature.

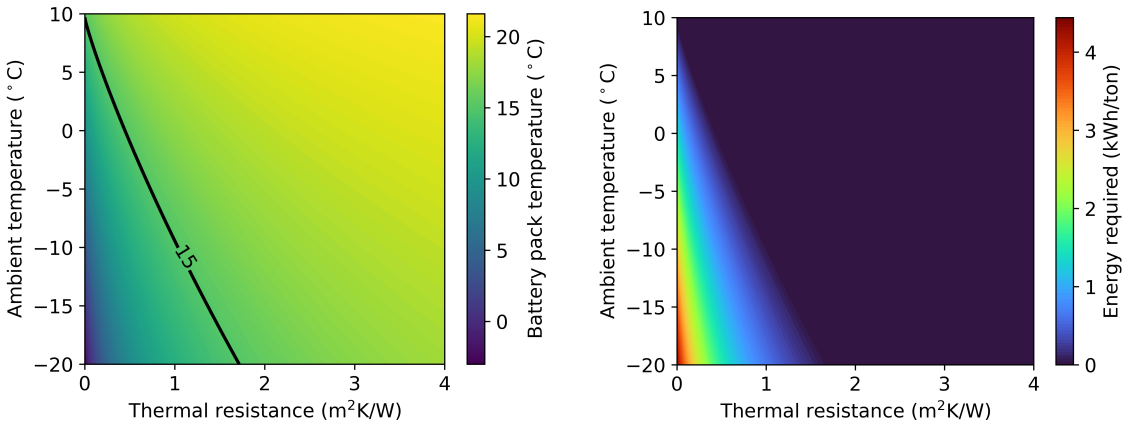

Figure 4.8: *Effect of thermal resistance of encapsulation and ambient temperature, after a 12 h parking phase, on (a) Average battery pack temperature; the black contour line is the threshold for battery heating (b) Energy required for battery climatization.*

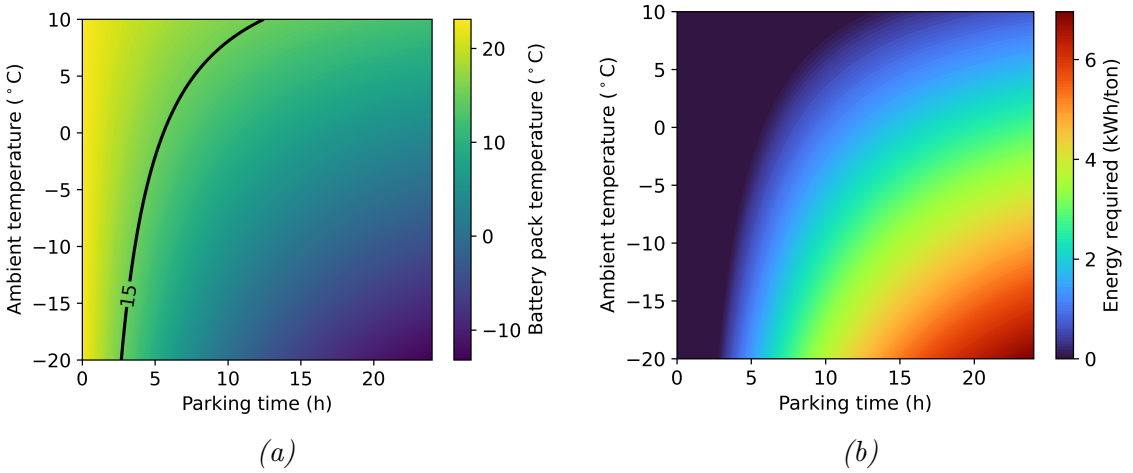

Figure 4.9: *Effect of duration of the parking phase and ambient temperature on (a) Average baseline battery pack temperature; the black contour line is the threshold for battery heating; (b) Energy required for baseline battery pack climatization.*

The effect of the duration of the parking phase and ambient temperature on the baseline battery pack temperature, is presented in Figure 4.9a. A similar contour profile for the energy required to heat the battery pack, Figure 4.9b, is observed for conditions under the threshold temperature. Based on equation 4.7, decreasing ambient temperatures increases the energy requirement linearly, while increasing the parking duration at a given ambient temperature increases the energy requirement exponentially. Based on these results, the heater energy saved using pack encapsulation relative to the baseline pack can be estimated as shown in Figure 4.10. The energy savings are plotted for four thermal resistances, 0.47, 0.94, 1.72, and 3.76 m^2K/W. The energy savings increase with thermal resistance until the battery pack temperature at the end of the parking phase is above 15°C. Thus, for a parking phase of 12 h, a thermal resistance of 1.72 m^2K/W (also illustrated in Figure 4.8a) is sufficient even at -20°C.

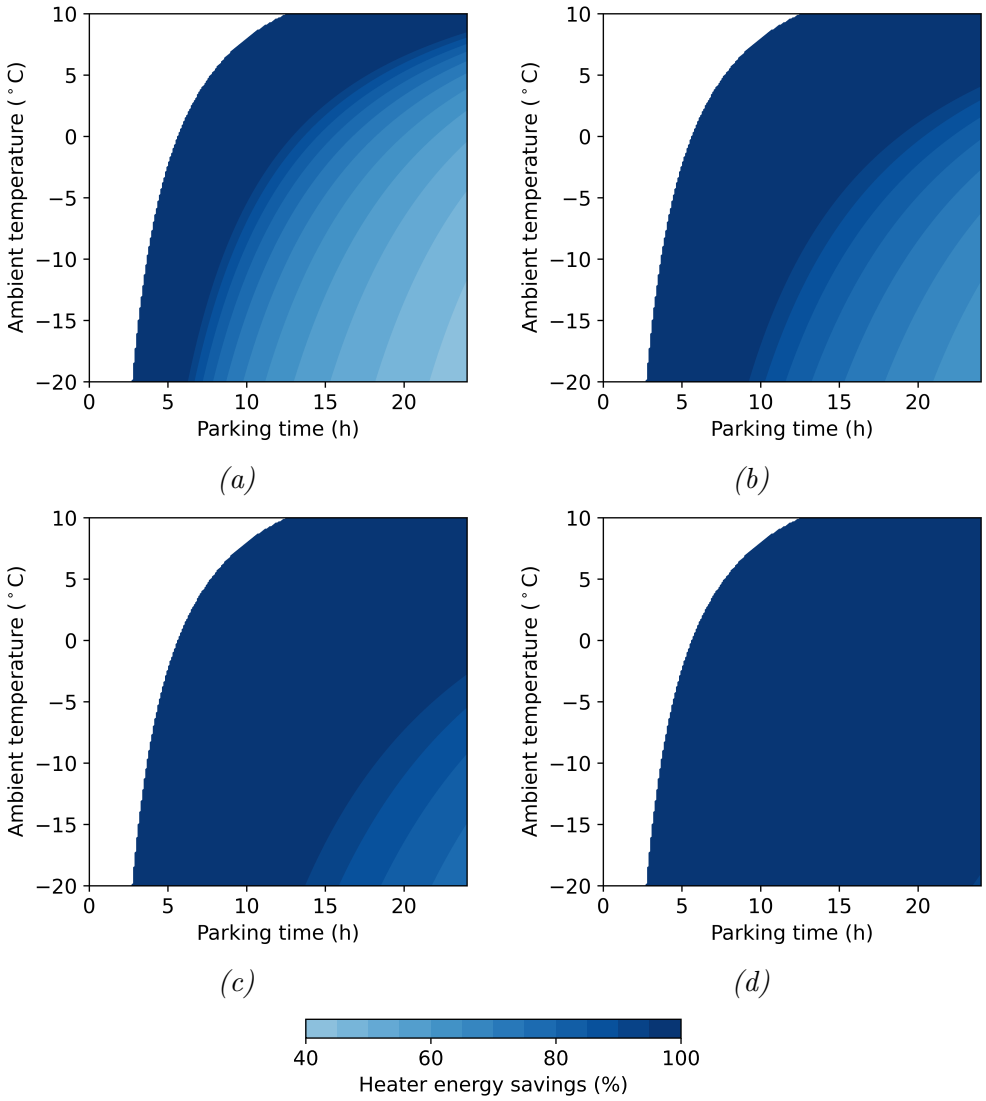

Figure 4.10: *Heater energy savings of the encapsulated configurations relative to the baseline, with varying thermal resistances (a) 0.47 m^2K/W; (b) 0.94 m^2K/W; (c) 1.72 m^2K/W; and (d) 3.76 m^2K/W.*

5

Combined analysis

This chapter presents the influence of the investigated heating load reduction strategies, namely cabin insulation, cabin air recirculation, and battery pack encapsulation, on vehicle performance and driving range. The vehicle system was modeled in the commercial simulation platform, GT-SUITE. First, the various subsystems are discussed, followed by the simulation procedure focusing on the investigated scenarios, and finally the results. More discussions of the combined analysis can be found in Paper E.

5.1 Vehicle subsystems

The vehicle considered was a fully electric truck and its main specifications are presented in Table 5.1. Figure 5.1 illustrates a schematic of the simplified truck model. Three main vehicle subsystems were considered: a simplified vehicle powertrain model, vehicle thermal management system, and system controllers.

5.1.1 Vehicle powertrain

The vehicle had three axles, each assumed to be equally weighted and driven by an electric motor through a differential. The electric motors also served as generators to recuperate energy while braking. The efficiency map of the electric machine as a function of the normalized torque and speed is shown in Figure 5.2. The traction power was calculated as

$$P_v = \left(M_v a_v + \frac{1}{2} \rho v_v^2 C_d A_{f_v} + \mu_r M_v g \cos(\beta) + M_v g \sin(\beta) \right) v_v \tag{5.1}$$

where M_v is the mass of the vehicle, a_v is the acceleration, ρ is the density of air, v_v is the velocity of the vehicle, C_d is the coefficient of drag, A_{f_v} is the frontal area, μ_r is the rolling resistance coefficient of the tyre, g is the acceleration due to gravity and β is the road gradient. In this study, only a flat road was considered and so, β was zero.

Parameter	Value
Vehicle mass (M_v)	20000 kg
Drag coefficient (C_d)	0.5
Frontal area (A_{f_v})	10 m^2
Gear-train efficiency	0.855

Table 5.1: *Truck specifications.*

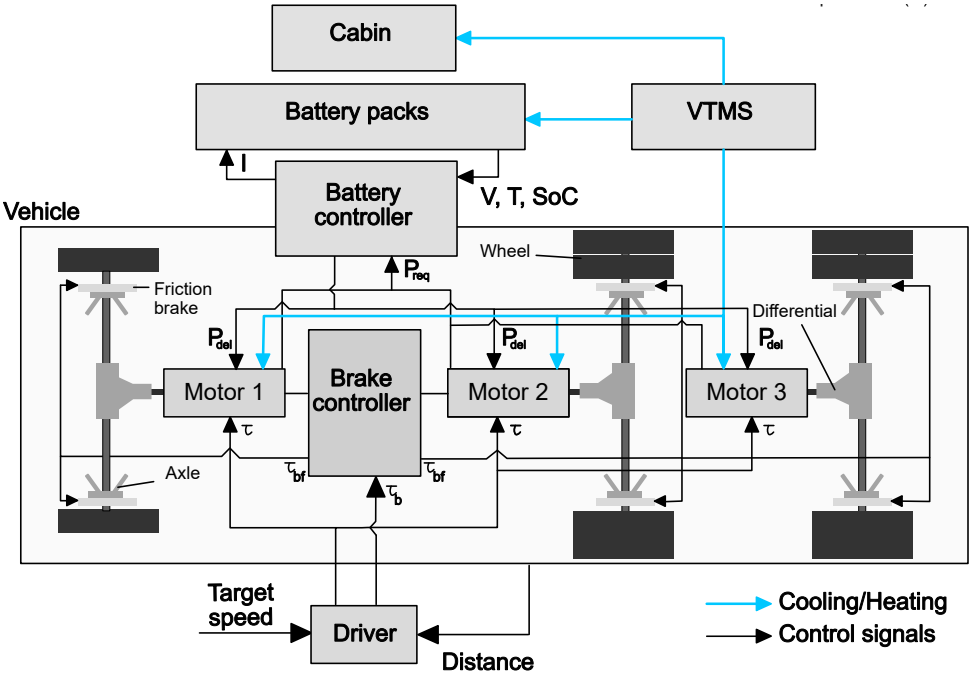

Figure 5.1: *Schematic of the simplified truck model.*

To account for the variation in the traction load due to operating temperatures, the air density was modeled based on the ideal gas equation accounting for ambient temperature at 1 bar ambient pressure. C_d was considered to have a constant value of 0.5, though it can show slight variations at different ambient temperatures. The rolling resistance coefficient was modeled based on the works of Hyttenin [24, 119] where it was defined as a function of the tyre temperature and vehicle velocity. The tyre temperature was initialized to the same value as the ambient, and its variation was computed based on ambient temperature and vehicle velocity. The rolling resistance coefficient was then computed instantaneously as a function of velocity and tyre temperature.

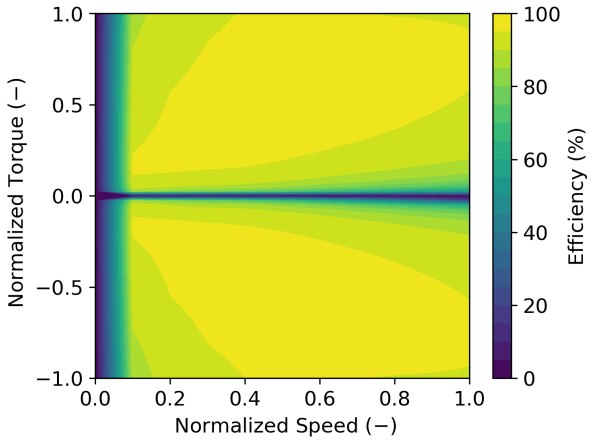

Figure 5.2: *Electric machine efficiency map.*

The electric machines received information about the maximum discharge/charge ability (discussed below) of the batteries during each timestep in the simulation. During braking, the brake controller unit received messages about the maximum power that could be sent to the batteries to be stored and the maximum braking torque the motor could produce. If the regenerated power was lower than the maximum charge threshold, the batteries were charged whereas if the regenerated power exceeded the maximum threshold, the batteries charged at their limits, and the friction brakes supplied the rest of the braking torque. The electrical losses to/from the battery pack were assumed to be 8% (personal communication). Finally, the vehicle was driven by a driver model whose input was a prescribed target speed. The driver model requested torque equally from the three electric motors to match the vehicle speed and the target speed.

5.1.2 Vehicle thermal management system

The thermal management architecture for the vehicle consisted of five circuits, as shown in the schematic in Figure 5.3.

- The vehicle included six battery packs and coolant hoses were connected in parallel to each pack. The battery circuit had a pump and heater in series, and a chiller for cooling using the refrigerant loop. The chiller was operated when the battery pack temperature was above 28°C, and until the pack temperature decreased below 26°C. The 10 kW heater downstream of the pump was employed for battery heating if the initial average temperature of the battery pack was below 15°C. The battery circuit was opened to the E-machines circuit using valve V2 if battery pack heating was necessary and when the temperature in the outer loop was suitable for heating.

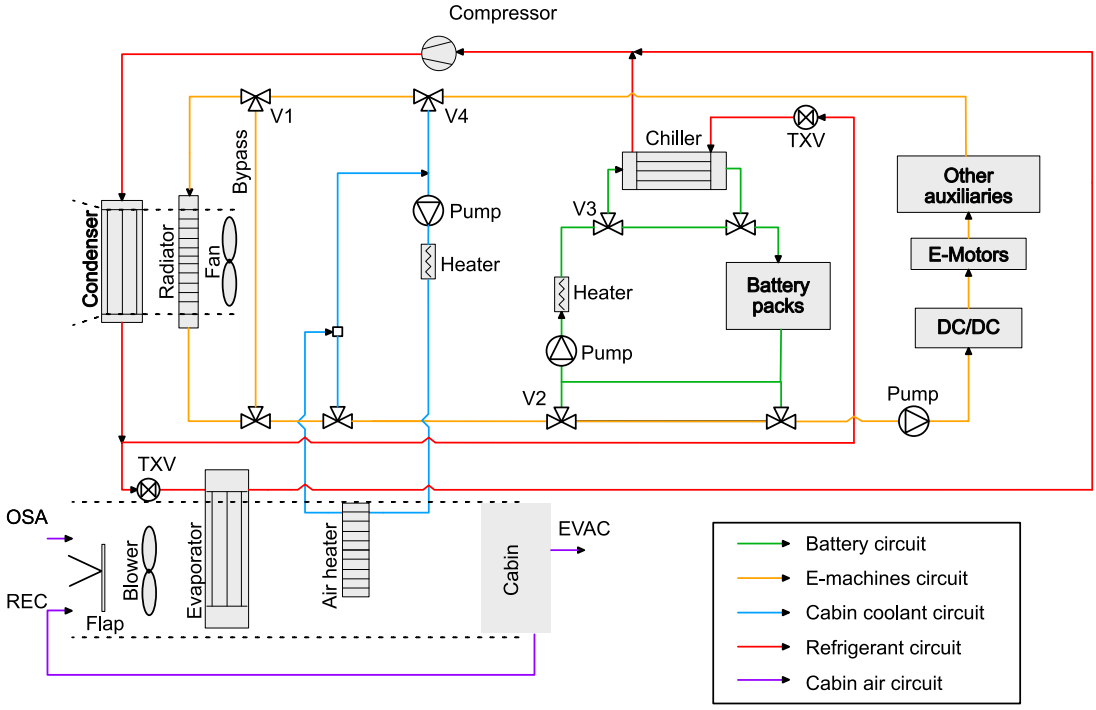

Figure 5.3: *Schematic of the vehicle thermal management system.*

- The components in the E-machines circuit were connected in series, while identical components, i.e., each of the three motors, were connected in parallel with the others. The E-machines circuit included a radiator for cooling. A thermostat was modeled to regulate the temperature in the circuit by allowing coolant to bypass the radiator when necessary using valve V1.
- The cabin coolant circuit consisted of three components: a pump, a coolant heater, and an air heater to heat the cabin air entering the cabin. The waste heat from the E-machines circuit could be used for this purpose if the temperature was between 1°C and 3°C above the required temperature of the coolant using valve V4. Outside this operating condition, the heater was employed to achieve the required inlet air temperature.
- The refrigerant circuit was modeled for dehumidifying the cabin air at the evaporator, along with a secondary loop equipped with a chiller for battery cooling. A variable-speed compressor was used and the speed was regulated based on the cooling request at the chiller and evaporator. To achieve the desired effect at the heat exchangers, the coolant flow rate at the chiller was regulated with valve V4 controlled by a PI controller. Expansion valves (TXV) upstream of the evaporator and chiller were employed to expand the hot refrigerant and to achieve a target degree of superheat upstream of the compressor. The evaporator was operated when the dew point temperature of the ambient air was above 5°C, aiming to cool down the air to 3°C. The chiller operated if the average battery pack temperature was above 28°C, and cooled until the pack temperature was below 26°C.
- The cabin air circuit was used to climatize the cabin. The main components of this circuit are a blower, an evaporator, an air heater, and the cabin. The blower drew air from the ambient outside air (OSA) and/or the cabin through recirculation (REC). The blower speed was set depending on the ambient temperature and maintained throughout the simulation. The temperature in the cabin air circuit was controlled by the evaporator and the cabin air heater, aiming to maintain 22°C. The cabin coolant heater rate was limited such that the maximum air temperature entering the cabin during heating was $40-T_\infty$ (°C). The requested recirculation ratio was achieved through a PI-controlled flap as shown in the figure.

A fan was placed in the under-hood compartment downstream of the radiator and was used when the vehicle velocity was less than 10 km/h, and if there was either coolant flow through the radiator or refrigerant flow through the condenser. Finally, a deaeration system (not shown in the figure) was included to prevent overpressure due to coolant expansion under heating or to supplement the primary systems with additional coolant when coolant contracts under cooling, which would otherwise create a negative pressure. In addition, the expansion tank aids in preventing cavitation by providing a high pressure upstream of the pump. The power required to run all the auxiliary components was considered during vehicle operation.

The battery pack model used in the vehicle simulations was the same as in Chapter-4 and the validation for the battery pack model is presented in section 4.1.2. The validation for the cabin used in the vehicle simulations is discussed in Paper E. For completeness, a brief model description is described below.

The cabin air was modeled as a single control volume, where the transport equations for the

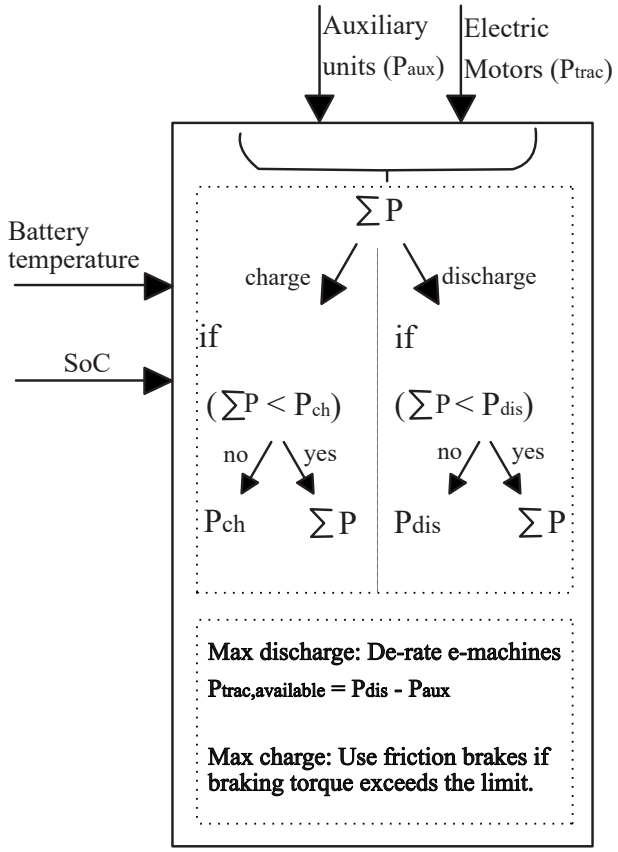

Figure 5.4: *Battery management system.*

temperature, CO_2, and humidity are solved in the time. The cabin solids were modeled as lumped thermal masses, and heat transfer to these solids was calibrated by imposing suitable heat transfer coefficients to each solid as functions of the HVAC inlet mass flow rate. The external heat transfer coefficient was imposed based on vehicle velocity as shown in Figure 3.16b. The heat transfer from the cabin air to the solids, HVAC heater rate, and the mean front windshield temperature are compared in Paper E for model verification, and the 0D cabin model was considered to be sufficiently accurate for vehicle simulations.

5.1.3 System controls

Battery management system

The simplified control logic for the battery pack simulations is shown in Fig. 5.4. The total electrical power, i.e., the sum of traction and auxiliary loads, requested/delivered from/to the pack was passed through the controller. This power was then converted to discharge/charge current by the battery pack based on its terminal voltage. Additionally, the battery pack's maximum discharge/charge ability in terms of power was considered in the controller for battery longevity. It was defined as a function of temperature and SoC as shown in Fig. 5.5a and Fig. 5.5b, respectively. When the discharge power request from the batteries exceeded the limit, the e-machines were de-rated to accommodate the total auxiliary loads. If the power regenerated exceeded the charging ability, batteries were charged at their limits, and friction brakes were

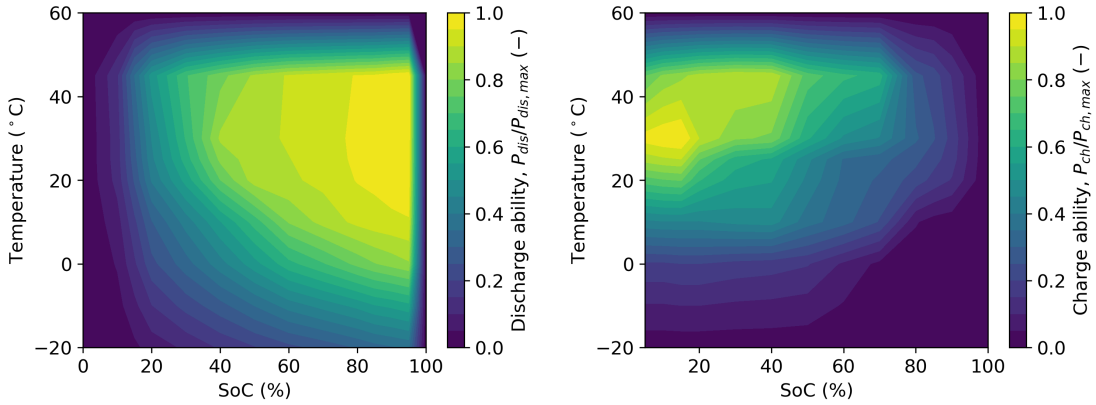

Figure 5.5: *Battery performance abilities as functions of SoC and temperature (a) Normalized battery discharge ability; (b) Normalized battery charge ability.*

employed for the rest of the braking torque.

Recirculation controller

The control strategy for the adaptive recirculation was based on equation B.6, the steady-state 0D cabin solution presented in Appendix B. The target dew-point for humidity was defined depending on the ambient temperature and vehicle velocity, as explained in Appendix D. Once the recirculation ratio was computed, the HVAC flap was controlled with a PI controller such that the fresh and recirculated air into the cabin satisfied the target values.

5.2 Simulation methodology

To capture the vehicle's performance, a transient operating cycle was used based on the recommendations from Romano et al. [120]. In their work, operating cycles were shown to provide a more realistic description of the environment that a typical driving cycle can not provide. To this end, the operating cycle was used to generate a stochastic representation of the road for a

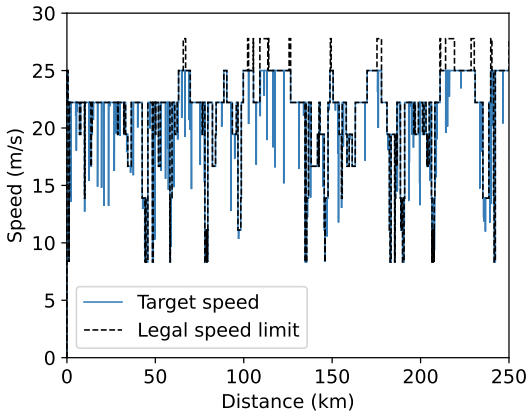

Figure 5.6: *Legal speed limit and the driver's target speed.*

distance of 250 km. A representative cycle describing the legal speed limit (v_{legal}), stop times, and road curvature (Y) was generated as functions of distance, illustrated in Figure 5.6, was chosen for this study.

With the resulting cycle, the driver was considered to operate such that the maximum truck speed was 25 m/s following the regulations in Sweden for heavy vehicles [121], and the lateral acceleration due to road curvature within 4.9 m/s^2. Thus, the target speed was defined as

$$v_{target} = \min(25, v_{legal}, \sqrt{4.9/Y}) \tag{5.2}$$

Five ambient temperatures were considered, 20°C, 10°C, 0°C, -10°C, and -20°C. The simulations were performed to investigate:

- Influence of ambient temperature on the vehicle performance at 70% RH and one occupant.
- Combined effect of the investigated strategies on the vehicle performance at 70% RH and one occupant.

The effect of higher ambient relative humidity and number of occupants on the effectiveness of the strategies is included in Paper E.

A parking-driving scenario consisting of a 12 h parking period followed by driving was studied. The average battery pack temperatures were initialized based on the results from equation 4.7, with an initial temperature of 23°C and the time constant corresponding to the battery pack configuration (baseline or encapsulated) for all scenarios with a parking duration of 12 h. The cabin and all cooling circuits were initialized to the same temperature as the ambient. Once the driving phase started, the driver targeted the speed obtained from the operating cycle. The battery packs were initialized to 80% SoC, and driving was carried out until it dropped to 20%. The auxiliary components were operated during the driving phase, and heating/cooling to the cabin and battery packs were provided depending on the scenarios.

For the cases with battery pack encapsulation, a thermal resistance of 1.72 m^{2}K/W was considered as it eliminated the need for the use of battery heating at -20°C for a parking duration of 12 h, as discussed in section 4.2. For the cases with cabin insulation, a thermal resistance of 4 m^{2}K/W was considered based on the results in section 3.1.2. The additional mass due to the insulation was included in the total mass of the truck although it was negligible compared to the vehicle mass.

5.3 Vehicle performance analysis

Figure 5.7a demonstrates the good agreement between the target and simulated speeds when subjected to the operating cycle at 20°C. Based on the driver's torque request, the E-motors draw/deliver current, Figure 5.7b, from/to the batteries. The operating power complies with the battery pack control logic as explained in subsection 5.1.3.

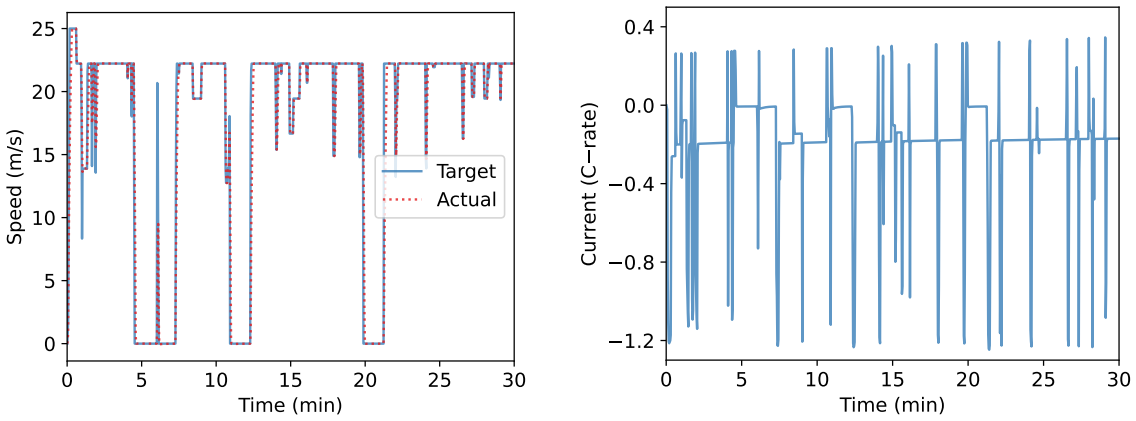

(a) *(b)*

Figure 5.7: *(a) Comparison between the target and actual speeds of the truck during the first 30 minutes of the cycle at 20°C; (b) Current request to the battery pack.*

5.3.1 Influence of ambient temperature on the vehicle performance

The ambient temperature's influence on the baseline vehicle, i.e., without cabin insulation, cabin air recirculation, and battery pack encapsulation, is discussed in this subsection.

Figure 5.8 describes the vehicle's range and energy consumption at the various ambient temperatures normalized to those at 20°C. The distance traveled by the vehicle decreases with decreasing ambient temperature as much as 37.6% at -20°C as compared to 20°C. The energy consumption increases with decreasing ambient temperatures by about 58% at -20°C.

The reasons for this behavior are explained by Figure 5.9. Each bar represents the degree of energy from the battery used for each influencing factor. About 8% of the energy is lost due to electrical losses for all scenarios. The majority of the energy is used for traction, i.e., to overcome the aerodynamic, rolling resistance, energy spent to accelerate the vehicle but lost at the friction brakes, and the losses at motors and gears, for all scenarios. However, at lower

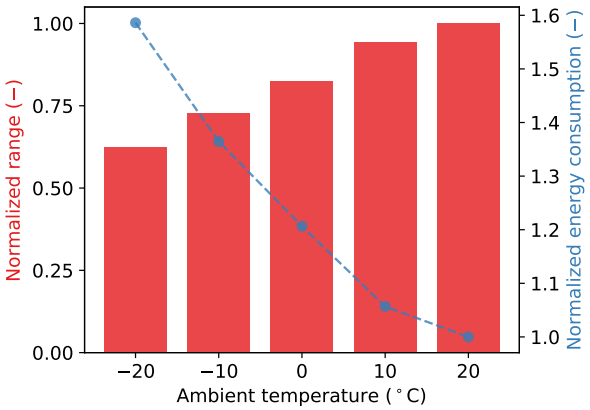

Figure 5.8: *Normalized vehicle range and energy consumption at different ambient temperatures.*

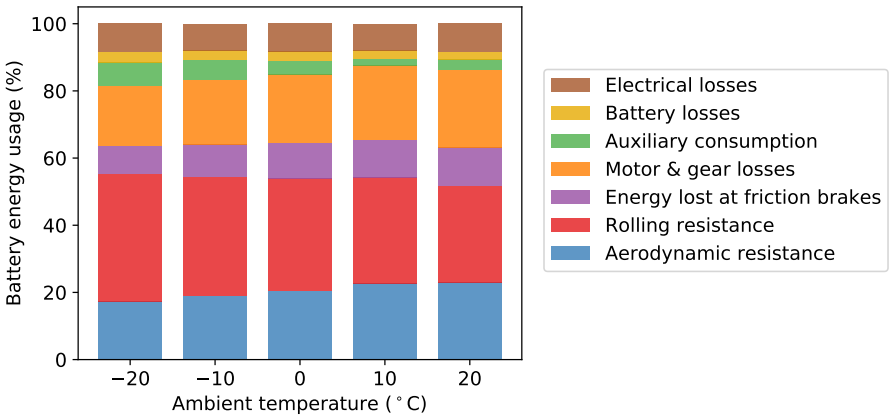

Figure 5.9: *Factors influencing energy expenditure at different ambient temperatures.*

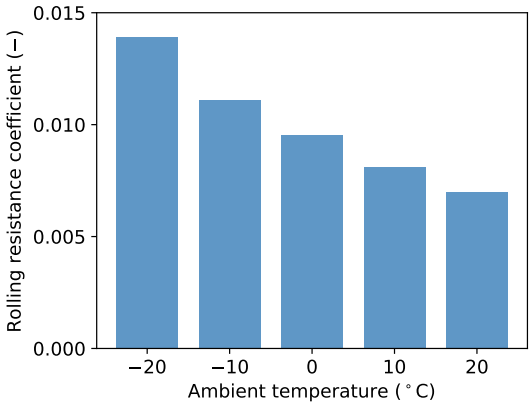

Figure 5.10: *Mean rolling resistance coefficient for the operating cycle at different ambient temperatures.*

ambient temperatures, the percentage of energy used for traction decreases and the energy used for auxiliaries and battery losses (marginally) increases, which is in good agreement with the literature presented in Chapter-2. Among the traction resistances, the contribution of the rolling resistance increases while the others decrease at low temperatures. The aerodynamic force increases at lower temperatures due to higher density. Yet, the percentage of energy in overcoming the resistance decreases due to the reduced distance traveled (see Figure 5.8). Meanwhile, the rolling resistance energy usage increases even with the lower distance due to the higher rolling resistance coefficient at low temperatures. As mentioned earlier, this parameter was modeled to be temperature-dependent and increases with a decrease in tyre temperature. The mean rolling resistance coefficient of the cycle for each scenario is plotted in Figure 5.10, and it can be seen that the values increase steadily from 0.007 at 20°C to 0.014 at -20°C.

The auxiliary energy expenditure increases by over 3.5 times from 10°C to -20°C, effectively ranging from 1.98% to 7.08%, respectively. Figure 5.11 illustrates the factors contributing to this increase. The mean auxiliary consumption increases fivefold, from about 1.8 kW at 10°C to 9 kW at -20°C. The main ambient temperature-dependent factors are cabin heating, battery heating, compressor, and underhood fan. All the other auxiliaries, such as the pumps and blowers have

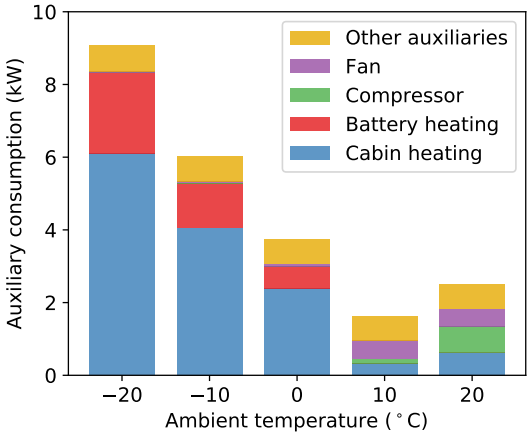

Figure 5.11: *Factors influencing the auxiliary energy consumption at different ambient temperatures.*

approximately the same effect at all operating temperatures. The cabin heating load is the largest auxiliary load at low ambient temperatures as the heater operates to target a mean cabin temperature of 22°C, as shown in Figure 5.12a. This is followed by battery heating for ambient temperatures below 0°C. For these scenarios, the battery pack temperature at the end of the 12 h parking phase is below the 15°C threshold as illustrated in Figure 5.12b, and thus battery heating is necessary. The compressor is not used at temperatures below 0°C, since dehumidification is not necessary. For the duration of the cycle, the battery chiller is not employed for these scenarios. Moreover, at these temperatures, the fan is employed less frequently than at 10°C and 20°C, as it was engaged only when the vehicle speed was below 10 km/h and if there was coolant flow through the radiator or refrigerant flow through the condenser.

Surprisingly, the scenario at 10°C has the lowest auxiliary energy consumption among the five

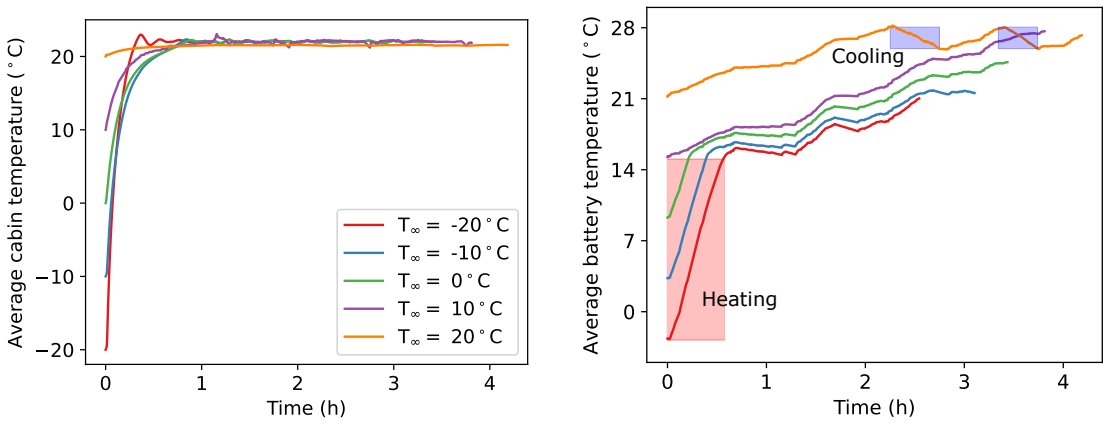

(a) *(b)*

Figure 5.12: *Comparison of (a) Average cabin temperature; (b) Average battery pack temperature. The red band represents the zone where battery heating is employed and the blue band represents the region where battery chiller is employed.*

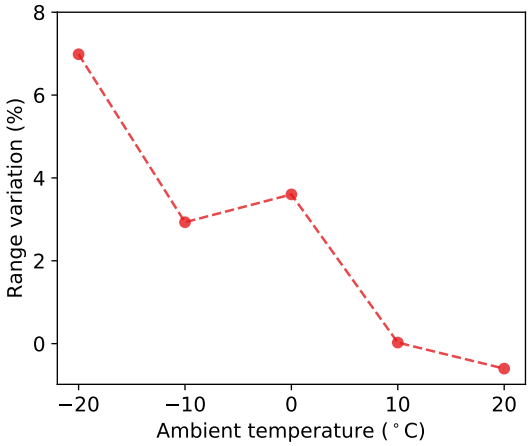

Figure 5.13: *Percentage variation in vehicle range with the investigated strategies, as compared to the baseline vehicle at respective ambient temperatures.*

scenarios. The main reason is that the coolant temperature in the cabin coolant circuit required to maintain the cabin at 22°C is within the same margins as the coolant temperature in the outer E-machines circuit. Thus, the valve V4 (see Figure 5.3) is opened, mitigating the usage of the heater in the cabin coolant circuit.

The scenario at 20°C has the second lowest auxiliary energy consumption among the considered cases. The compressor requires the most energy as it cools both the evaporator, for dehumidifying the cabin air, and the battery chiller, for cooling the battery packs. The HVAC cabin air requires cabin coolant heating to reheat the air leaving the evaporator so that the temperature entering the cabin is at an appropriate level.

5.3.2 Combined effect of the investigated strategies on the vehicle performance

The effect of each strategy individually is discussed in Paper E, and only the combined effects on vehicle performance are presented below.

Figure 5.13 describes the percentage increase in vehicle range with all the strategies included as compared to the baseline vehicle range at the same ambient temperature. The range increases below 0°C, up to about 7% at -20°C. The reason for the increased range gains at low ambient temperatures is mainly because of the effect that these strategies have on the auxiliary energy expenditure as seen in Figure 5.14. With the inclusion of these strategies, the energy requirement for the auxiliary components decreases, thus increasing the energy available for traction. At 10°C, no significant variation in vehicle range was seen while at 20°C, a marginal increase in the auxiliary energy expenditure is noted and is the main reason for the slightly lower range (-0.6%) in this scenario for the vehicle with all strategies included.

The components influencing auxiliary energy consumption are compared for the two configurations in Figure 5.15. For ambient temperatures below 0°C, the mean auxiliary energy consumption decreases by over 50% for the vehicle with all strategies as compared to the baseline configuration.

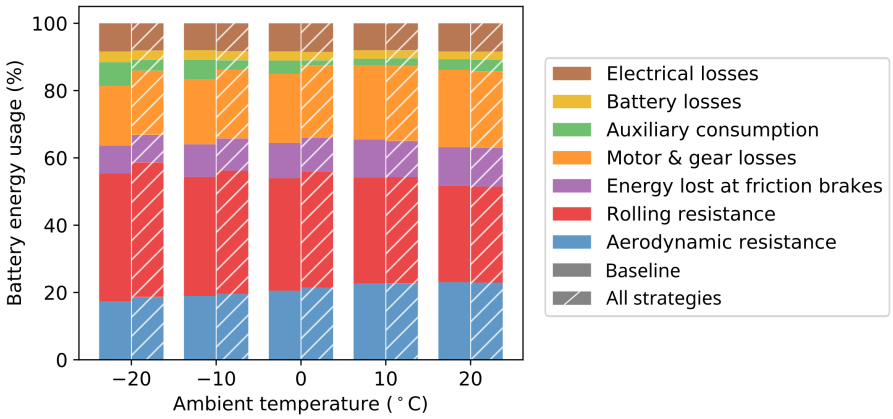

Figure 5.14: *Factors influencing energy expenditure at different ambient temperatures comparing the baseline vehicle and a vehicle with all strategies included.*

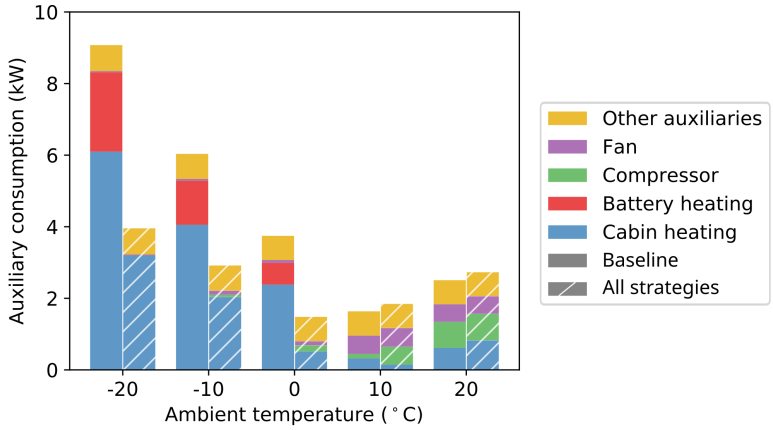

Figure 5.15: *Factors influencing the auxiliary energy consumption at different ambient temperatures comparing the baseline vehicle and a vehicle with all strategies included.*

The scenario at 0°C has the lowest auxiliary energy consumption with all strategies included compared to 10°C with the baseline vehicle. The cabin heating load decreases for the scenario at 10°C, but the compressor energy consumption increases considerably, offsetting the cabin heating energy saving. Each strategy has a unique influence on auxiliary consumption. The behavior of the vehicle with all strategies is characterized by three main features:

- No battery heating requirement
- Higher compressor engagement.
- Lower cabin heating requirement

The first two factors are due to the usage of battery pack encapsulation. As discussed in Chapter-4, by insulating the battery pack, its temperature can be retained at a sufficiently high value so that the energy required for battery heating in the subsequent cycles can be mitigated.

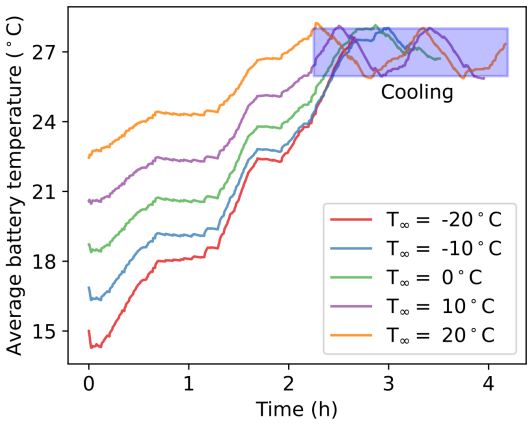

Figure 5.16: *Average battery pack temperature with thermal encapsulation. The blue band represents the zone where the battery chiller is employed.*

The thermal resistance used for encapsulation was 1.72 m^2K/W, which eliminated the need for battery heating when the parking duration was 12 h even at -20°C as shown in Figure 4.8 and Figure 4.10. Meanwhile, due to better insulation, the cooling requirement of warm battery packs increases slightly. The battery packs are entirely reliant on the cooling system which increases the demand on the refrigerant system. The insulated battery pack temperatures are plotted in Figure 5.16, and it can be seen that temperatures reach the threshold for chiller employment at a faster rate than the baseline packs as shown in Figure 5.12b. The energy spent for cooling the insulated battery pack is greater than the baseline pack for ambient temperatures above -10°C. Nevertheless, the energy gain from using battery pack encapsulation for cases below 0°C outweighs the energy expenditure due to compressor-chiller employment during one battery cycle as seen in Figure 5.15.

A significant reduction in the cabin heating load is noted for cases below 10°C. This behavior is due to both cabin insulation and cabin air recirculation. Using cabin insulation reduces the ambient load, and the inlet temperature required to maintain the cabin at 22°C is reduced as

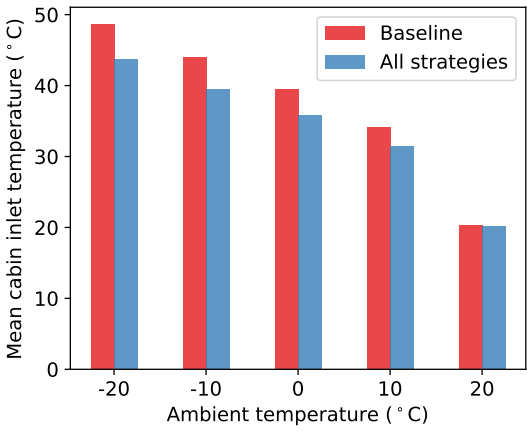

Figure 5.17: *Mean cabin inlet temperature of the operating cycle comparing the baseline vehicle and a vehicle with all strategies included.*

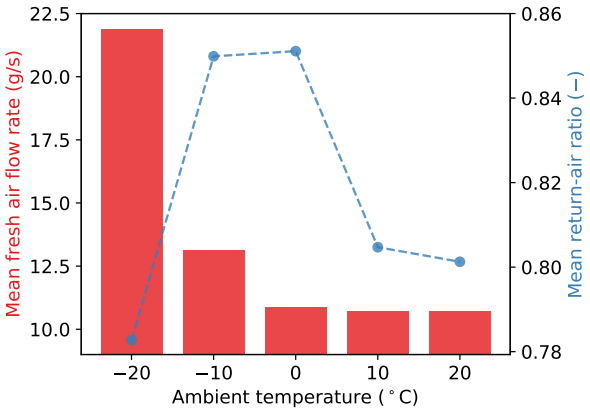

Figure 5.18: *Mean fresh-air flow rate in red, and mean return-air ratio in blue for the vehicle with all strategies at various ambient temperatures.*

seen in section 3.3. The blower speed in the cabin air circuit was maintained constant for each scenario. With recirculation, the mass flow rate through the HVAC system increases by about 10 g/s due to the difference between the operating pressure in the cabin and that upstream of the blower. The combined effects cause the mean cabin inlet temperature to reduce as shown in Figure 5.17. Due to the inlet temperature reduction, the scenarios at 0°C and 10°C are within the same margins as the coolant temperatures in the E-machines circuit, thus making it possible to use waste heat for cabin heating by opening valve V4 (see Figure 5.3). Thus a larger relative reduction in heating load is observed for 0°C and 10°C due to both strategies.

The RAR controller operates as shown in Figure 5.18. Based on these results, scenarios above 0°C are CO_2-critical, with a fresh-air intake of approximately 10 g/s to maintain mean CO_2 at 1000 ppm. The scenarios at -10°C and -20°C are humidity-critical, allowing about 13 g/s and 21.8 g/s of fresh air, which corresponds to 84.9% and 78.5% mean return-air ratio. As mentioned earlier, the mass flow rate is increased with recirculation and raises the cabin heating load marginally at 20°C, which is the main reason for the reduction in vehicle range at 20°C. Nevertheless, these results are in line with the discussions in section 3.2.3 and show that using recirculation at low ambient temperatures is beneficial.

6

Concluding remarks

The objective of this thesis was to investigate the potential of energy-saving strategies by auxiliary load reduction to extend the driving range of battery electric vehicles at low ambient temperatures. Three strategies, cabin insulation, cabin air recirculation, and battery pack encapsulation were investigated for this purpose, and their effects were studied individually, and at the vehicle level.

First, the effect of cabin insulation was explored on a passenger car driven at 50 km/h and -7°C. A conjugate heat transfer numerical procedure was developed and verified with experimental data from tests in a climatic wind tunnel. Six configurations with insulation on various surfaces, including a fully insulated configuration, and four different magnitudes of insulation resistances were tested. For the same heating load, the insulated configurations exhibited higher mean cabin temperatures than the non-insulated configuration as expected. The rate of increase in the average cabin temperature of the insulated configurations was higher than the non-insulation configuration, and thus the cabin can reach the desired temperatures faster. An asymptotic increase in the mean cabin temperature was noted with an increase in insulation resistance for the fully insulated configuration, with about 9°C higher mean temperature than the non-insulated configuration at a thermal resistance of 4 m^2K/W.

The second method explored was cabin air recirculation on a truck cabin. Numerical simulations were performed using a coupled CFD-thermoregulation model, with the consideration of humidity and CO_2. The JOS-3 thermoregulation model for a human was employed for estimations of skin temperatures and evaporation of vapor from the skin. A parametric analysis was performed by varying the ambient temperature, relative humidity, and driving speed to investigate the effectiveness of the recirculation controller. The controller adapted between humidity and CO_2-critical conditions during run-time. The fresh-air mass flow requirements were reduced with increasing differences between the setpoint and ambient vapor mass fractions under humidity-critical conditions and plateaued at 10 g/s where CO2 was more critical. The proposed strategy provided energy savings ranging from 9% to 34% depending on the operating condition. Finally, combining both cabin insulation and RAR control resulted in 41.7% energy savings on the truck, coupled with improved mean overall sensation.

The last strategy was battery pack encapsulation to mitigate the heat loss from the pack to the ambient so that the energy required to heat the pack during the subsequent cycle could be reduced. A module-discretized battery pack model was created to perform electrical-thermal simulations for large battery packs. An electrical circuit model (2RC Thevenin model) was used to capture the electrical characteristics, and Bernardi's heat generation model was used to estimate heat generation from the modules. The model was calibrated with heat-up and cool-down tests to capture the thermal dynamics with coolant and ambient air, respectively, and

validated with test data. Several thermal resistances were tested on the battery pack model during parking to capture the cool-down trends. As expected, the encapsulated battery pack reduced the rate of heat loss and retained the pack at a higher temperature. For a parking period of 12 h, the thermal resistance of 1.72 m^2K/W was required at -20°C for no battery heating.

Finally, these strategies were investigated at the vehicle level. A simplified vehicle model was developed, consisting of a powertrain model, a vehicle thermal management system, and system controllers to perform transient operating cycle simulations. The baseline vehicle energy consumption was 58% higher at -20°C, as compared to 20°C, resulting in a range loss of 37.6% when operated after a 12 h parking period. One of the reasons for this was the increased auxiliary energy consumption, especially the high battery and cabin heating loads at low ambient temperatures. Upon including the strategies (cabin insulation, cabin air recirculation, and battery pack encapsulation), the range improved for scenarios lower than 0°C. The use of battery encapsulation eliminated the need for battery heating at low temperatures but required greater cooling efforts at higher ambient temperatures. The use of cabin insulation and cabin air recirculation decreased the cabin heating loads greatly for operating scenarios under 10°C. Using these strategies reduced the HVAC inlet temperature required to maintain the setpoint temperature in the cabin, promoting waste heat usage for cabin heating at 0°C and 10°C. With cabin air recirculation, the mean fresh-air mass flow decreased from 21.8 g/s at -20°C to 10 g/s for conditions above 0°C. The combined effects of the investigated strategies resulted in range gains of up to 7% at -20°C.

6.1 Future work

In this work, numerical investigations of the heating load reduction strategies were performed. Experimental validations of these methods are essential to comprehensively understand their behavior and gain deeper insights at both component and vehicle levels. Although some experimental validation was performed for cabin insulation, a more extensive investigation remains necessary.

The investigated methods can be integrated with techniques that efficiently deliver heat energy, such as waste heat recovery systems and heat pumps. Additionally, incorporating other strategies to reduce HVAC load, such as steering, seat, panel heaters, heated windshields, localized air-conditioning, and polycarbonate windows, can further decrease the demand for cabin heating. This, in turn, could enhance the energy efficiency of BEVs.

The effect of precipitation, altitude, and other moisture sources present in the cabin and clothes of the occupants should be investigated to effectively control recirculation in the cabin in real-world conditions.

By incorporating predictive models to anticipate the thermal behavior of components in a vehicle, control strategies can be optimized and tailored to operating conditions and planned trips. Such enhancements could lead to improved utilization of waste heat for battery and cabin heating demands.

7

Summary of Papers

7.1 Paper A

System-Level modeling and thermal simulations of large battery packs for electric trucks

This paper is focused on a system-level modeling methodology for thermal simulations of large battery packs for electric trucks. A module-to-module discretization was performed to study the thermal behavior and temperature distribution within the pack. The heat generated from each module was estimated using Bernardi's expression. The conservation equations in 1D formulation for coolant flow through the channels were solved numerically. The pack model was calibrated for thermal interface material properties under a heat-up test. The model evaluation was performed for four charging/discharging and cooling scenarios typical for truck operations. The simulation results were in good agreement with the experimental data with an RMS error of less than 0.55 K when estimating the battery pack temperature, less than 0.26 K when estimating the outlet coolant temperature, and less than 0.4% in the estimation of the SoC of the pack.

7.2 Paper B

Thermal encapsulation of large battery packs for electric vehicles operating in cold climate

The potential of thermal encapsulation of large battery packs for electric truck applications was investigated in this paper. The battery pack modeled in Paper A was used to perform vehicle-level simulations under drive cycle conditions. Parking-driving cycles at various ambient temperatures and a parametric study on the encapsulation characteristics were carried out to assess the energy consumption under each condition. The study showed that a high thermal resistance of the insulation material significantly reduced the heat loss to the environment, acclimatizing the battery pack close to near-optimal operating temperatures. This resulted in potential energy savings of about 15% at -25°C when operating after a 12 h parking period.

7.3 Paper C

Effect of cabin insulation on the heating performance in EVs at low temperatures

This study investigated the effect of heat transfer to the thermal masses on the cabin temperature in a passenger car, and the influence of insulation on different surfaces while climatizing under low ambient temperatures. A conjugate heat transfer model of the cabin was developed, along with a framework to perform transient cabin heat-up simulations. The scenario considered was

a vehicle driving at 50 km/h at -7°C for 40 minutes. Six configurations with insulation on different surfaces, including a fully insulated cabin, and four thermal resistance magnitudes were studied. For the same heating load, the insulated configurations exhibited higher mean cabin temperatures than the baseline cabin. The rate of increase in the average cabin temperature was also higher, meaning that the cabin could reach the desired temperatures faster with insulation. The results from the numerical model agreed well with the experiments performed in a climatic wind tunnel for both the baseline and the fully insulated configurations.

7.4 Paper D

An adaptive cabin air recirculation strategy for an electric truck using a coupled CFD-thermoregulation approach

In this paper, an adaptive recirculation strategy was proposed and studied on an electric truck cabin while heating. Numerical simulations were performed using a coupled CFD-thermoregulation model, with the consideration of humidity and CO_2. The JOS-3 thermoregulation model was employed for estimations of skin temperatures and sweating, and the Berkeley comfort model was used to evaluate the comfort metrics. Ten scenarios were considered at various vehicle speeds, temperatures, and relative humidity levels and evaluated with and without the proposed return-air strategy. The controller adapted between humidity and CO_2-critical conditions during run-time. The fresh-air mass flow requirements were reduced with increasing difference between the setpoint and ambient vapor mass fractions under humidity critical conditions and plateaued at 10 g/s where CO_2 was more critical. The proposed strategy provided heater energy savings ranging from 9% to 34% depending on the operating condition.

7.5 Paper E

Heating load reduction strategies for cabin and battery pack climatization in electric trucks operating in cold climates

The influence of auxiliary heating load reduction strategies on vehicle performance was investigated in the paper. Vehicle simulations were performed for an electric truck operating under parking-driving scenarios at various ambient temperatures. The load reduction strategies included cabin insulation, cabin air recirculation, and battery pack thermal encapsulation. During vehicle operation, the auxiliary energy consumption increased five-fold when the ambient temperature was lowered from 10°C to -20°C on the baseline vehicle. When the heating load reduction strategies were employed, the heating loads for both cabin and battery decreased, leading to a vehicle range increase of up to 7% at -20°C. At a high relative humidity, or with more occupants, the degree of cabin air recirculation that could be employed reduced, resulting in lower range gains.

Appendices

A

Material properties of the solids in the vehicles

Passenger car cabin

Solid ID	Usage	Density (kg/m^3)	Thermal conductivity (W/mK)	Specific capacity (kJ/kgK)
S1	Seats	481	0.05	1300
S2	Carpets	1200	0.18	1200
S3	Windows, sun roof, rear windshield	2500	0.8	750
S4	Front windshield	2237	0.525	965
S5	Seat rails, exterior door, door reinforcements	7832	64	434
S6	Floor	481	0.294	1465
S7	Dashboard, pillars, roof	996	0.2	1400
S8	Center console, inner door panels	1100	0.13	580
S9	Steering assembly	1200	0.19	1400
S10	Middle door, luggage cover	200	0.04	1400

Table A.1: *Thermo-physical properties of the solids in the passenger car cabin [102, 122, 123].*

Truck cabin

Solid ID	Usage	Density (kg/m^3)	Specific capacity (kJ/kgK)	Thermal conductivity (W/mK)
S1	Side windows	2500	840	1.4
S2	Windshield	2338	754	1.1717
S3	Door panels, IP Top storage covers	908	1883	0.26
S4	Floor, motor wall	1030	1913	0.31
S5	Roof	440	1500	0.1
S6	Side, rear walls	1270	1700	0.2
S7	Bunk, seats	410	1210	0.05
S8	Ducts, bunk lower wall	1211	900	0.15
S9	Door mid-panel	908	1400	0.19
S10	Door reinforcements	7832	434	64

Table A.2: *Thermo-physical properties of the solids in the truck cabin [102, 122, 123].*

Solids	Thermal resistance (K/W)
Windshield, side windows Seat, door (all layers)	0
Floor	0.96
Roof	0.08
Top storage covers	18.13
Rear wall	2.40
Motor wall	1.07
Bunk, bunk lower wall	33.01
Side panels	3.28

Table A.3: *Thermal resistance on the outer surface of the solids in the truck cabin.*

B

Steady-state solution for the recirculation ratio from a 0D cabin model

The transport of specific humidity (ω) in the lumped model with one control volume can be described as,

$$m_{cab}\frac{d\omega}{dt} = \dot{m}_{in}(\omega_{bo} - \omega) + \dot{m}_h\omega_h \tag{B.1}$$

where m_{cab} is the mass of air in the cabin, m_{in} is the mass flow rate of air from the HVAC system, $m_h\omega_h$ is the rate at which vapor is introduced by the occupant. The first term on the right-hand side represents the HVAC contribution to humidity transport and the second term represents the source term from the human.

Assuming that the specific humidity at the recirculation outlet is equal to the mean concentration in the cabin, the specific humidity from the blower (ω_{bo}) can be defined as,

$$\omega_{bo} = \gamma\omega + (1-\gamma)\omega_\infty \tag{B.2}$$

where ω_∞ is the ambient specific humidity. Depending on the minimum temperature of the glass, the inlet set-point for specific humidity ($\omega_{in,set}$) can be defined using eqn. 3.8 as $\omega(T_{g,min}-1, 100\%)$. The mean cabin specific humidity can be rewritten from eqn. B.2 as,

$$\omega = \frac{\omega_{in,set} - (1-\gamma)\omega_\infty}{\gamma} \tag{B.3}$$

At steady-state conditions, the left-side term in eqn. B.1 is zero. Substituting eqn. B.3 into eqn. B.1, the recirculation ratio at steady-state for satisfying the humidity criterion (γ_ω) can be defined as,

$$\gamma_{\omega,ss} = \frac{1}{1 + \frac{\dot{m}_h\omega_h}{\dot{m}_{in}(\omega_{in,set}-\omega_\infty)}} \tag{B.4}$$

The transport of CO_2 (α) in a lumped model can be described similarly to eqn. B.1. Upon following the same steps, to maintain 1000 ppm mean concentration in the cabin, the steady-state recirculation ratio for CO_2 criterion can be defined as,

$$\gamma_{\alpha,ss} = 1 - \frac{\dot{m}_h\alpha_h}{\dot{m}_{in}(\alpha_{set} - \alpha_\infty)} \tag{B.5}$$

The final steady-state RAR is,

$$\gamma_{ss} = \min(\gamma_{\omega,ss}, \gamma_{\alpha,ss}) \tag{B.6}$$

C

Recirculation controller

The saturation vapor pressure is an exponential function of temperature (eqn. 3.2), resulting in large variations of the set-point for vapor mass fraction. To make the controller robust under all conditions, the gains were set based on the ambient operating conditions:

$$k_p(T_\infty, \phi_\infty) = -\frac{(1-\phi_\infty)\left(1+\frac{T_\infty+a}{a}\right)}{(x_\omega(T_\infty-1,1)-x_\omega(T_\infty,\phi_\infty))} \tag{C.1}$$

$$k_i(T_\infty, \phi_\infty) = \frac{k_p(T_\infty, \phi_\infty)}{c(T_\infty, \phi_\infty)} \tag{C.2}$$

where $\phi_\infty \in [0,1]$, T_∞ described in °C, a and c are tuning parameters. The parameter a was set to 20 while c was defined as,

$$c = \gamma_{ss} m_{cab} \frac{(\omega_{in,set} - \omega_\infty)}{\dot{m}_h \omega_h} \tag{C.3}$$

where γ_{ss} is the steady state RAR at a given ambient temperature, vapor source, and ambient humidity.

D

Recirculation setpoint for 0D cabin model

In section 3.2, the recirculation setpoint for vapor mass fraction was evaluated at $x_\omega(T_{g,min} - 1, 100\%)$, i.e., 1°C lower than the minimum windshield temperature. Increasing the target dew-point temperature means that the amount of recirculation that can be employed increases leading to greater energy savings but at the expense of possible window fogging. The simulations of the cabin at the vehicle level are performed with 0D models, with one control volume for air and lumped masses for the cabin solids, and provide only the mean temperatures. Thus, the setpoint must be reformulated with the mean window temperature with minimal window fogging.

Firstly, the window temperatures are presented in Figure D.1a for the reference case at the end of 30 minutes. The lowest temperatures occur around the edges of the window. The temperature is highest in the region where the flow from the defroster/demister is incident on the window.

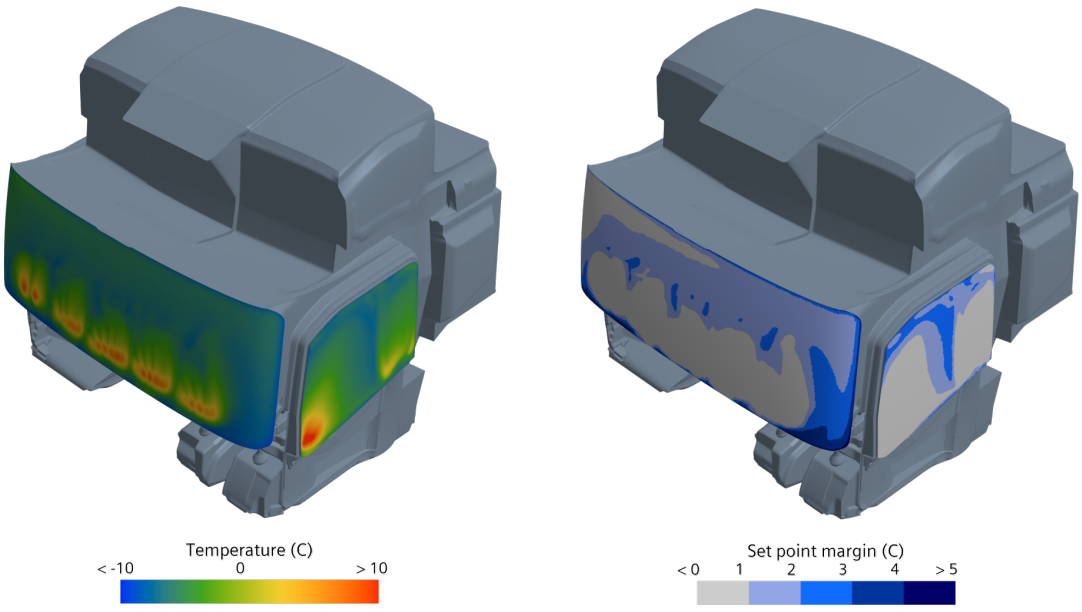

(a) *(b)*

Figure D.1: *(a) Temperature distribution on the window for the reference case at -10°C, 70% RH, and 90 km/h, at the end of 30 minutes. (b) Region of possible fogging with varying setpoint margins.*

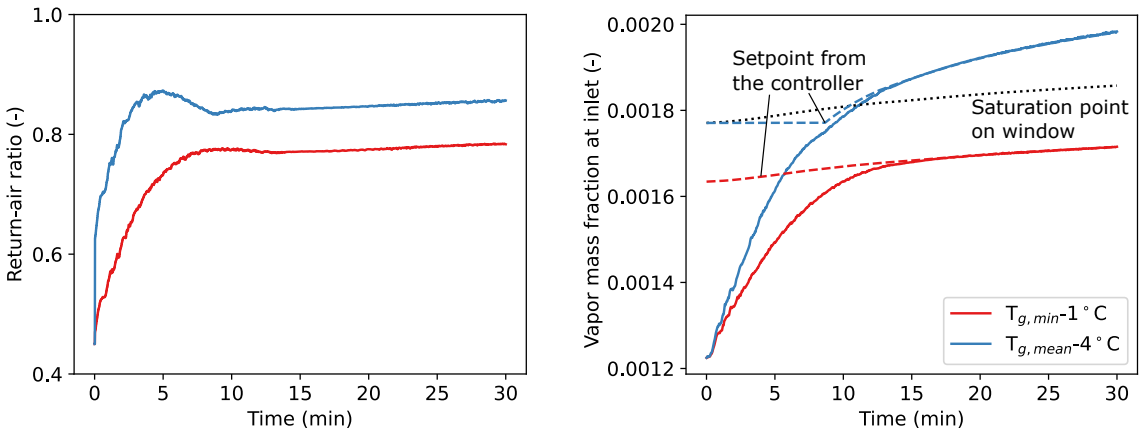

(a) *(b)*

Figure D.2: *Results from the RAR-controller comparing targeting strategies for the humidity controller (a) Return-air ratio; (b) Vapor mass fraction at the inlet.*

There is a sharp decrease in temperature contours outside this region. The minimum window temperature increases from -10°C to -9.4°C, while the mean window temperature at the end of 30 minutes is -4.7°C. Thus, if the controller aims for the vapor mass fraction corresponding to the mean window temperature, about half of the window would fog due to the HVAC flow.

Figure D.1b illustrates the region where potential fogging is targeted while varying the setpoint margin. The setpoint margin is defined as the difference between the mean temperature on the window and the temperature field. If the controller targets a certain setpoint margin below the mean window temperature, the area with margins above that value would fog due to HVAC flow. As shown in the figure, no fogging occurs when the margin is above 5°C, as used in the evaluations in Chapter 3.1. By decreasing the setpoint margin, the controller operates to target a vapor mass fraction such that its dew-point temperature is higher than certain parts of the window, as illustrated in the figure. For example, if the setpoint margin is set to 4°C, the controller targets a vapor mass fraction corresponding to $x_\omega(T_{g,mean} - 4, 100\%)$. This could fog the area where the temperatures are lower than this value. Hence, the band above the setpoint margin 4°C would fog under that condition. Since the 0D recirculation model had an excellent correlation with the CFD results, eqn. B.4 was used to evaluate the amount of recirculation that could be used at $x_\omega(T_{g,mean} - 4, 100\%)$, and yielded 85% RAR for the reference scenario. This could potentially fog around 0.5% of the front window area due to HVAC flow, based on the figure.

To confirm this hypothesis, the reference case was simulated in CFD with the controller targeting $T_{g,mean} - 4$. To improve the robustness of the control strategy and to improve energy expenditure, the targeted value was set as,

$$T_{target,dp} = \max(T_{g,mean} - 4, T_\infty) \tag{D.1}$$

Figure D.2a and Figure D.2b illustrate the recirculation ratio and the vapor mass fraction at the inlet for the two methods. It can be seen that while targeting the mean window temperature the setpoint margin, about 7% more RAR can be employed, which results in about 32.4% savings

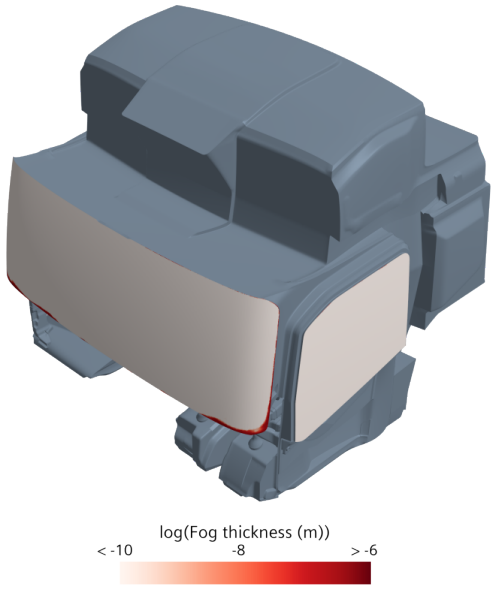

Figure D.3: *Illustration of the fog thickness developed while targeting vapor mass fraction with dew-point temperature* $T_{g,mean} - 4$.

method as compared to 29.3% while targeting the minimum temperature. The vapor mass fraction at the inlet increases above the saturation point for the former case causing slight fogging at the bottom edges. This can be visualized in Figure D.3 where the fog thickness is presented. The observed fogging area is slightly higher at 1.1% than the expected fogging area of 0.5% due to higher local vapor concentration from the occupant's breathing and sweating. Nevertheless, the fogging was not considered to hinder the visibility of the driver.

Based on this understanding, the same approach was extended to various driving speeds as shown in Figure D.4 with a normalized setpoint margin (θ_{set}). Normalization was performed using the difference between the inlet temperature (T_{in}) and the ambient temperature. This was done so that each contour could serve as a representative windshield temperature distribution for different driving speeds across ambient temperatures. The values for the setpoint margin used in the controller are shown in Table D.1. Thus, the recirculation controller targets a dew-point temperature based on the ambient temperature, driving speed, and mean windshield temperature as,

Driving speed (km/h)	**Setpoint margin (−)**
0	0.19
30	0.105
60	0.081
90	0.066

Table D.1: *Variation of normalized setpoint margin at different driving speeds.*

$$T_{target,dp} = \max\left(T_\infty, T_{g,mean} - \theta_{set}(v_{veh}) \cdot (T_{in} - T_\infty)\right) \tag{D.2}$$

The variation in θ_{set} was smoothened using a time filter to reflect mean window temperature changes in vehicle simulations with continuously varying velocities.

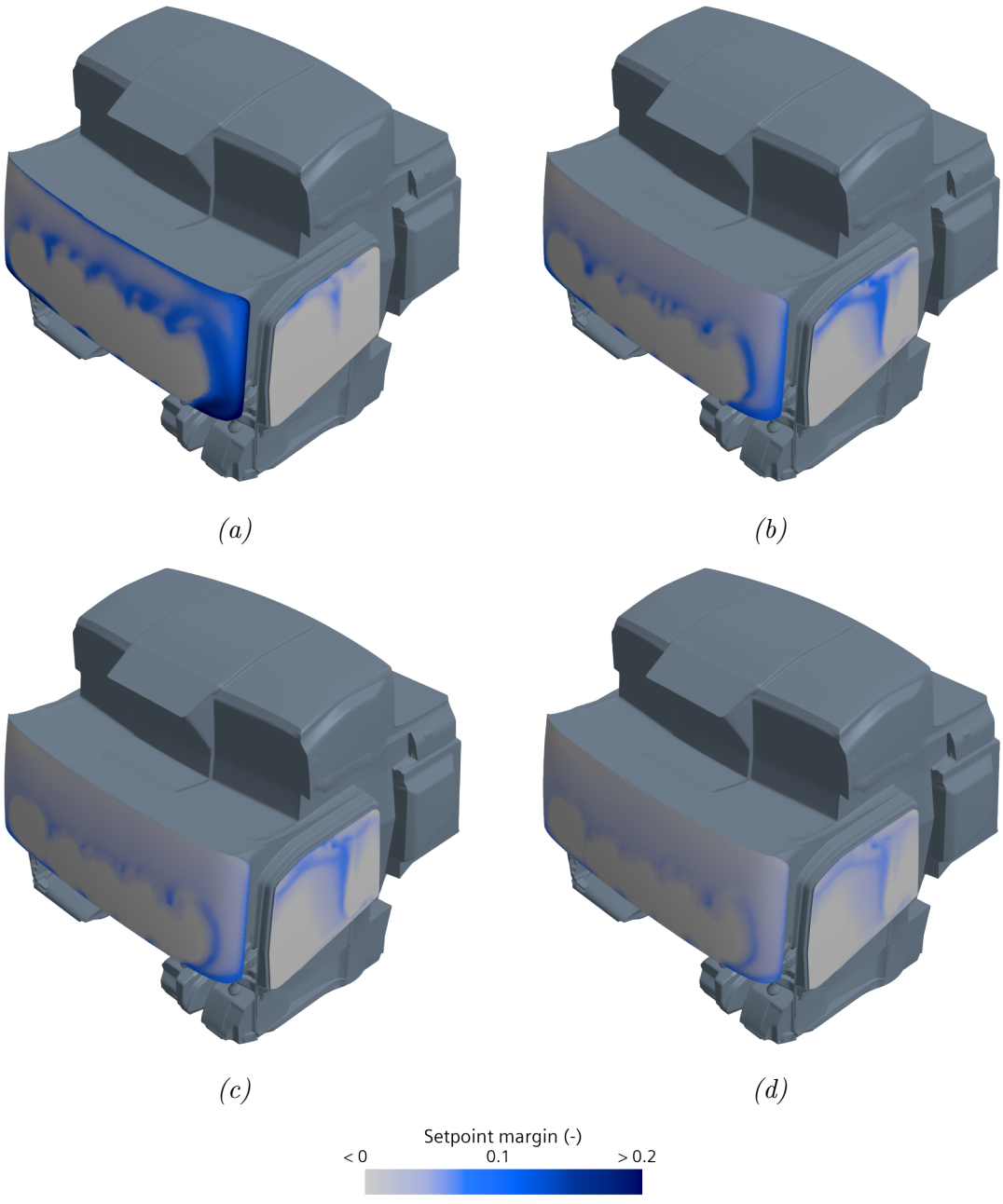

Figure D.4: *Region of possible window fogging with varying normalized setpoint margins at different driving speeds (a) 0 km/h; (b) 30 km/h; (c) 60 km/h; (d) 90 km/h.*

References

[1] Ramesh Babu, A. "Battery thermal management for electric vehicles operating in cold climates". Licentiate. Sweden: Chalmers University of Technology, 2022. URL: https://research.chalmers.se/en/publication/528866 (visited on 2023-12-03).

[2] Statista. "Global Carbon Project. (December 5, 2023). Annual carbon dioxide (CO) emissions worldwide from 1940 to 2023 (in billion metric tons) [Graph]." URL: https://www.statista.com/statistics/276629/global-co2-emissions/ (visited on 2023-12-03).

[3] European Environmental Agency. "Greenhouse gas emissions from transport in Europe". 2023-10. URL: https://www.eea.europa.eu/en/analysis/indicators/greenhouse-gas-emissions-from-transport (visited on 2023-12-03).

[4] Grigoratos, T. et al. "Real world emissions performance of heavy-duty Euro VI diesel vehicles". *Atmospheric Environment* **201** (2019-03), 348–359. ISSN: 1352-2310. DOI: 10.1016/j.atmosenv.2018.12.042. URL: https://www.sciencedirect.com/science/article/pii/S1352231019300056 (visited on 2023-12-03).

[5] Connelly, E. and Dasgupta, A. "Electric vehicles". 2023-07. URL: https://www.iea.org/energy-system/transport/electric-vehicles (visited on 2023-12-03).

[6] Clean Energy Institute, University of Washington. "Lithium-Ion Battery". 2015-11. URL: https://www.cei.washington.edu/research/energy-storage/lithium-ion-battery/ (visited on 2023-12-03).

[7] Pesaran, A., Vlahinos, A., and Stuart, T. "Cooling and Preheating of Batteries in Hybrid Electric Vehicles". *The 6th ASME-JSME Thermal Engineering Joint Conference*. American Society of Mechanical Engineers Digital Collection, 2003.

[8] Liu, J. et al. "Analysis of Maximum Return Air Ratio on No-fogging Condition by In-cabin Climate Simulation for EV". *Energy Procedia* **105** (2017-05), 2445–2450. ISSN: 18766102. DOI: 10.1016/j.egypro.2017.03.703. URL: https://linkinghub.elsevier.com/retrieve/pii/S187661021730766X (visited on 2023-01-04).

[9] Brady, J. and O'Mahony, M. "Development of a driving cycle to evaluate the energy economy of electric vehicles in urban areas". *Applied Energy* **177** (2016-09), 165–178. ISSN: 0306-2619. DOI: 10.1016/j.apenergy.2016.05.094. URL: https://www.sciencedirect.com/science/article/pii/S0306261916306924 (visited on 2023-12-08).

[10] Romano, L. "The operating cycle representation of road transport missions". ISBN: 9789179058883. PhD thesis. Sweden: Chalmers University of Technology, 2023. URL: https://research.chalmers.se/en/publication/536236 (visited on 2023-12-08).

[11] Greenwood, I. D., Dunn, R. C., and Raine, R. R. "Estimating the Effects of Traffic Congestion on Fuel Consumption and Vehicle Emissions Based on Acceleration Noise". *Journal of Transportation Engineering* **133**.2 (2007-02). Publisher: American Society of Civil Engineers, 96–104. ISSN: 0733-947X. DOI: 10.1061/(ASCE)0733-947X(2007)133:2(96). URL: https://ascelibrary.org/doi/10.1061/%28ASCE%290733-947X%282007%29133%3A2%2896%29 (visited on 2023-12-08).

[12] Burgess, S. C. and Choi, J. M. J. "A parametric study of the energy demands of car transportation: a case study of two competing commuter routes in the UK". *Transportation Research Part D: Transport and Environment* **8**.1 (2003-01), 21–36. ISSN: 1361-9209. DOI:

10.1016/S1361-9209(02)00016-0. URL: https://www.sciencedirect.com/science/article/pii/S1361920902000160 (visited on 2023-12-08).

[13] Liu, K., Yamamoto, T., and Morikawa, T. "Impact of road gradient on energy consumption of electric vehicles". *Transportation Research Part D: Transport and Environment* **54** (2017-07), 74–81. ISSN: 1361-9209. DOI: 10.1016/j.trd.2017.05.005. URL: https://www.sciencedirect.com/science/article/pii/S1361920917303887 (visited on 2023-12-08).

[14] Taggart, J. "Ambient temperature impacts on real-world electric vehicle efficiency & range". *2017 IEEE Transportation Electrification Conference and Expo (ITEC)*. 2017-06, pp. 186–190. DOI: 10.1109/ITEC.2017.7993269.

[15] Askerdal, M., Fredriksson, J., and Laine, L. "Development of simplified air drag models including crosswinds for commercial heavy vehicle combinations". *Vehicle System Dynamics* **0**.0 (2023). https://doi.org/10.1080/00423114.2023.2213786, 1–18. ISSN: 0042-3114. DOI: 10.1080/00423114.2023.2213786. URL: https://doi.org/10.1080/00423114.2023.2213786 (visited on 2023-12-08).

[16] Raeesi, A., McAuliffe, B., and Galler, J. "Impact of Precipitation Drag on a Road Vehicle". SAE Technical Paper 2023-01-0792. ISSN: 0148-7191, 2688-3627. Warrendale, PA: SAE International, 2023-04. DOI: 10.4271/2023-01-0792. URL: https://www.sae.org/publications/technical-papers/content/2023-01-0792/ (visited on 2023-12-08).

[17] Törnell, J. "Aerodynamics of vehicle platooning". ISBN: 9789179058012. PhD thesis. Sweden: Chalmers University of Technology, 2023. URL: https://research.chalmers.se/en/publication/534569 (visited on 2023-12-08).

[18] Romano, L. et al. "Stochastic modeling of mission stops and variable cargo weight for heavy-duty trucks". *2023 IEEE Vehicle Power and Propulsion Conference*. 2023. URL: https://research.chalmers.se/en/publication/536631 (visited on 2023-12-08).

[19] Steinstraeter, M., Heinrich, T., and Lienkamp, M. "Effect of Low Temperature on Electric Vehicle Range". *World Electric Vehicle Journal* **12**.3 (2021-09). Number: 3 Publisher: Multidisciplinary Digital Publishing Institute, 115. ISSN: 2032-6653. DOI: 10.3390/wevj12030115. URL: https://www.mdpi.com/2032-6653/12/3/115 (visited on 2023-12-07).

[20] Al-Wreikat, Y., Serrano, C., and Sodré, J. R. "Effects of ambient temperature and trip characteristics on the energy consumption of an electric vehicle". *Energy* **238** (2022-01), 122028. ISSN: 0360-5442. DOI: 10.1016/j.energy.2021.122028. URL: https://www.sciencedirect.com/science/article/pii/S0360544221022763 (visited on 2023-09-22).

[21] Al-Wreikat, Y., Serrano, C., and Sodré, J. R. "Driving behaviour and trip condition effects on the energy consumption of an electric vehicle under real-world driving". *Applied Energy* **297** (2021-09), 117096. ISSN: 0306-2619. DOI: 10.1016/j.apenergy.2021.117096. URL: https://www.sciencedirect.com/science/article/pii/S0306261921005444 (visited on 2023-12-08).

[22] Yuksel, T. and Michalek, J. J. "Effects of Regional Temperature on Electric Vehicle Efficiency, Range, and Emissions in the United States". *Environmental Science & Technology* **49**.6 (2015-03). Publisher: American Chemical Society, 3974–3980. ISSN: 0013-936X. DOI: 10.1021/es505621s. URL: https://doi.org/10.1021/es505621s (visited on 2023-12-07).

[23] Liu, K. et al. "Exploring the interactive effects of ambient temperature and vehicle auxiliary loads on electric vehicle energy consumption". *Applied Energy*. Transformative

Innovations for a Sustainable Future – Part III **227** (2018-10), 324–331. ISSN: 0306-2619. DOI: 10.1016/j.apenergy.2017.08.074. URL: https://www.sciencedirect.com/science/article/pii/S0306261917310929 (visited on 2023-12-04).

[24] Hyttinen, J. "Modelling and experimental testing of truck tyre rolling resistance". PhD thesis. Sweden: KTH Royal Institute of Technology, 2023. URL: https://urn.kb.se/resolve?urn=urn:nbn:se:kth:diva-335323 (visited on 2023-12-22).

[25] Chowdhury, S. et al. "Total Thermal Management of Battery Electric Vehicles (BEVs)". *SAE Technical Papers* **2018-37-0026** (2018-05). DOI: 10.4271/2018-37-0026. URL: https://www.sae.org/content/2018-37-0026/ (visited on 2023-01-04).

[26] Zhang, Z. et al. "Climate control loads prediction of electric vehicles". *Applied Thermal Engineering* **110** (2017-01), 1183–1188. ISSN: 1359-4311. DOI: 10.1016/j.applthermaleng.2016.08.186. URL: https://www.sciencedirect.com/science/article/pii/S1359431116315459 (visited on 2023-12-14).

[27] Zhang, Z. et al. "Electric vehicle range extension strategies based on improved AC system in cold climate – A review". *International Journal of Refrigeration* **88** (2018-04), 141–150. ISSN: 0140-7007. DOI: 10.1016/j.ijrefrig.2017.12.018. URL: https://www.sciencedirect.com/science/article/pii/S0140700718300033 (visited on 2023-09-27).

[28] Chiriac, G. et al. "Electric Bus Indoor Heat Balance in Cold Weather". *Applied Sciences* **11**.24 (2021-01). Number: 24 Publisher: Multidisciplinary Digital Publishing Institute, 11761. ISSN: 2076-3417. DOI: 10.3390/app112411761. URL: https://www.mdpi.com/2076-3417/11/24/11761 (visited on 2023-12-15).

[29] Delos Reyes, J. R. M., Parsons, R. V., and Hoemsen, R. "Winter Happens: The Effect of Ambient Temperature on the Travel Range of Electric Vehicles". *IEEE Transactions on Vehicular Technology* **65**.6 (2016-06). Conference Name: IEEE Transactions on Vehicular Technology, 4016–4022. ISSN: 1939-9359. DOI: 10.1109/TVT.2016.2544178. URL: https://ieeexplore.ieee.org/abstract/document/7436782 (visited on 2023-12-11).

[30] Meyer, N. et al. "The Impact of Driving Cycle and Climate on Electrical Consumption & Range of Fully Electric Passenger Vehicles". *EVS26 - International Battery, Hybrid and Fuel Cell Electric Vehicle Symposium*. Los Angeles, California, 2012.

[31] Ramsey, D. et al. "Simulation of an electric vehicle to study the impact of cabin heating on the driving range". *2020 IEEE 91st Vehicular Technology Conference (VTC2020-Spring)*. ISSN: 2577-2465. 2020-05, pp. 1–5. DOI: 10.1109/VTC2020-Spring48590.2020.9129169. URL: https://ieeexplore.ieee.org/document/9129169 (visited on 2023-12-12).

[32] Horrein, L. et al. "Impact of Heating System on the Range of an Electric Vehicle". *IEEE Transactions on Vehicular Technology* **66**.6 (2017-06). Conference Name: IEEE Transactions on Vehicular Technology, 4668–4677. ISSN: 1939-9359. DOI: 10.1109/TVT.2016.2615095. URL: https://ieeexplore.ieee.org/document/7582495 (visited on 2023-12-12).

[33] Liu, H. et al. "Thermal issues about Li-ion batteries and recent progress in battery thermal management systems: A review". *Energy Conversion and Management* **150** (2017-10), 304–330. ISSN: 01968904. DOI: 10.1016/j.enconman.2017.08.016. URL: https://linkinghub.elsevier.com/retrieve/pii/S0196890417307288 (visited on 2023-01-04).

[34] Nagasubramanian, G. "Electrical characteristics of 18650 Li-ion cells at low temperatures". *Journal of Applied Electrochemistry* **31**.1 (2001-01), 99–104. ISSN: 1572-8838. DOI: 10.

1023/A:1004113825283. URL: https://doi.org/10.1023/A:1004113825283 (visited on 2023-12-10).

[35] Ji, Y., Zhang, Y., and Wang, C.-Y. "Li-Ion Cell Operation at Low Temperatures". *Journal of The Electrochemical Society* **160**.4 (2013-02). Publisher: IOP Publishing, A636. ISSN: 1945-7111. DOI: 10.1149/2.047304jes. URL: https://iopscience.iop.org/article/10.1149/2.047304jes/meta (visited on 2023-12-10).

[36] Zhang, S. S., Xu, K., and Jow, T. R. "The low temperature performance of Li-ion batteries". *Journal of Power Sources* **115**.1 (2003-03), 137–140. ISSN: 0378-7753. DOI: 10.1016/S0378-7753(02)00618-3. URL: https://www.sciencedirect.com/science/article/pii/S0378775302006183 (visited on 2023-12-10).

[37] Zhang, S. S., Xu, K., and Jow, T. R. "Electrochemical impedance study on the low temperature of Li-ion batteries". *Electrochimica Acta* **49**.7 (2004-03), 1057–1061. ISSN: 0013-4686. DOI: 10.1016/j.electacta.2003.10.016. URL: https://www.sciencedirect.com/science/article/pii/S0013468603008478 (visited on 2023-12-10).

[38] Waldmann, T. et al. "Temperature dependent ageing mechanisms in Lithium-ion batteries – A Post-Mortem study". *Journal of Power Sources* **262** (2014-09), 129–135. ISSN: 0378-7753. DOI: 10.1016/j.jpowsour.2014.03.112. URL: https://www.sciencedirect.com/science/article/pii/S0378775314004352 (visited on 2023-12-10).

[39] Fan, J. and Tan, S. "Studies on Charging Lithium-Ion Cells at Low Temperatures". *Journal of The Electrochemical Society* **153**.6 (2006-04). Publisher: IOP Publishing, A1081. ISSN: 1945-7111. DOI: 10.1149/1.2190029. URL: https://iopscience.iop.org/article/10.1149/1.2190029/meta (visited on 2023-12-10).

[40] Ma, S. et al. "Temperature effect and thermal impact in lithium-ion batteries: A review". *Progress in Natural Science: Materials International* **28**.6 (2018-12), 653–666. ISSN: 10020071. DOI: 10.1016/j.pnsc.2018.11.002. URL: https://linkinghub.elsevier.com/retrieve/pii/S1002007118307536 (visited on 2023-01-04).

[41] Hu, X. et al. "Battery warm-up methodologies at subzero temperatures for automotive applications: Recent advances and perspectives". *Progress in Energy and Combustion Science* **77** (2020-03), 100806. ISSN: 0360-1285. DOI: 10.1016/j.pecs.2019.100806. URL: https://www.sciencedirect.com/science/article/pii/S0360128519301169 (visited on 2023-12-04).

[42] Rodrigues, M.-T. F. et al. "A materials perspective on Li-ion batteries at extreme temperatures". *Nature Energy* **2**.8 (2017-07). Number: 8 Publisher: Nature Publishing Group, 1–14. ISSN: 2058-7546. DOI: 10.1038/nenergy.2017.108. URL: https://www.nature.com/articles/nenergy2017108 (visited on 2023-12-10).

[43] Bandhauer, T. M., Garimella, S., and Fuller, T. F. "A Critical Review of Thermal Issues in Lithium-Ion Batteries". *Journal of The Electrochemical Society* **158**.3 (2011), R1. ISSN: 00134651. DOI: 10.1149/1.3515880. URL: https://iopscience.iop.org/article/10.1149/1.3515880 (visited on 2023-01-04).

[44] Lei, S., Xin, S., and Liu, S. "Separate and integrated thermal management solutions for electric vehicles: A review". *Journal of Power Sources* **550** (2022-12), 232133. ISSN: 0378-7753. DOI: 10.1016/j.jpowsour.2022.232133. URL: https://www.sciencedirect.com/science/article/pii/S0378775322011107 (visited on 2023-12-05).

[45] Zou, H. et al. "Performance Analysis of a Heat Pump Air Conditioning System Coupling with Battery Cooling for Electric Vehicles". *Energy Procedia*. International Conference on Applied Energy, ICAE2014 **61** (2014-01), 891–894. ISSN: 1876-6102. DOI: 10.1016/

j.egypro.2014.11.989. URL: https://www.sciencedirect.com/science/article/pii/S1876610214028197 (visited on 2023-12-19).

[46] Cen, J., Li, Z., and Jiang, F. "Experimental investigation on using the electric vehicle air conditioning system for lithium-ion battery thermal management". *Energy for Sustainable Development* **45** (2018-08), 88–95. ISSN: 0973-0826. DOI: 10.1016/j.esd.2018.05.005. URL: https://www.sciencedirect.com/science/article/pii/S0973082618301753 (visited on 2023-12-19).

[47] Shen, M. and Gao, Q. "System simulation on refrigerant-based battery thermal management technology for electric vehicles". *Energy Conversion and Management* **203** (2020-01), 112176. ISSN: 0196-8904. DOI: 10.1016/j.enconman.2019.112176. URL: https://www.sciencedirect.com/science/article/pii/S0196890419311823 (visited on 2024-04-08).

[48] Zhang, K. et al. "Exergy Analysis of Electric Vehicle Heat Pump Air Conditioning System with Battery Thermal Management System". *Journal of Thermal Science* **29**.2 (2020-04), 408–422. ISSN: 1993-033X. DOI: 10.1007/s11630-019-1128-2. URL: https://doi.org/10.1007/s11630-019-1128-2 (visited on 2023-12-19).

[49] Han, X. et al. "Numerical study on the heating performance of a novel integrated thermal management system for the electric bus". *Energy* **186** (2019-11), 115812. ISSN: 0360-5442. DOI: 10.1016/j.energy.2019.07.142. URL: https://www.sciencedirect.com/science/article/pii/S0360544219314847 (visited on 2023-12-19).

[50] Suh, I.-S. et al. "Design and experimental analysis of an efficient HVAC (heating, ventilation, air-conditioning) system on an electric bus with dynamic on-road wireless charging". *Energy* **81** (2015-03), 262–273. ISSN: 0360-5442. DOI: 10.1016/j.energy.2014.12.038. URL: https://www.sciencedirect.com/science/article/pii/S0360544214014054 (visited on 2023-12-19).

[51] Ahn, J. H. et al. "Heating performance characteristics of a dual source heat pump using air and waste heat in electric vehicles". *Applied Energy* **119** (2014-04), 1–9. ISSN: 0306-2619. DOI: 10.1016/j.apenergy.2013.12.065. URL: https://www.sciencedirect.com/science/article/pii/S0306261914000051 (visited on 2023-09-29).

[52] Nielsen, F., Uddheim, Å., and Dalenbäck, J.-O. "Potential energy consumption reduction of automotive climate control systems". *Applied Thermal Engineering* **106** (2016-08), 381–389. ISSN: 1359-4311. DOI: 10.1016/j.applthermaleng.2016.05.137. URL: https://www.sciencedirect.com/science/article/pii/S1359431116308158 (visited on 2023-12-14).

[53] Jeffers, M. A., Chaney, L., and Rugh, J. P. "Climate Control Load Reduction Strategies for Electric Drive Vehicles in Cold Weather". *SAE International Journal of Passenger Cars - Mechanical Systems* **9**.1 (2016-04), 75–82. ISSN: 1946-4002. DOI: 10.4271/2016-01-0262. URL: https://www.sae.org/content/2016-01-0262/ (visited on 2023-01-04).

[54] Gasworth, S. and Tankala, T. "Reduced Steady State Heating and Air Conditioning Loads via Reduced Glazing Thermal Conductivity". SAE Technical Paper 2011-01-0126. ISSN: 0148-7191, 2688-3627. Warrendale, PA: SAE International, 2011-04. DOI: 10.4271/2011-01-0126. URL: https://www.sae.org/publications/technical-papers/content/2011-01-0126/ (visited on 2023-12-14).

[55] Türler, D., Hopkins, D., and Goudey, H. "Reducing Vehicle Auxiliary Loads Using Advanced Thermal Insulation and Window Technologies". SAE Technical Paper 2003-01-1076. ISSN: 0148-7191, 2688-3627. Warrendale, PA: SAE International, 2003-03. DOI:

10.4271/2003-01-1076. URL: https://www.sae.org/publications/technical-papers/content/2003-01-1076/ (visited on 2023-12-14).

[56] Oiwake, M. et al. "Effects of the Glass and Body Heat Transfer Characteristics of a Hybrid Electric Vehicle on Its Fuel Consumption and Cruising Distance". 2017-03, pp. 2017–01–0184. DOI: 10.4271/2017-01-0184. URL: https://www.sae.org/content/2017-01-0184/ (visited on 2023-01-04).

[57] Wirth, S. et al. "Improved Thermal Insulation for Contemporary Automotive Roof Structures Based on a Computational Fluid Dynamics Heat Flux Approach". *Heat Transfer Engineering* **37**.16 (2016-11), 1418–1426. ISSN: 0145-7632. DOI: 10.1080/01457632.2015.1136170. URL: https://doi.org/10.1080/01457632.2015.1136170 (visited on 2023-12-14).

[58] Shikata, K. et al. "Development of Two Layer Flow HVAC Unit". SAE Technical Paper 1999-01-1199. ISSN: 0148-7191, 2688-3627. Warrendale, PA: SAE International, 1999-03. DOI: 10.4271/1999-01-1199. URL: https://www.sae.org/publications/technical-papers/content/1999-01-1199/ (visited on 2023-11-03).

[59] Hirai, S. et al. "The Humidity Control System Applied to Reduce Ventilation Heat Loss of HVAC Systems". *SAE 2011 World Congress & Exhibition*. 2011-04. DOI: 10.4271/2011-01-0134. URL: https://www.sae.org/content/2011-01-0134/ (visited on 2023-07-05).

[60] Zhang, G. et al. "Investigation on an improved heat pump AC system with the view of return air utilization and anti-fogging for electric vehicles". *Applied Thermal Engineering* **115** (2017-03), 726–735. ISSN: 1359-4311. DOI: 10.1016/j.applthermaleng.2016.12.143. URL: https://www.sciencedirect.com/science/article/pii/S1359431116345070 (visited on 2023-05-15).

[61] Higuchi, Y. et al. "Efficient Heat Pump System for PHEV/BEV". *WCX™ 17: SAE World Congress Experience*. 2017-03. DOI: 10.4271/2017-01-0188. URL: https://www.sae.org/content/2017-01-0188/ (visited on 2023-01-04).

[62] Yang, T. et al. "Experimental performance of a vapor-injection CO2 heat pump system for electric vehicles in 30 °C to 50 °C range". *Applied Thermal Engineering* **217** (2022-11), 119149. ISSN: 1359-4311. DOI: 10.1016/j.applthermaleng.2022.119149. URL: https://www.sciencedirect.com/science/article/pii/S1359431122010808 (visited on 2023-12-04).

[63] Zhang, Z. et al. "LCCP Analysis of Energy-Saving Effect of Defaulting to Recirculated Cabin Air in EV Mobile Air Conditioning System". *International Refrigeration and Air Conditioning Conference* (2016-01). URL: https://docs.lib.purdue.edu/iracc/1738.

[64] Wei, D. et al. "Vehicle cabin air quality: influence of air recirculation on energy use, particles, and CO2". *Environmental Science and Pollution Research* **30**.15 (2023-03), 43387–43402. ISSN: 1614-7499. DOI: 10.1007/s11356-023-25219-x. URL: https://doi.org/10.1007/s11356-023-25219-x (visited on 2023-12-14).

[65] Urbank, T. M. et al. "Development and Application of an Integrated Dew Point and Glass Temperature Sensor". *SAE Transactions* **110** (2001). Publisher: SAE International, 546–556. ISSN: 0096-736X. URL: https://www.jstor.org/stable/44730910 (visited on 2023-11-03).

[66] Lorenz, M. et al. "A Coupled Numerical Model to Predict Heat Transfer and Passenger Thermal Comfort in Vehicle Cabins". *SAE 2014 World Congress & Exhibition*. 2014-04, pp. 2014–01–0664. DOI: 10.4271/2014-01-0664. URL: https://www.sae.org/content/2014-01-0664/ (visited on 2023-07-05).

[67] Lorenz, M. "Reduction of Heating Loads and Interior Window Fogging in Vehicles". PhD thesis. Germany: Technische Universität München, 2015.

[68] Pan, L. et al. "Energy-saving effect of utilizing recirculated air in electric vehicle air conditioning system". *International Journal of Refrigeration* **102** (2019-06), 122–129. ISSN: 0140-7007. DOI: 10.1016/j.ijrefrig.2019.03.018. URL: https://www.sciencedirect.com/science/article/pii/S0140700719301173 (visited on 2023-07-05).

[69] Norin, F. "Insulating Glazing in Side Windows". *SAE Transactions* **98** (1989). Publisher: SAE International, 27–29. ISSN: 0096-736X. URL: https://www.jstor.org/stable/44472252 (visited on 2024-04-15).

[70] Durán, I. R. and Laroche, G. "Current trends, challenges, and perspectives of anti-fogging technology: Surface and material design, fabrication strategies, and beyond". *Progress in Materials Science* **99** (2019-01), 106–186. ISSN: 0079-6425. DOI: 10.1016/j.pmatsci.2018.09.001. URL: https://www.sciencedirect.com/science/article/pii/S0079642518300902 (visited on 2024-04-15).

[71] Jeffers, M. A., Chaney, L., and Rugh, J. P. "Climate Control Load Reduction Strategies for Electric Drive Vehicles in Warm Weather". SAE Technical Paper 2015-01-0355. ISSN: 0148-7191, 2688-3627. Warrendale, PA: SAE International, 2015-04. DOI: 10.4271/2015-01-0355. URL: https://www.sae.org/publications/technical-papers/content/2015-01-0355/ (visited on 2023-12-15).

[72] Rui, X. H. et al. "A comparative study on the low-temperature performance of LiFePO4/C and Li3V2(PO4)3/C cathodes for lithium-ion batteries". *Journal of Power Sources* **196**.4 (2011-02), 2109–2114. ISSN: 0378-7753. DOI: 10.1016/j.jpowsour.2010.10.063. URL: https://www.sciencedirect.com/science/article/pii/S037877531001863X (visited on 2023-12-18).

[73] Yang, B. et al. "Lithium difluorophosphate as an additive to improve the low temperature performance of LiNi0.5Co0.2Mn0.3O2/graphite cells". *Electrochimica Acta* **221** (2016-12), 107–114. ISSN: 0013-4686. DOI: 10.1016/j.electacta.2016.10.037. URL: https://www.sciencedirect.com/science/article/pii/S0013468616321247 (visited on 2023-12-18).

[74] Li, Q. et al. "Wide-Temperature Electrolytes for Lithium-Ion Batteries". *ACS Applied Materials & Interfaces* **9**.22 (2017-06). Publisher: American Chemical Society, 18826–18835. ISSN: 1944-8244. DOI: 10.1021/acsami.7b04099. URL: https://doi.org/10.1021/acsami.7b04099 (visited on 2023-12-18).

[75] Shang, Z. et al. "Structural optimization of lithium-ion battery for improving thermal performance based on a liquid cooling system". *International Journal of Heat and Mass Transfer* **130** (2019-03), 33–41. ISSN: 00179310. DOI: 10.1016/j.ijheatmasstransfer.2018.10.074. URL: https://linkinghub.elsevier.com/retrieve/pii/S0017931018324797 (visited on 2023-01-04).

[76] Afraz, M. V., Ali Mohammadi, Z., and Karimi, G. "A novel compact thermal management model for performance evaluation of tesla-like lithium-ion battery packs". *Energy Conversion and Management* **300** (2024-01), 117927. ISSN: 0196-8904. DOI: 10.1016/j.enconman.2023.117927. URL: https://www.sciencedirect.com/science/article/pii/S0196890423012736 (visited on 2023-12-05).

[77] Jarrett, A. and Kim, I. Y. "Design optimization of electric vehicle battery cooling plates for thermal performance". *Journal of Power Sources* **196**.23 (2011-12), 10359–10368. ISSN: 03787753. DOI: 10.1016/j.jpowsour.2011.06.090. URL: https://linkinghub.elsevier.com/retrieve/pii/S0378775311013279 (visited on 2023-01-04).

[78] Jarrett, A. and Kim, I. Y. "Influence of operating conditions on the optimum design of electric vehicle battery cooling plates". *Journal of Power Sources* **245** (2014-01), 644–655. ISSN: 03787753. DOI: 10.1016/j.jpowsour.2013.06.114. URL: https://linkinghub.elsevier.com/retrieve/pii/S037877531301121X (visited on 2023-01-04).

[79] Liu, H., Chika, E., and Zhao, J. "Investigation into the effectiveness of nanofluids on the mini-channel thermal management for high power lithium ion battery". *Applied Thermal Engineering* **142** (2018-09), 511–523. ISSN: 1359-4311. DOI: 10.1016/j.applthermaleng.2018.07.037. URL: https://www.sciencedirect.com/science/article/pii/S1359431118329119 (visited on 2023-12-18).

[80] Zhang, C., Jin, X., and Li, J. "PTC Self-Heating Experiments and Thermal Modeling of Lithium-Ion Battery Pack in Electric Vehicles". *Energies* **10**.4 (2017-04). Number: 4 Publisher: Multidisciplinary Digital Publishing Institute, 572. ISSN: 1996-1073. DOI: 10.3390/en10040572. URL: https://www.mdpi.com/1996-1073/10/4/572 (visited on 2023-12-18).

[81] Jin, X. et al. "Researches on Modeling and Experiment of Li-ion Battery PTC Self-heating in Electric Vehicles". *Energy Procedia*. Clean Energy for Clean City: CUE 2016–Applied Energy Symposium and Forum: Low-Carbon Cities and Urban Energy Systems **104** (2016-12), 62–67. ISSN: 1876-6102. DOI: 10.1016/j.egypro.2016.12.012. URL: https://www.sciencedirect.com/science/article/pii/S1876610216315673 (visited on 2023-12-18).

[82] Hallaj, S. A. and Selman, J. R. "A Novel Thermal Management System for Electric Vehicle Batteries Using Phase-Change Material". *Journal of The Electrochemical Society* **147**.9 (2000-09). Publisher: IOP Publishing, 3231. ISSN: 1945-7111. DOI: 10.1149/1.1393888. URL: https://iopscience.iop.org/article/10.1149/1.1393888/meta (visited on 2023-12-18).

[83] Ghadbeigi, L. et al. "Cold temperature performance of phase change material based battery thermal management systems". *Energy Reports* **4** (2018-11), 303–307. ISSN: 2352-4847. DOI: 10.1016/j.egyr.2018.04.001. URL: https://www.sciencedirect.com/science/article/pii/S2352484718300428 (visited on 2023-12-18).

[84] Wu, X., Chen, Z., and Wang, Z. "Analysis of Low Temperature Preheating Effect Based on Battery Temperature-Rise Model". *Energies* **10**.8 (2017-08). Number: 8 Publisher: Multidisciplinary Digital Publishing Institute, 1121. ISSN: 1996-1073. DOI: 10.3390/en10081121. URL: https://www.mdpi.com/1996-1073/10/8/1121 (visited on 2023-12-18).

[85] Du, J., Chen, Z., and Li, F. "Multi-Objective Optimization Discharge Method for Heating Lithium-Ion Battery at Low Temperatures". *IEEE Access* **6** (2018). Conference Name: IEEE Access, 44036–44049. ISSN: 2169-3536. DOI: 10.1109/ACCESS.2018.2837652. URL: https://ieeexplore.ieee.org/document/8360426 (visited on 2023-12-18).

[86] Mohan, S., Kim, Y., and Stefanopoulou, A. G. "Energy-Conscious Warm-Up of Li-Ion Cells From Subzero Temperatures". *IEEE Transactions on Industrial Electronics* **63**.5 (2016-05). Conference Name: IEEE Transactions on Industrial Electronics, 2954–2964. ISSN: 1557-9948. DOI: 10.1109/TIE.2016.2523440. URL: https://ieeexplore.ieee.org/document/7395333 (visited on 2023-12-18).

[87] Baba, H., Kawasaki, K., and Kawachi, H. "Battery Heating System for Electric Vehicles". SAE Technical Paper 2015-01-0248. ISSN: 0148-7191, 2688-3627. Warrendale, PA: SAE International, 2015-04. DOI: 10.4271/2015-01-0248. URL: https://www.sae.org/publications/technical-papers/content/2015-01-0248/ (visited on 2023-12-18).

[88] Lei, Z., Zhang, Y., and Lei, X. "Improving temperature uniformity of a lithium-ion battery by intermittent heating method in cold climate". *International Journal of Heat and Mass Transfer* **121** (2018-06), 275–281. ISSN: 0017-9310. DOI: 10.1016/j.ijheatmasstransfer.2017.12.159. URL: https://www.sciencedirect.com/science/article/pii/S0017931017341996 (visited on 2023-12-18).

[89] Qu, Z. G., Jiang, Z. Y., and Wang, Q. "Experimental study on pulse self–heating of lithium–ion battery at low temperature". *International Journal of Heat and Mass Transfer* **135** (2019-06), 696–705. ISSN: 0017-9310. DOI: 10.1016/j.ijheatmasstransfer.2019.02.020. URL: https://www.sciencedirect.com/science/article/pii/S0017931018352803 (visited on 2023-12-18).

[90] Hande, A. and Stuart, T. "AC heating for EV/HEV Batteries". *Power Electronics in Transportation, 2002.* 2002-10, pp. 119–124. DOI: 10.1109/PET.2002.1185559. URL: https://ieeexplore.ieee.org/document/1185559 (visited on 2023-12-18).

[91] Stuart, T. A. and Hande, A. "HEV battery heating using AC currents". *Journal of Power Sources* **129**.2 (2004-04), 368–378. ISSN: 0378-7753. DOI: 10.1016/j.jpowsour.2003.10.014. URL: https://www.sciencedirect.com/science/article/pii/S0378775303011352 (visited on 2023-12-18).

[92] Zhu, J. et al. "An alternating current heating method for lithium-ion batteries from subzero temperatures". *International Journal of Energy Research* **40**.13 (2016). _eprint: https://onlinelibrary.wiley.com/doi/pdf/10.1002/er.3576, 1869–1883. ISSN: 1099-114X. DOI: 10.1002/er.3576. URL: https://onlinelibrary.wiley.com/doi/abs/10.1002/er.3576 (visited on 2023-12-18).

[93] Ling, Z. et al. "Warming-Up Effects of Phase Change Materials on Lithium-Ion Batteries Operated at Low Temperatures". *Energy Technology* **4**.9 (2016), 1071–1076. ISSN: 2194-4296. DOI: 10.1002/ente.201600083. URL: https://onlinelibrary.wiley.com/doi/abs/10.1002/ente.201600083 (visited on 2023-12-17).

[94] Ouyang, D. et al. "Influence of low temperature conditions on lithium-ion batteries and the application of an insulation material". *RSC Advances* **9**.16 (2019), 9053–9066. ISSN: 2046-2069. DOI: 10.1039/C9RA00490D. URL: http://xlink.rsc.org/?DOI=C9RA00490D (visited on 2023-01-04).

[95] Wu, H. et al. "Experimental study on aerogel passive thermal control method for cylindrical lithium-ion batteries at low temperature". *Applied Thermal Engineering* **169** (2020-03), 114946. ISSN: 1359-4311. DOI: 10.1016/j.applthermaleng.2020.114946. URL: https://www.sciencedirect.com/science/article/pii/S135943111933234X (visited on 2023-12-17).

[96] Danca, P. et al. "On the Possibility of CFD Modeling of the Indoor Environment in a Vehicle". *Energy Procedia* **112** (2017-03), 656–663. ISSN: 18766102. DOI: 10.1016/j.egypro.2017.03.1133. URL: https://linkinghub.elsevier.com/retrieve/pii/S1876610217312584 (visited on 2023-01-04).

[97] Liu, W. et al. "Evaluation of various categories of turbulence models for predicting air distribution in an airliner cabin". *Building and Environment* **65** (2013-07), 118–131. ISSN: 0360-1323. DOI: 10.1016/j.buildenv.2013.03.018. URL: https://www.sciencedirect.com/science/article/pii/S036013231300098X (visited on 2023-06-16).

[98] Fojtlín, M. et al. "Airflow Measurement of the Car HVAC Unit Using Hot-wire Anemometry". *EPJ Web of Conferences* **114** (2016). Ed. by P. Dančová and M. Veselý, 02023. ISSN:

2100-014X. DOI: 10.1051/epjconf/201611402023. URL: http://www.epj-conferences.org/10.1051/epjconf/201611402023 (visited on 2023-01-04).

[99] Siemens. "Simcenter STAR-CCM+ User Guide". 2022. URL: https://docs.sw.siemens.com/en-US/doc/226870983/PL20230724207774020.starccmp_userguide_html?audience=external (visited on 2023-12-20).

[100] Josefsson, E., Hobeika, T., and Sebben, S. "Evaluation of wind tunnel interference on numerical prediction of wheel aerodynamics". *Journal of Wind Engineering and Industrial Aerodynamics* **224** (2022-05), 104945. ISSN: 0167-6105. DOI: 10.1016/j.jweia.2022.104945. URL: https://www.sciencedirect.com/science/article/pii/S0167610522000502 (visited on 2023-12-20).

[101] Hobeika, T. "Wheel Modelling and Cooling Flow Effects on Car Aerodynamics". ISBN: 9781085760720. Ph.D. Sweden: Chalmers Tekniska Hogskola (Sweden), 2018. URL: https://www.proquest.com/docview/2376175546/abstract/9153159E3BC6414FPQ/1 (visited on 2023-12-20).

[102] Mao, Y., Wang, J., and Li, J. "Experimental and numerical study of air flow and temperature variations in an electric vehicle cabin during cooling and heating". *Applied Thermal Engineering* **137** (2018-06), 356–367. ISSN: 13594311. DOI: 10.1016/j.applthermaleng.2018.03.099. URL: https://linkinghub.elsevier.com/retrieve/pii/S1359431117331058 (visited on 2023-01-04).

[103] Incropera, F. P. "Fundamentals of heat and mass transfer". 6th ed. Vol. 6. New York: Wiley, 2013. ISBN: 978-0-471-45728-2.

[104] Hickey, C. J., Raspet, R., and Slaton, W. V. "Effects of thermal diffusion on sound attenuation in evaporating and condensing gas-vapor mixtures in tubes". *The Journal of the Acoustical Society of America* **107**.3 (2000-03), 1126–1130. ISSN: 0001-4966. DOI: 10.1121/1.428403. URL: https://doi.org/10.1121/1.428403 (visited on 2023-12-25).

[105] Gualtieri, C. et al. "On the Values for the Turbulent Schmidt Number in Environmental Flows". *Fluids* **2**.2 (2017-06). Number: 2 Publisher: Multidisciplinary Digital Publishing Institute, 17. ISSN: 2311-5521. DOI: 10.3390/fluids2020017. URL: https://www.mdpi.com/2311-5521/2/2/17 (visited on 2023-12-25).

[106] Ghiaasiaan, S. M. "Convective Heat and Mass Transfer". CRC Press, 2018-06. ISBN: 978-1-351-11273-4.

[107] Zhang, H. et al. "Studies of air-flow and temperature fields inside a passenger compartment for improving thermal comfort and saving energy. Part I: Test/numerical model and validation". *Applied Thermal Engineering* **29**.10 (2009-07), 2022–2027. ISSN: 13594311. DOI: 10.1016/j.applthermaleng.2008.10.005. URL: https://linkinghub.elsevier.com/retrieve/pii/S1359431108004183 (visited on 2023-01-04).

[108] Hayakawa, Y., Sato, D., and Yamada, N. "Measurement of the Convective Heat Transfer Coefficient and Temperature of Vehicle-Integrated Photovoltaic Modules". *Energies* **15**.13 (2022-01). Number: 13 Publisher: Multidisciplinary Digital Publishing Institute, 4818. ISSN: 1996-1073. DOI: 10.3390/en15134818. URL: https://www.mdpi.com/1996-1073/15/13/4818 (visited on 2023-06-13).

[109] Takahashi, Y. et al. "Thermoregulation model JOS-3 with new open source code". *Energy and Buildings* **231** (2021-01), 110575. ISSN: 0378-7788. DOI: 10.1016/j.enbuild.2020.110575. URL: https://www.sciencedirect.com/science/article/pii/S0378778820333612 (visited on 2023-01-04).

[110] Chang, T.-B. et al. "Development of a CFD model for simulating vehicle cabin indoor air quality". *Transportation Research Part D: Transport and Environment* **62** (2018-07),

433–440. ISSN: 13619209. DOI: 10.1016/j.trd.2018.03.018. URL: https://linkinghub.elsevier.com/retrieve/pii/S1361920917309744 (visited on 2023-01-04).

[111] Mansour, E. et al. "Measurement of temperature and relative humidity in exhaled breath". *Sensors and Actuators B: Chemical* **304** (2020-02), 127371. ISSN: 0925-4005. DOI: 10.1016/j.snb.2019.127371. URL: https://www.sciencedirect.com/science/article/pii/S0925400519315709 (visited on 2023-03-20).

[112] Rintamäki, H. and Rissanen, S. "Heat Strain in Cold". *Industrial Health* **44**.3 (2006), 427–432. DOI: 10.2486/indhealth.44.427.

[113] Zhang, H. "Human Thermal Sensation and Comfort in Transient and Non-Uniform Thermal Environments". PhD thesis. United States of America: University of California, Berkeley, 2003.

[114] Wang, F. "Clothing Evaporative Resistance: Its Measurements and Application in Prediction of Heat Strain". ISBN 978-91-7473-158-3. PhD thesis. Sweden: Lund University, 2011-11.

[115] Gamma Technologies. "GT-SUITE User's Manual". **2** (2022).

[116] Kays, W. M., Crawford, M. E., and Weigand, B. "Convective heat and mass transfer". 4. ed. McGraw-Hill series in mechanical engineering. McGraw-Hill Higher Education, 2005. ISBN: 978-0-07-246876-2.

[117] Huria, T. et al. "High fidelity electrical model with thermal dependence for characterization and simulation of high power lithium battery cells". *2012 IEEE International Electric Vehicle Conference*. 2012-03, pp. 1–8. DOI: 10.1109/IEVC.2012.6183271. URL: https://ieeexplore.ieee.org/document/6183271 (visited on 2023-12-29).

[118] Bernardi, D., Pawlikowski, E., and Newman, J. "A General Energy Balance for Battery Systems". *Journal of The Electrochemical Society* **132**.1 (1985-01). Publisher: IOP Publishing, 5. ISSN: 1945-7111. DOI: 10.1149/1.2113792. URL: https://iopscience.iop.org/article/10.1149/1.2113792/meta (visited on 2023-12-29).

[119] Hyttinen, J. et al. "Truck tyre transient rolling resistance and temperature at varying vehicle velocities - Measurements and simulations". *Polymer Testing* **122** (2023-05), 108004. ISSN: 0142-9418. DOI: 10.1016/j.polymertesting.2023.108004. URL: https://www.sciencedirect.com/science/article/pii/S0142941823000843 (visited on 2024-01-07).

[120] Romano, L. et al. "Development of the Västra Götaland Operating Cycle for Long-Haul Heavy-Duty Vehicles". *IEEE Access* **11** (2023), 73268–73302. ISSN: 2169-3536. DOI: 10.1109/ACCESS.2023.3295989. URL: https://ieeexplore.ieee.org/document/10184427/ (visited on 2024-01-29).

[121] "Road rules and safety in Sweden". URL: https://europa.eu/youreurope/citizens/travel/driving-abroad/road-rules-and-safety/sweden/index_en.htm (visited on 2024-01-17).

[122] Kolich, M. et al. "Thermophysical Properties Measurement of Interior Car Materials vs. Temperature and Mechanical Compression". *SAE Int. J. Mater. Manf.* **7(3):646-654** (2014). URL: https://www.sae.org/publications/technical-papers/content/2014-01-1024/ (visited on 2024-01-29).

[123] Pokorny, J., Fiser, J., and Jicha, M. "A parametric study of influence of material properties on car cabin environment". *EPJ Web of Conferences* **67** (2014). Publisher: EDP Sciences, 02096. ISSN: 2100-014X. DOI: 10.1051/epjconf/20146702096. URL: https://www.epj-conferences.org/articles/epjconf/abs/2014/04/epjconf_efm-13_02096/epjconf_efm-13_02096.html (visited on 2024-01-29).

[124] Ramesh Babu, A. et al. "System-Level Modeling and Thermal Simulations of Large Battery Packs for Electric Trucks". *Energies* **14**.16 (2021-01). Number: 16 Publisher: Multidisciplinary Digital Publishing Institute, 4796. ISSN: 1996-1073. DOI: 10.3390/en14164796. URL: https://www.mdpi.com/1996-1073/14/16/4796 (visited on 2023-01-04).

[125] Ramesh Babu, A., Minovski, B., and Sebben, S. "Thermal encapsulation of large battery packs for electric vehicles operating in cold climate". *Applied Thermal Engineering* **212** (2022-07), 118548. ISSN: 1359-4311. DOI: 10.1016/j.applthermaleng.2022.118548. URL: https://www.sciencedirect.com/science/article/pii/S1359431122004999 (visited on 2023-01-04).

[126] Ramesh Babu, A., Sebben, S., and Bark, T. "Effect of Cabin Insulation on the Heating Performance in EVs at Low Temperatures". *SAE WCX Conference*. Detroit, Michigan, United States: SAE Technical Papers, 2023-04. DOI: 10.4271/2023-01-0763. URL: https://www.sae.org/content/2023-01-0763 (visited on 2023-06-13).

[127] Ramesh Babu, A. et al. "An adaptive cabin air recirculation strategy for an electric truck using a coupled CFD-thermoregulation approach". *International Journal of Heat and Mass Transfer* **221** (2024-04), 125056. ISSN: 0017-9310. DOI: 10.1016/j.ijheatmasstransfer.2023.125056. URL: https://www.sciencedirect.com/science/article/pii/S0017931023012012 (visited on 2023-12-14).

[128] Ramesh Babu, A. et al. "Heating load reduction strategies for cabin and battery pack climatization in electric trucks operating in cold climates." *Submitted to Thermal Science and Engineering Progress* (2024).